

AD-A166 742

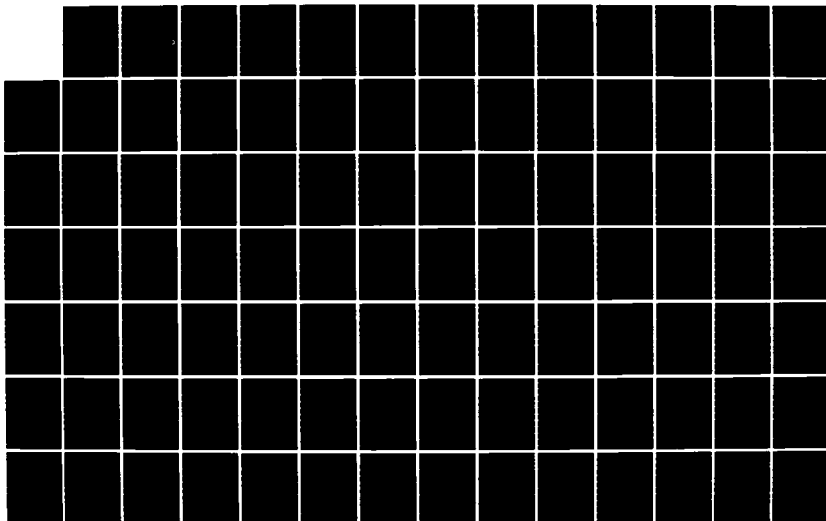
ATOMISTIC SIMULATION STUDY OF VACANCY CLUSTERS IN  
COPPER(U) AIR FORCE INST OF TECH WRIGHT-PATTERSON AFB  
OM M J SABOCHICK 1985 AFIT/CI/NR-86-350

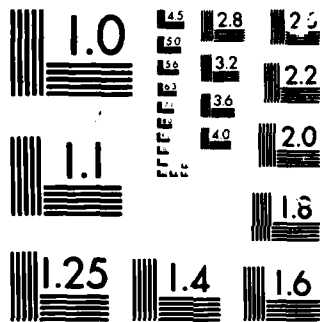
1/3

UNCLASSIFIED

F/G 11/6

NL





MICROCOPY

CHART

AD-A166 742

SECURITY CLASSIFICATION OF THIS PAGE (When Data Entered)

| REPORT DOCUMENTATION PAGE   |                       | READ INSTRUCTIONS<br>BEFORE COMPLETING FORM                    |
|---|-----------------------|--|
| 1. REPORT NUMBER<br>AFIT/CI/NR 86-35D   | 2. GOVT ACCESSION NO. | 3. RECIPIENT'S CATALOG NUMBER                                  |
| 4. TITLE (and Subtitle)<br>Atomistic Simulation Study Of Vacancy Clusters<br>In Copper  |                       | 5. TYPE OF REPORT & PERIOD COVERED<br>THESIS/DISSERTATION      |
|   |                       | 6. PERFORMING ORG. REPORT NUMBER                               |
| 7. AUTHOR(s)<br>Michael John Sabochick  |                       | 8. CONTRACT OR GRANT NUMBER(s)                                 |
| 9. PERFORMING ORGANIZATION NAME AND ADDRESS<br>AFIT STUDENT AT:<br>Massachusetts Institute of Technology  |                       | 10. PROGRAM ELEMENT, PROJECT, TASK<br>AREA & WORK UNIT NUMBERS |
| 11. CONTROLLING OFFICE NAME AND ADDRESS<br>AFIT/NR<br>WPAFB OH 45433-6583   |                       | 12. REPORT DATE<br>1985  |
| 14. MONITORING AGENCY NAME & ADDRESS (if different from Controlling Office)   |                       | 13. NUMBER OF PAGES<br>224                                     |
|   |                       | 15. SECURITY CLASS. (of this report)<br>UNCLASS                |
|   |                       | 15a. DECLASSIFICATION/DOWNGRADING<br>SCHEDULE                  |
| 16. DISTRIBUTION STATEMENT (of this Report)<br><br>APPROVED FOR PUBLIC RELEASE; DISTRIBUTION UNLIMITED  |                       |  |
| 17. DISTRIBUTION STATEMENT (of the abstract entered in Block 20, if different from Report)  |                       |  |
| 18. SUPPLEMENTARY NOTES<br>APPROVED FOR PUBLIC RELEASE: IAW AFR 190-1<br><br>LYNN E. WOLAVER<br>Dean for Research and<br>Professional Development<br>AFIT/NR, WPAFB OH 45433-6583 |                       |  |
| 19. KEY WORDS (Continue on reverse side if necessary and identify by block number)  |                       |  |
| 20. ABSTRACT (Continue on reverse side if necessary and identify by block number)   |                       |  |

DD FORM 1 JAN 73 1473

EDITION OF 1 NOV 65 IS OBSOLETE

SECURITY CLASSIFICATION OF THIS PAGE (When Data Entered)

Michael John Sabochick, Capt., USAF  
1986, 224 pages  
Doctor of Philosophy in Nuclear Engineering  
Massachusetts Institute of Technology

Abstract

Defect properties of copper are calculated using molecular statics with an interatomic potential recently derived from first principles. Tri- and tetravacancies are found to be very mobile with migration energies of 0.56 and 0.39 eV, respectively, compared to previously calculated single and divacancy migration energies of 0.82 and 0.55 eV, respectively. Using the binding and migration energies calculated with the interatomic potential, annealing kinetics in copper and modeled using rate equations. The effective activation energy of annealing in the model is within 0.02 eV of single vacancy migration energy over a wide range of sink and initial single vacancy concentrations, which conforms to experimental results. In two cases, however, the larger clusters affect the activation energy and no definitive conclusions about whether or not the calculated cluster migration energies are correct for copper can be made.

The stability and structure of larger vacancy clusters with ten to forty vacancies were also investigated using the first principles copper potential. The stacking fault energy was first calculated and, for the potential cutoff radius used in the defect calculations, yielded a value of 65 mJ/m<sup>2</sup> compared to the experimental value of ~70 mJ/m<sup>2</sup>. To investigate the large clusters, vacancy platelets of various sizes were created in a close-packed plane and the system was relaxed to the minimum energy configuration. Small vacancy platelets with as few as ten vacancies collapsed into stacking fault tetrahedra and faulted loops, depending on the shape of the platelet. Stacking fault tetrahedra are found to be the most stable large clusters.

- i -

|                     |                                     |
|---------------------|-------------------------------------|
| Accession For       |                                     |
| NTIS GRA&I          | <input checked="" type="checkbox"/> |
| DTIC TAB            | <input type="checkbox"/>            |
| Unannounced         | <input type="checkbox"/>            |
| Justification       |                                     |
| By                  |                                     |
| Distribution /      |                                     |
| Avail. and/or Sales |                                     |
| Distribution /      |                                     |
| Avail. and/or Sales |                                     |

A-1





## AFIT RESEARCH ASSESSMENT

The purpose of this questionnaire is to ascertain the value and/or contribution of research accomplished by students or faculty of the Air Force Institute of Technology (AU). It would be greatly appreciated if you would complete the following questionnaire and return it to:

AFIT/NR  
Wright-Patterson AFB OH 45433

RESEARCH TITLE: \_\_\_\_\_

AUTHOR: \_\_\_\_\_

### RESEARCH ASSESSMENT QUESTIONS:

1. Did this research contribute to a current Air Force project?

☐ a. YES

☐ b. NO

2. Do you believe this research topic is significant enough that it would have been researched (or contracted) by your organization or another agency if AFIT had not?

☐ a. YES

☐ b. NO

3. The benefits of AFIT research can often be expressed by the equivalent value that your agency achieved/received by virtue of AFIT performing the research. Can you estimate what this research would have cost if it had been accomplished under contract or if it had been done in-house in terms of manpower and/or dollars?

☐ a. MAN-YEARS \_\_\_\_\_

☐ b. \$ \_\_\_\_\_

4. Often it is not possible to attach equivalent dollar values to research, although the results of the research may, in fact, be important. Whether or not you were able to establish an equivalent value for this research (3. above), what is your estimate of its significance?

☐ a. HIGHLY  
SIGNIFICANT

☐ b. SIGNIFICANT

☐ c. SLIGHTLY  
SIGNIFICANT

☐ d. OF NO  
SIGNIFICANCE

5. AFIT welcomes any further comments you may have on the above questions, or any additional details concerning the current application, future potential, or other value of this research. Please use the bottom part of this questionnaire for your statement(s).

NAME \_\_\_\_\_ GRADE \_\_\_\_\_ POSITION \_\_\_\_\_

ORGANIZATION \_\_\_\_\_ LOCATION \_\_\_\_\_

STATEMENT(s):

FOLD DOWN ON OUTSIDE - SEAL WITH TAPE

AFIT/NR  
WRIGHT-PATTERSON AFB OH 45433  
OFFICIAL BUSINESS  
PENALTY FOR PRIVATE USE. \$300



NO POSTAGE  
NECESSARY  
IF MAILED  
IN THE  
UNITED STATES

**BUSINESS REPLY MAIL**

FIRST CLASS PERMIT NO. 73236 WASHINGTON D.C.

POSTAGE WILL BE PAID BY ADDRESSEE

AFIT/ DAA  
Wright-Patterson AFB OH 45433



FOLD IN

ATOMISTIC SIMULATION STUDY OF  
VACANCY CLUSTERS IN COPPER

by

Michael John Sabochick

B.S. University of Florida  
(1981)

M.S. Air Force Institute of  
Technology  
(1982)

SUBMITTED TO THE DEPARTMENT OF NUCLEAR  
ENGINEERING IN PARTIAL FULFILLMENT OF  
THE REQUIREMENTS FOR THE DEGREE OF

DOCTOR OF PHILOSOPHY

at the

MASSACHUSETTS INSTITUTE OF TECHNOLOGY

December 1985

Copyright © 1985 Massachusetts Institute of Technology

Signature of Author

\_\_\_\_\_  
Department of Nuclear Engineering  
December 4, 1985

Certified by

\_\_\_\_\_  
Sidney Yip  
Thesis Supervisor

Accepted by

\_\_\_\_\_  
Allan F. Henry  
Chairman, Departmental Committee on Graduate Students

ATOMISTIC SIMULATION STUDY OF  
VACANCY CLUSTERS IN COPPER

by

Michael John Sabochick

Submitted to the Department of Nuclear  
Engineering on December 4, 1985 in partial  
fulfillment of the requirements for the degree  
of DOCTOR OF PHILOSOPHY.

Abstract

Defect properties of copper are calculated using molecular statics with an interatomic potential recently derived from first principles. Tri- and tetravacancies are found to be very mobile with migration energies of 0.56 and 0.39 eV, respectively, compared to previously calculated single and divacancy migration energies of 0.82 and 0.55 eV, respectively. Using the binding and migration energies calculated with the interatomic potential, annealing kinetics in copper are modeled using rate equations. The effective activation energy of annealing in the model is within 0.02 eV of single vacancy migration energy over a wide range of sink and initial single vacancy concentrations, which conforms to experimental results. In two cases, however, the larger clusters affect the activation energy and no definitive conclusions about whether or not the calculated cluster migration energies are correct for copper can be made.

The stability and structure of larger vacancy clusters with ten to forty vacancies were also investigated using the first principles copper potential. The stacking fault energy was first calculated and, for the potential cutoff radius used in the defect calculations, yielded of a value of 65 mJ/m<sup>2</sup> compared to the experimental value of ~70 mJ/m<sup>2</sup>. To investigate the large clusters, vacancy platelets of various sizes were created in a close-packed plane and the system was relaxed to the minimum energy configuration. Small vacancy platelets with as few as ten vacancies collapsed into stacking fault tetrahedra

and faulted loops, depending on the shape of the platelet. Stacking fault tetrahedra are found to be the most stable large clusters.

In order to investigate the range applicability of the potential, molecular dynamics calculations of thermodynamics and vibrational properties were performed. Parallel calculations were also done using an empirical potential. It was found that the agreement between calculated and experimental properties was much better at low temperatures than at temperatures near melting for both potentials. Neither potential was found to be significantly better than the other for thermodynamic calculations.

A first principles potential for silver was also used to calculate defect migration and thermodynamic properties. The divacancy is found to be the most mobile vacancy cluster, followed by tetra-, tri-, and single vacancies. Combined with the copper results, it is concluded that di-, tri-, and tetravacancies are all highly mobile compared to single vacancy, and the relative order among the clusters depends on the potential. As with the copper potentials, the thermodynamic properties calculated using the silver potential were in good agreement with experimental results at low temperatures, but discrepancies were found at high temperatures.

Thesis Supervisor: Sidney Yip  
Title: Professor of Nuclear Engineering

Thesis Reader: Ronald G. Ballinger  
Title: Assistant Professor of Nuclear  
Engineering

-4-

For Lillian and John

Table of Contents

|   |     |
|---|-----|
| Abstract                                | 2   |
| Table of Contents                       | 5   |
| List of Figures                         | 7   |
| List of Tables                          | 9   |
| Acknowledgments                         | 10  |
| 1. Introduction                         | 11  |
| 2. Interatomic Potentials for Copper    | 20  |
| 2.1 Introduction                        | 20  |
| 2.2 Empirical Potentials                | 22  |
| 2.3 Pseudopotentials                    | 27  |
| 3. Molecular Dynamics                   | 37  |
| 3.1 Introduction                        | 37  |
| 3.2 Integration Scheme                  | 40  |
| 3.3 Boundary and Initial Conditions     | 44  |
| 3.4 Time-Saving Methods                 | 47  |
| 3.4.1 Verlet Neighbor List              | 49  |
| 3.4.2 Evaluation of the Potential       | 51  |
| 3.5 Thermodynamic Property Calculations | 55  |
| 3.6 The Parrinello-Rahman Method        | 58  |
| 4. Molecular Statics                    | 64  |
| 4.1 Introduction                        | 64  |
| 4.2 Review of Molecular Statics Methods | 67  |
| 4.3 A New Method                        | 72  |
| 4.4 Comparisons of Methods              | 76  |
| 4.5 Defect Energy Calculations          | 79  |
| 4.5.1 Formation Energy                  | 79  |
| 4.5.2 Binding Energy                    | 87  |
| 4.5.3 Migration Energy                  | 88  |
| 5. Bulk Properties                      | 99  |
| 5.1 Introduction                        | 99  |
| 5.2 Thermodynamic Properties            | 100 |
| 5.3 Vibrational Properties              | 127 |
| 5.4 Discussion                          | 131 |
| 6. Small Vacancy Cluster Migration      | 134 |
| 6.1 Introduction                        | 134 |
| 6.2 Migration Energy Calculations       | 135 |
| 6.3 Annealing Kinetics                  | 141 |

|   |     |
|---|-----|
| 6.4 Discussion                                | 161 |
| 7. Large Clusters                             | 168 |
| 7.1 Introduction                              | 168 |
| 7.2 Stacking Fault Energy                     | 169 |
| 7.3 Large Cluster Configurations and Energies | 172 |
| 7.4 Discussion                                | 189 |
| 8. Silver Properties                          | 193 |
| 8.1 Introduction                              | 193 |
| 8.2 Thermodynamic Properties                  | 198 |
| 8.3 Small Cluster Migration                   | 200 |
| 8.4 Discussion                                | 208 |
| 9. Conclusions                                | 214 |



# List of Figures

|              |   |     |
|--------------|---|-----|
| Figure 2-1:  | Copper Potentials   | 35  |
| Figure 3-1:  | Periodic Boundaries   | 48  |
| Figure 3-2:  | Implementation of Verlet Neighbor List                          | 52  |
| Figure 3-3:  | Simulation Volume of a Flexible Boundary System                 | 62  |
| Figure 4-1:  | Conventional Algorithm for Fletcher's Method                    | 74  |
| Figure 4-2:  | Modified Algorithm for Fletcher's Method                        | 77  |
| Figure 4-3:  | Comparison of MS Methods for Case 1                             | 80  |
| Figure 4-4:  | Comparison of MS Methods for Case 2                             | 81  |
| Figure 4-5:  | Comparison of MS Methods for Case 3                             | 82  |
| Figure 4-6:  | Vacancy Jump in a Square Lattice                                | 91  |
| Figure 4-7:  | Migration Path for a Vacancy Jump                               | 93  |
| Figure 4-8:  | Effect of Constraint on the Potential Energy                    | 97  |
| Figure 5-1:  | MSD vs Temperature for Dagens' Potential                        | 109 |
| Figure 5-2:  | MSD vs Temperature for the Modified Morse Potential             | 110 |
| Figure 5-3:  | Total Energy vs Temperature for the Pseudopotential             | 113 |
| Figure 5-4:  | Enthalpy vs Temperature for the Modified Morse Potential        | 114 |
| Figure 5-5:  | Pressure vs Temperature for Dagens' Potential                   | 116 |
| Figure 5-6:  | Volume vs Temperature for the Modified Morse Potential          | 117 |
| Figure 5-7:  | Order Parameter vs Temperature for Dagens' Potential            | 119 |
| Figure 5-8:  | Properties During a Modified Morse Potential Melting Transition | 124 |
| Figure 5-9:  | VACF at ~298K   | 129 |
| Figure 5-10: | Frequency Spectra at ~298K                                      | 130 |
| Figure 6-1:  | Vacancy Cluster Configurations in Copper                        | 139 |
| Figure 6-2:  | Copper Trivacancy Migration Mechanisms                          | 142 |
| Figure 6-3:  | Copper Trivacancy Migration Barriers                            | 143 |
| Figure 6-4:  | Copper Tetravacancy Migration Mechanism                         | 144 |
| Figure 6-5:  | Copper Tetravacancy Migration                                   | 145 |

|              |  |     |
|--------------|--|-----|
| Barriers     |  |     |
| Figure 6-6:  | Results of an Annealing Run                                      | 159 |
| Figure 7-1:  | Schematic of System for Calculating<br>the Stacking Fault Energy | 171 |
| Figure 7-2:  | Shapes of Vacancy Platelets<br>Introduced into (111) Plane       | 174 |
| Figure 7-3:  | Displacement Field above the<br>Vacancy Hexagon                  | 176 |
| Figure 7-4:  | Displacement in z-direction Above<br>Vacancy Loop                | 177 |
| Figure 7-5:  | Displacement in z-direction Above<br>Vacancy Loop                | 178 |
| Figure 7-6:  | (111) Planes at the Face of an SFT                               | 180 |
| Figure 7-7:  | Cross-Section of 21-Vacancy SFT                                  | 181 |
| Figure 7-8:  | (110) Cross-Section of Rhombus                                   | 184 |
| Figure 7-9:  | (112) Cross-Section of Rhombus                                   | 185 |
| Figure 7-10: | (111) Planes above and below<br>Rhombus                          | 186 |
| Figure 7-11: | Binding Energies of Large Clusters                               | 188 |
| Figure 8-1:  | Silver Thermodynamic Properties                                  | 199 |
| Figure 8-2:  | Silver Bulk Modulus Calculations                                 | 201 |
| Figure 8-3:  | Silver Trivacancy Configurations                                 | 204 |
| Figure 8-4:  | Silver Migration Mechanisms                                      | 206 |
| Figure 8-5:  | Silver Trivacancy Migration Energy<br>Barrier                    | 207 |
| Figure 8-6:  | Tetravacancy Configurations                                      | 209 |

# List of Tables

|                   |   |     |
|-------------------|---|-----|
| <u>Table 2-1:</u> | Interatomic Potential Parameters for        | 34  |
|                   | Noble Metals (from Lam <sup>1</sup> et al ) |     |
| <u>Table 3-1:</u> | Values of $\alpha_i$ for Gear Predictor-    | 42  |
|                   | Corrector Algorithm                         |     |
| <u>Table 5-1:</u> | Simulation Volumes Used in Property         | 103 |
|                   | Calculations with Dagens' Copper Potential  |     |
| <u>Table 5-2:</u> | Thermodynamic Properties of Dagens'         | 105 |
|                   | Potential (Part I)                          |     |
| <u>Table 5-3:</u> | Thermodynamic Properties of Dagens'         | 106 |
|                   | Potential (Part II)                         |     |
| <u>Table 5-4:</u> | Thermodynamic Properties of Modified        | 107 |
|                   | Morse Potential (Part I)                    |     |
| <u>Table 5-5:</u> | Thermodynamic Properties of Modified        | 108 |
|                   | Morse Potential (Part II)                   |     |
| <u>Table 5-6:</u> | Derived Thermodynamic Properties            | 121 |
| <u>Table 6-1:</u> | Comparison of Copper Results with Lam       | 138 |
|                   | <sup>1, 3</sup> et al                       |     |
| <u>Table 6-2:</u> | Binding Energies of Tri- and                | 140 |
|                   | Tetravacancies in Copper                    |     |
| <u>Table 6-3:</u> | Binding and Migration Energies of           | 147 |
|                   | Small Vacancy Clusters in Copper            |     |
| <u>Table 6-4:</u> | Reactions of Vacancy Defects with one       | 152 |
|                   | another and with Internal Sinks             |     |
| <u>Table 6-5:</u> | Values of the Physical Parameters           | 156 |
|                   | Used in Equations (6.12) and (6.13)         |     |
| <u>Table 6-6:</u> | Average Effective Activation Energies       | 160 |
|                   | of Anneals (eV)                             |     |
| <u>Table 6-7:</u> | Temperatures for Maximum Annealing          | 161 |
|                   | [K]   |     |
| <u>Table 7-1:</u> | Comparison of Stacking Fault Energy         | 172 |
|                   | Calculations                                |     |
| <u>Table 7-2:</u> | Binding Energies of Large Clusters          | 187 |
| <u>Table 8-1:</u> | Comparison of Silver Thermodynamic          | 200 |
|                   | Properties                                  |     |
| <u>Table 8-2:</u> | Comparison of Silver Results                | 202 |
| <u>Table 8-3:</u> | Binding Energies of Silver Vacancy          | 205 |
|                   | Clusters                                    |     |
| <u>Table 8-4:</u> | Silver Migration Energies                   | 205 |
| <u>Table 8-5:</u> | Defect Annealing Values in Silver           | 211 |

Acknowledgments

It is a pleasure to thank Professor Sidney Yip for his guidance and help during the course of my work. I appreciate that he tried to go beyond just teaching me facts, but also tried to teach me to learn and contribute. Although the road was not always easy, he had my concerns in mind and wanted me to do the best I could possibly do.

Dr. N. Q. Lam of Argonne National Laboratory was very helpful with discussions and suggestions. I am particularly grateful to him for taking the time to review the drafts of my thesis. I also want to thank Professor R. G. Ballinger at M.I.T. for critically reading the drafts.

I want to acknowledge the extensive financial support which was provided to me by the United States Air Force. In particular, I also want to thank Professor C. J. Bridgman at the Air Force Institute of Technology (AFIT) for believing in my abilities and making it possible for me to continue my studies at the M.I.T.

The National Science Foundation provided some funds for parts of the computational work, and I must acknowledge Project Athena at M.I.T. for program development resources.

Finally, I thank my wife, Lillian, for helping me over the rough spots.

Chapter 1  
Introduction

The technological importance of vacancies and small vacancy clusters in materials has led to a considerable research effort toward studying their effects. For many reasons this has not been an easy task. The primary difficulty is the small size of these defects which is on the order of a few lattice constants. This makes it difficult to identify and distinguish from among vacancies and small vacancy clusters and has often forced experimentalists to use macroscopic properties to quantify defect concentrations. For example, single vacancy migration energies have been estimated for most metals using annealing experiments in which the electrical resistivity is used as a measure of vacancy concentration. As Balluffi<sup>4</sup> summarizes, this method has many drawbacks, and the single vacancy migration energies of some metals have only recently been reliably determined after twenty years of experiments.

In the case of copper, there is very little experimental information about small vacancy clusters. Although the experimental values of single vacancy formation and migration energy are fairly well

established<sup>4</sup>, the binding and migration energies of larger clusters are unknown. Annealing studies done by Wienhold<sup>5</sup> et al have suggested that at least one vacancy cluster is as mobile as the single vacancy in copper. This is confirmed by perturbed angular correlation (PAC) studies of annealing in copper done by Wichert<sup>6</sup> et al and Deicher<sup>7</sup> et al in which there appears to be a second mobile vacancy-type defect in addition to the single vacancy. Neither of these methods has been able to specifically identify the size of the cluster, although it is assumed to be a divacancy since theoretically divacancies are<sup>4</sup> believed to be more mobile than single vacancies.

Defects involving larger vacancy clusters, dislocation loops and stacking fault tetrahedra (SFT), can be identified using electron microscopy<sup>8</sup> and the size distributions of loops can be determined using diffuse X-ray scattering<sup>9</sup>. Recently Larson and Young<sup>9</sup> analyzed the size distribution of dislocation loops in copper using diffuse X-ray scattering and found loops which were apparently as small as about 10-15Å in radius. This conflicted with earlier electron microscopy studies which found loops as small as about 25Å<sup>10</sup>. Larson pointed out that diffuse X-ray scattering should be better for analyzing small loops, although it does not allow one to image defects but only produces a size distribution. The

diffuse X-ray scattering data in copper is interpreted using anisotropic elasticity theory<sup>9, 11</sup>. Although these results are no doubt more reliable than the previous studies using isotropic theory, it is well-known that the assumptions behind elasticity theory break down near<sup>12</sup> dislocation cores.

With these uncertainties in basic defect properties of copper, it is evident that computational and theoretical methods could contribute important information to the current understanding. The purpose of this work is to resolve some of these questions about the properties of small vacancy defects in copper using the computational methods of molecular statics (MS) and molecular dynamics (MD). In these methods the material is represented by a collection of atoms which interact with one another through a given interatomic potential. This work is a particularly timely application of MS and MD, since an interatomic potential recently derived by Dagens using the<sup>13, 14, 15</sup> pseudopotential method is employed.

<sup>16</sup>The pseudopotential method is used to derive potentials from first principles and with a minimum amount of experimental information. Even with this justification, however, the potential must be able to duplicate existing experimental results to be considered reliable. The quantities so far calculated using the potential derived by Dagens, which include the most stable

lattice type<sup>15</sup>, the elastic constants<sup>15</sup>, phonon frequencies<sup>17</sup>, and the properties of single vacancies<sup>1</sup>, all agree well with experimental values for copper. In this work the verification of the potential is further extended by the calculation of basic thermodynamic properties and vibrational properties. The bulk modulus and phonon frequencies are also calculated to insure that the computer implementation is correct since these can be compared with previous calculations. It should be pointed out that these results are for nonzero temperatures using molecular dynamics while the previous calculations were done using techniques at zero or low temperatures.

The defect calculations in this work for the most part follow standard methods in this area. The first attempt to calculate the displacement field around a single vacancy was made by Girifalco and Streetman in 1958<sup>18</sup>. This work applies to BCC metals; in 1960 Girifalco and Weizer made a more complete study of vacancy relaxation in cubic metals using a Morse potential<sup>19</sup>. Tewordt used two Born-Mayer potentials to calculate properties of various point defects in copper in 1958<sup>20</sup>. This work is significant because it was the first case where an atomistic or discrete method was combined with elastic theory. In 1965 Johnson reported on the first calculations of both the single and divacancy migration



energies using a copper potential<sup>21</sup>. Using a potential for nickel (the Johnson I potential), Johnson later reported calculations on the formation and migration energies of larger clusters and discovered a simple relationship describing these values<sup>22</sup>. In 1966 Cotterill<sup>12</sup> and Doyama published a work on the investigation of the edge dislocations in copper using a Morse potential; they also reported calculations for the stacking fault energy using Born-Mayer and Morse potentials. In 1975 Bennett discussed the method used to calculate the migration energy in static systems in this work<sup>23</sup>.

The first application of molecular dynamics to thermodynamic property calculations was done by Alder in 1959<sup>24</sup>. Rahman was the first to use continuous potentials for these calculations in 1964<sup>25</sup>. The original calculations were for liquids; Dickey and Paskins<sup>26</sup> calculated the properties of solids in 1969. These studies were performed on microcanonical, i.e., constant volume, systems. Andersen suggested a way of doing constant pressure simulation in 1980 in which the system volume was allowed to expand and contract<sup>27</sup>. Parrinello and Rahman subsequently did calculations using a technique in which the boundaries change shape as well as volume<sup>28</sup> which permitted the lattice structure to change.

From this review it is apparent that MS and MD, as

applied to defect and thermodynamic property calculations in this work, are well-established methods. Except for the flexible boundary method, the general techniques in these areas have not changed significantly. The molecular statics method has become computationally faster and new methods have been presented for calculating properties such as elastic constants. It is interesting to note, however, that there has not been much cross-fertilization between workers in defect and thermodynamic property calculations. Apparently the only potential which has been extensively investigated by workers in both areas is the Lennard-Jones 6-12 potential for argon and other noble gases. This potential is not as applicable to metals as other potentials, however, and the defect properties of metals are of much greater technological interest than those of argon. In this work a single potential is used to represent copper. The hypothesis that a single interatomic potential can be used to successfully calculate many different properties of a material is being tested.

The outline of this work is as follows. In Chapter 2 the potential used in this work is described in detail and compared to some previous potentials used for copper. The difference between empirical and first principles potentials are emphasized, and some of the major disadvantages and necessary assumptions related to the

potential used in this work are pointed out. The computational methods used in this work, molecular dynamics and molecular statics, are discussed in Chapters 3 and 4, respectively. The molecular dynamics method as used in this work is covered, including the flexible<sup>28</sup> boundary technique of Parrinello and Rahman. A new molecular statics method which is an order of magnitude or more faster than previous methods is presented in Chapter 4.

The method and results of thermodynamics calculations are presented in Chapter 5. Dagens' potential<sup>15, 1</sup>, derived from pseudopotential theory, and the empirical<sup>29</sup> Morse potential, both reproduce copper properties at low temperatures better than at high temperatures. The reason for the good performance at low temperatures is that both potentials (especially Dagens' potential) are particularly good at reproducing the phonon spectra.

Chapter 6 is devoted to the evaluation of migration energies of tri- and tetravacancies. Molecular statics results show that in the order of increasing mobility, small vacancy defects in copper are single vacancies, trivacancies, divacancies, and tetravacancies. To investigate the experimental consequences of the migration energies, rate equations describing vacancy defects in copper are used to model annealing kinetics. In most cases, it is found that the migration energies of the

divacancies and larger clusters do not affect the effective activation energy, which agrees with experimental observations<sup>4, 5</sup>. It is also concluded that the migration energies of defects are sensitive to the potential and are not readily predictable based on the results for other potentials.

Stacking fault and large vacancy cluster calculations are presented in Chapter 7. The stacking fault energy is found to have the same order of magnitude as experimental predictions if the potential is not extended beyond twelve nearest neighbors. It appears that the analytic form of the interatomic potential which is fitted to pseudopotential results<sup>1</sup> is inaccurate at large radii. Vacancy platelets with as few as ten vacancies are found to collapse to form stable and metastable clusters. The most stable vacancy clusters are those which arise from vacancy platelets in the shape of triangles, rhomboids, and hexagons, in order of decreasing stability. The triangular platelets invariably form stacking fault tetrahedra (SFT), the hexagons form Frank loops, and the rhomboids form a complex intermediate configuration. The displacement field immediately above the hexagonal loops is found to differ greatly from anisotropic elasticity theory<sup>30</sup>, which has been used to interpret diffuse X-ray scattering data<sup>9, 11</sup>.

The general pseudopotential theory developed by

Dagens is applicable to silver in addition to copper<sup>13, 14, 15</sup> and Lam et al<sup>1</sup> has given the potential parameters for both metals. In Chapter 8, preliminary calculations using the silver potential are presented. These silver results are found to support the general conclusions of the results in Chapters 5, 6, and 7.

## Chapter 2

### Interatomic Potentials for Copper

#### 2.1 Introduction

Molecular dynamics (MD) and molecular statics (MS) can be used to simulate a wide range of material properties and behavior. Both micro- and macroscopic properties can be calculated such as the vacancy formation energy and the elastic constants. Regardless of the property being simulated, however, MD and MS both require that the interatomic potential be given. The power of these methods is that if one knows how atoms interact on an atomistic level, many other properties can be calculated without further assumptions. In practice, limitations on computational resources make it necessary to restrict interactions between atoms to relatively short range, and the the system size a few hundred or thousand atoms. It is well recognized that one's ability to predict the behavior of a real material depends on the interatomic potential which is used, and that the availability of a suitable interatomic potential is crucial to a successful computer simulation study.

Another point concerning potentials which applies to

this work is the difference between ideal and real metal simulations. The properties of an ideal metal are those which pertain to metals in general. Real metal properties, however, are those which distinguish a particular metal from others. An example of an ideal metal property is that divacancies are believed to be more mobile than single vacancies in fcc metals<sup>4</sup>. A molecular statics simulation which uses an interatomic potential for a metal would be expected to find that the divacancy migration energy is less than the single vacancy migration energy, and hence that divacancies are more mobile than single vacancies. On the the other hand, the actual values of the single and divacancy migration energies of a metal are real metal properties since they are peculiar to that metal. An interatomic potential for that particular metal must be used if one has any hope of calculating these values. This distinction between ideal and real metal simulations is important to this work since we are interested in calculating the properties of real copper.

In this Chapter the potential functions cited and/or used in this work will be discussed. In the following section a general background will be given for empirical potentials, including some of their strengths and weaknesses. The empirical potentials are used mostly for comparison here (some thermodynamic calculations are performed) and this discussion does not really do them

justice. It should also be pointed out that "empirical" in this work refers to potentials for which experimental vs. first principles input is emphasized, which does not follow standard usage<sup>31</sup>, and this point will be briefly discussed. Following the discussion of empirical potentials, the pseudopotential method will be discussed in a general way and the potential of Dagens used in this work will be described in detail. Some important approximations that had to be made to use Dagens' potential are pointed out.

## 2.2 Empirical Potentials

In this work, interatomic potentials which are derived by a fit to experimental data will be referred to as empirical, although often a distinction is made between empirical and semi-empirical potentials<sup>31</sup>. In both cases, the free parameters of a functional form are fitted to reproduce an experimentally measured property or properties. The functional form of a semi-empirical potential is given in advance of the fit and is suggested more by the general properties of the material (e.g., a stable cubic crystal) than by the properties which are actually being fitted. The functional form of a true empirical potential, however, is suggested by the property or properties to which it is being fitted<sup>31</sup>. The potential consists of splines or connected polynomials



which can represent a very general function. Except for the copper potential of Baskes and Melius<sup>32</sup> briefly discussed below, the potentials discussed in this section are properly called semi-empirical potentials. Throughout the work, however, all potentials except for the interatomic potential derived by Dagens' from pseudopotential theory will be called empirical potentials.

The general idea behind empirical potentials is to assume that the interatomic potential can be represented using a fairly simple functional form, at least over interatomic interaction radii which are important to the property or properties of interest. The functional form contains a few independent parameters which can be fitted to give the correct results for a few given properties under very specific conditions. For example, one could fit a potential to the elastic constants of a material at a temperature of absolute zero. It is then assumed that the general form of the potential is accurate enough to use it for other properties (interstitial formation energy, vacancy migration energy, etc.) and other conditions (e.g.,  $T > 0$ ).

One difficulty with empirical potentials is that the functional parameters are not in general unique and depend on the material property and conditions used for the fit. This problem can be rationalized in three ways. The first

is that the form of the potential is not general enough to simulate the "true" potential, i.e., the way that real atoms interact. For real materials this is true: one cannot find a single potential to represent atom-atom interactions under all conceivable conditions. One solution to this could be to generalize the potential further, but simultaneously fitting many properties is difficult and it is not clear that the potential will be more realistic. The second explanation is that any form of central potential is insufficient to represent interatomic interactions since nonlocal interactions may be important. This means that any form of central potential, even as general as a table of values, will not be sufficient under all conditions. This is a justification for using empirical vs. pseudopotential methods. If a single central potential valid for all properties does not exist, perhaps it is better use an empirical potential suggested by and fitted to the properties in which we are interested than to go to all the trouble to derive an interatomic potential from pseudopotential theory. Finally, all interatomic potentials are in the end justified by their ability to reproduce experimental results. Even if a potential has some justification of a first principles derivation, to be useful it must be able to perform well in simulations. Hence, there are valid reasons for using empirical potential in spite of their disadvantages.

Among the different forms of empirical potentials, three are referenced in this work. The first is the Born-Mayer potential,

$$u(r_{ij}) = L \exp(-\gamma r_{ij}) \quad (2.1)$$

where  $r$  is the interatomic distance and  $u$  is the potential energy. This potential was not used for any calculations here, but is cited for stacking fault results by Cotterill and Doyama<sup>12</sup>. The values of the parameters are  $L = 0.053$  ev and  $\gamma = 13.9 \text{ \AA}^{-1}$ , from Gibson et al<sup>33</sup>. Since the Born-Mayer potential does not contain an attractive part, an external pressure must be applied to the system to maintain a given density. This is a problem shared with pseudopotentials, except that the external force can in principle be calculated for the pseudopotentials.

The second empirical potential cited in this work is the Morse potential,

$$u(r_{ij}) = D \{ \exp[-2\alpha(r_{ij} - r_0)] - 2 \exp[-\alpha(r_{ij} - r_0)] \} \quad (2.2)$$

where  $D$ ,  $\alpha$ , and  $r_0$  are constants to be specified. Cotterill and Doyama used a Morse potential in a study of edge dislocations and stacking fault energies in copper<sup>12</sup>. The potential was fitted to the sublimation energy of copper, and the parameters for a truncation radius at 176

atoms are  $D = 0.3236$  ev,  $\alpha = 1.2941 \text{ \AA}^{-1}$ , and  $r_0 = 2.9133 \text{ \AA}$ .

The third empirical potential is a modified Morse potential used by Schober et al<sup>29</sup> to calculate interstitial properties. The functional form of this potential is

$$u(r_{ij}) = D \{ \exp[-2\alpha(r_{ij} - r_0)] - 2 \exp[-\alpha(r_{ij} - r_0)] \} + B(r_{ij} - r_{NN})^4 H(r_{ij} - r_{NN}) + V_0 \quad (2.3)$$

where

$$H(x) = \begin{cases} 1, & x < 0 \\ 0, & x \geq 0 \end{cases} \quad (2.4)$$

The extra terms, compared with equation (2.2), makes the potential softer in the nearest neighbor region and provides two more parameters which can be used for fitting properties<sup>29</sup>. This potential was fitted to the vacancy formation energy and elastic constants of copper and the potential parameters are  $D = 0.227$  ev,  $r_0 = 0.71555a$ ,  $\alpha = 7.6499a^{-1}$ ,  $B = -1200 \text{ ev} / a^4$ ,  $V_0 = 0.0233$  ev, and  $r_{NN} = a / 2^{1/2}$ , where  $a$  is the lattice constant. Since this potential was fitted to more recent values of the

vacancy formation energy and was also fitted to the bulk modulus, it is used in Chapter 5 to do thermodynamic calculations of copper for comparison with the Dagens' interatomic potential discussed below.

An empirical potential recently derived by Baskes and Melius<sup>32</sup> was also considered. Baskes and Melius did a true empirical fit for seven fcc metals to a large number of properties, and had a separate term for the cohesive electron energy (the structure-independent term in the pseudopotential). Unfortunately, they apparently used outdated values for the vacancy formation and migration energies<sup>4</sup> in the fit for copper (see Balluffi<sup>5</sup> and Wienhold for recent estimates of these values). De Leeuw et al used this potential to calculate copper properties near the melting point and found that a significant external pressure had to be applied to maintain the correct density<sup>34</sup>. Because of these problems this potential was not used in this work.

### 2.3 Pseudopotentials

There is a long history behind the pseudopotential method, and the classic work was published by Harrison in 1966<sup>16</sup>. The pseudopotential method is an attempt to derive interatomic potentials from first principles. It takes advantage of the free-electron nature of the conduction electrons in metals, which are free to roam

throughout the metal instead of being associated with individual atoms. The metal is separated into two components: the conduction electrons, which are represented by some type of average interaction, and the metallic ions, whose electrons are tightly bound<sup>16</sup>. The strong potential inside the metallic ions is then replaced by a weaker potential which preserves the energy eigenvalues of the conduction electrons<sup>31</sup>. The original pseudopotential method proposed by Harrison did not require experimental information to be introduced into the derivation of potential. Since the late 1960's, however, modifications of the method which incorporate some experimental data have proven more successful for some<sup>35, 36, 37</sup> metals than the pure pseudopotential approach. After discussing some general aspects of pseudopotentials, the potential used in this work will be covered.

Interatomic potentials derived from pseudopotential methods have some common characteristics. The first is that the potentials are oscillatory beyond a range of about one lattice constant<sup>38</sup>. These oscillations converge to the Friedel oscillations at long range. Whether or not these oscillations are physically significant is not well-established<sup>39, 37</sup>. One practical consequence of the oscillations is that these potentials are long-ranged and must be truncated to be used for molecular dynamics and statics. This can lead to convergence difficulties,

especially for properties which depend on the long-range part of the potential.

A second characteristic of the potentials is they contain structure-dependent and independent components which arise from the treatment of the free electrons. If the total cohesive energy of the crystal is included in the interatomic pair potential  $u_{ij}$ , the total energy  $E$  can be written

$$E = \sum_{i < j} u(r_{ij}) \quad (2.5)$$

where  $r_{ij}$  is the distance between atoms  $i$  and  $j$ . Equation (2.5) is valid for many empirical pair potentials including the Morse and modified-Morse potentials discussed in the previous section. In metals, however, and particularly when the pseudopotential method is used,<sup>40</sup> the total cohesive energy is given by

$$E = \sum_{i < j} u(r_{ij}; V) + U(V) \quad (2.6)$$

The first term in (2.6), similar to the right-hand side of (2.5), is the structure-dependent component of the total energy and depends on the positions of the atoms. This part of the potential is used directly in molecular dynamics since it describes how one atom interacts with another. The second term of (2.6) is the structure-independent component and depends only on the system volume and not on the positions of the atoms. It

physically represents the cohesive energy provided by the conduction electrons, which are not directly simulated. It is not necessary to know the structure-independent part of the potential to calculate many properties of the material. For example, if we wanted to determine the stable lattice configuration or calculate defect formation energies at a given density, we would only need the structure-dependent part of the potential. For this reason the structure-independent component is not always provided in derivations of pseudopotentials. This is unfortunate since the volume derivative of the total energy is the system pressure, and this derivative obviously depends on the second term of (2.6). When the structure-independent component is known, it adds an extra complication to direct thermodynamic and mechanical property calculations. When it is unknown, some thermodynamic properties simply cannot be evaluated.

To make matters worse, the structure-dependent component of the potential is also volume dependent. Hence, the form of the interatomic potential  $u(r; V)$  depends on the density of the system. If simulations are done at the same volume  $V_0$ , a single interatomic potential  $u(r; V_0)$  can be used and the structure-independent component  $U(V_0)$  is not necessary as long as it is sufficient to calculate the total energy within a constant. To compare calculations at a different volume



$V_1$ , however, we not only need to know the structure-independent component  $U(V_1)$ , but we also need a different interatomic potential  $u(r; V_1)$ .

Another complication in using pseudopotentials in molecular dynamics and molecular statics calculations is that they generally do not come in a simple functional form. The interatomic potential calculated using the pseudopotential method consists of a table of values of energy vs. interatomic radius. In principle this is not a problem; one can calculate the table to any desired accuracy with sufficient computer resources, and the table can be interpolated using standard numerical methods such as splines. However, it requires a considerable amount of space to publish a table of sufficient accuracy for all calculations, and programming would be tedious and prone to error using such a table from a paper. The pseudopotential method is difficult enough to preclude each worker from repeating the calculations to get the interatomic potential function, especially using the advanced methods necessary to get the best interatomic potential. One solution to this dilemma is to fit the interatomic potential generated by the pseudopotential method to a very general functional form suggested by the physics of interatomic interactions and the structure of the interatomic potential itself. Of course, the function to which we are fitting the pseudopotential interatomic

potential should not be so complicated that it also causes difficulties.

In spite of all of these problems there still is much interest in developing and using interatomic potentials derived from pseudopotential theory. The reasons are that the potentials are better justified theoretically than empirical potentials, and also that the pseudopotential methods provide a theory of interatomic interactions in metals.

The interatomic potential used in this work is based on the work of Dagens<sup>13, 14, 15</sup>. This was the culmination of attempts to account for the d-band in the noble metals<sup>41, 42</sup>. Harrison had previously noted that a basic assumption behind the pseudopotential method was that the core and conduction electrons could be cleanly separated such that the core of the atom could be treated as an ion<sup>43</sup>. The assumption only strictly holds for the alkali and polyvalent metals for which reliable interatomic potentials have been derived using the pseudopotential method. Unfortunately, the assumption breaks down in noble and transition metals.

The results of Dagens' calculations were fitted to a general interatomic potential of the form<sup>1</sup>

$$u(r) = \{1 - \exp[-\alpha(r-r_1)^2]\} \times$$

$$\left[ \left( C_0 + \frac{C_1}{r^2} \right) \frac{\cos \chi}{r^3} + \frac{S_1 \sin \chi}{r^5} \right] +$$

$$\sum_n \frac{B_n \exp(-\beta r^2)}{r^{3-n}} +$$

$$D \exp(-\gamma r) \quad (2.7)$$

where  $\chi \equiv \psi + 2k_F r$ .

The parameters for the fit are given in Table 2-1. The parameters for silver are also included in Table 2-1, as this potential will be used in Chapter 8. The copper potentials discussed in this Chapter are plotted in Figure 2-1. The differences between the various potentials is striking when it is considered that they are all for the same metal. As Lam<sup>1</sup> points out, the copper potential has a minimum near the first nearest neighbor radius. Whether or not this is physically realistic is not well-established<sup>37</sup>.

It was not possible to determine the structure-independent part of the potential for this work; apparently, this is a very difficult task<sup>44</sup>. This does not affect the defect calculations presented in this work,

|          | <u>Cu</u> | <u>Ag</u> |
|----------|-----------|-----------|
| $\alpha$ | 0.2       | 0.1       |
| $r_1$    | 3         | 3         |
| $C_0$    | 0.265     | 0.186     |
| $C_1$    | -0.252    | 1.34      |
| $S_1$    | -20.85    | -22.05    |
| $\psi$   | 1.429     | 1.528     |
| $\beta$  | 0.163     | 0.109     |
| $B_0$    | 16.55     | 17.669    |
| $B_1$    | -0.0033   | -0.459    |
| $B_2$    | 0.0825    | -0.2044   |
| $B_3$    | -0.1576   | -0.02728  |
| $\gamma$ | 0.74      | 0.8       |
| D        | 0.1246    | 0.2819    |
| $k_F$    | 0.7189    | 0.6387    |

Table 2-1: Interatomic Potential Parameters<sup>1</sup>  
for Noble Metals (from Lam et al )

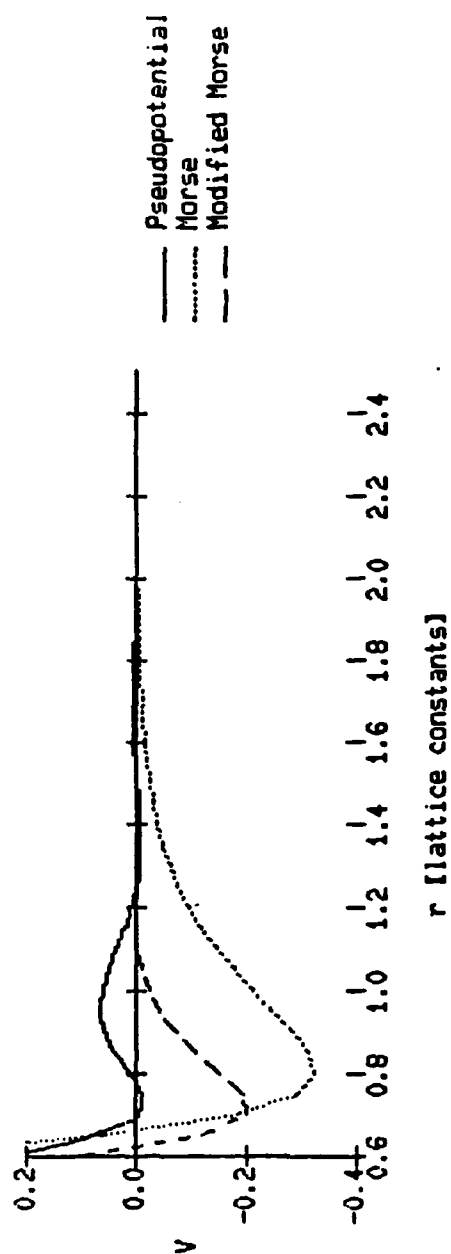


Figure 2-1: Copper Potentials

but it made it impossible to calculate the pressure for the thermodynamic calculations. This problem will be discussed in more detail in Chapter 5.

As pointed out earlier in this Chapter, the interatomic potentials derived using the pseudopotential method are long-ranged. To overcome this difficulty, Duesbury et al<sup>45</sup> developed a damping factor for the potential  $u(r)$  such that

$$u^{eff}(r) = u(r) \exp(-d^2 r^2) \quad (2.8)$$

where  $u^{eff}(r)$  is the potential actually used in the molecular statics calculations. Following Lam<sup>1</sup>, the copper calculations using the Dagens' potential were done using  $d = 0.25 a^{-1}$ , where  $a$  is the lattice constant.

### Chapter 3 Molecular Dynamics

#### 3.1 Introduction

The thermodynamic properties of copper were calculated in this work using a technique called computational molecular dynamics (MD). In MD one solves the equations of motion of  $N$  atoms subject to a given interatomic potential using a computer. Given  $N$  atoms with coordinates  $\underline{r}_i$  and velocities  $\underline{v}_i$ ,  $1 \leq i \leq N$ , one solves the set of equations

$$m \frac{d\underline{v}_i(t)}{dt} = - \sum_{j \neq i} \frac{du(r_{ij})}{dr_{ij}} \quad (3.1)$$

for  $\underline{r}_i(t)$  and  $\underline{v}_i(t)$ , where  $m$  is the atom mass,  $r_{ij}$  is the distance between atoms  $i$  and  $j$ , and  $u(r)$  is the interatomic potential. Many properties of the system such as its temperature, internal energy, and pressure, can be calculated since they can be expressed in terms of  $\underline{r}_i(t)$  and  $\underline{v}_i(t)$ .

The system that one simulates using conventional MD has a constant number of atoms  $N$ , a constant volume  $V$ , and a constant total energy  $E$ . This type of system is called a

microcanonical ensemble. The ensemble itself, which consists of all the possible configurations of the system with the given  $N$ ,  $V$ , and  $E$ , is uniquely specified by these values. Each configuration of the system has its own temperature and pressure, however, and the temperature and pressure of the ensemble is the average of these values over all the possible configurations in the ensemble. Even though the temperature and pressure of the ensemble are well-defined and unique, one cannot reliably estimate their values without taking an average over many configurations or MD time steps. Consequently, one cannot know the temperature and pressure of the ensemble which is being simulated until after the run is completed.

These characteristics of conventional MD affect its use for thermodynamic property calculations. As pointed out above, it is necessary to average the temperature and pressure (and other properties which fluctuate) over many time steps to determine the ensemble averages. There is no practical way to average over all possible configurations, since (classically) there are an infinite number of them, and the best one can do is get an estimate of a fluctuating property. It is important that "unlikely" configurations, i.e., configurations which are very unlikely to occur, are excluded because their property values will distort the averages. These unlikely configurations have the greatest chance of occurring at



the very beginning of the simulation, since as the simulation proceeds it will approach more probable configurations. Hence, it is important to select the initial configuration properly. The consequence of not knowing the temperature and pressure of the ensemble one is simulating until well into the simulation is that it is difficult to calculate ensembles with a given pressure and temperature. This is unfortunate since experimental properties of a material, especially those for solids, are usually presented at a given temperature and for atmospheric pressure. Without special techniques, the best one can expect to do is to calculate ensembles for various values of  $V$  and  $E$  and interpolate to the desired temperature and pressure. In this work, velocity-scaling is used to set the simulation temperature and the flexible boundary technique is used to set the simulation pressure.

In this Chapter the molecular dynamics method will be discussed. The integration scheme used to solve (3.1) for  $\underline{r}_i(t)$  and  $\underline{v}_i(t)$  is presented first. This is followed by a discussion of the initial and boundary conditions, which includes the selection of the initial configuration and velocity-scaling. The equations for calculating basic properties are given, and computational time-saving methods used in this work are discussed. Finally, the flexible border method is outlined.

### 3.2 Integration Scheme

The fundamental feature of molecular dynamics is the solution of the equations of motion given by (3.1). Except for simple cases it is not possible to solve these equations analytically and it is necessary to resort to numerical methods. Since the solution of these equations is so basic to computational molecular dynamics, the selection of the numerical integrating scheme is important. A detailed study of integration methods for MD applications has been made by Beeman<sup>46</sup>. The method which appears to be is a Gear-Nordsieck method discussed by Haile<sup>47</sup>. This method has three basic steps:

1. Prediction - use values of positions and derivatives at time  $t$  to estimate the positions and derivatives and  $t+\Delta t$ .
2. Evaluation - evaluate the potential function, i.e., the right hand side of (3.1), at the predicted positions.
3. Correction - using the results of the evaluated potential, correct the positions and derivatives.

Let  $\underline{r}_i^{(n)}(t)$  be the  $n^{\text{th}}$  derivative of the position of atom  $i$  and time  $t$ , and let  $\underline{r}_i^{P(n)}(t+\Delta t)$  be the predicted value of the  $n^{\text{th}}$  derivative of the position of atom  $i$  at time  $t+\Delta t$ . For an integrator of order  $p$ , we need the derivatives up to  $n = p$ . We estimate  $\underline{r}_i^{P(n)}(t+\Delta t)$  by expanding the Taylor series in  $\underline{r}_i(t)$  about  $t$ , where

$$\underline{r}_i^{(n)}(t+\Delta t) = \sum_{k=0}^{p-n} \frac{\underline{r}_i^{(n+k)}(t) (\Delta t)^k}{k!} \quad (3.2)$$

where  $p$  is the order of the integrator we wish to use.

The next step, and the core of a molecular dynamics code, is the evaluation of the potential for  $\underline{r}_i^{(n)}(t+\Delta t)$ . Most of the computer time in a molecular dynamics run is spent in this step, and many of the details of the implementation are buried here. These details, such as spatial boundaries which are imposed on the system and time-saving techniques for the evaluation of the potential, will be discussed in subsequent sections.

The evaluation of the right hand side of (3.1) yields, after dividing by the mass  $m$ , the second derivatives  $\underline{r}_i^{(2)}(t+\Delta t)$ . The difference between predicted value  $\underline{r}_i^{(2)}(t+\Delta t)$  and the calculated value  $\underline{r}_i^{(2)}(t+\Delta t)$  yields an estimate of the error in the prediction  $\Delta \underline{r}^{(2)}$ , where

$$\Delta \underline{r}^{(2)} = \underline{r}_i^{(2)}(t+\Delta t) - \underline{r}_i^{(2)}(t+\Delta t) \quad (3.3)$$

The error  $\Delta \underline{r}^{(2)}$  is now used to make corrections to all the derivatives where

$$\begin{aligned} \underline{r}_i^{(n)}(t+\Delta t) &= \underline{r}_i^{P(n)}(t+\Delta t) + \\ &\sum_n \Delta \underline{r}^{(2)} \frac{(\Delta t)^{n-2} n!}{2!} \end{aligned} \quad (3.4)$$

where  $\alpha_i$  is given in Table 3-1. Using the values  $\underline{r}_i^{(n)}$  we now make another time step by repeating the process.

| $\alpha_i$ | Order p  |          |          |
|------------|----------|----------|----------|
|            | <u>3</u> | <u>4</u> | <u>5</u> |
| $\alpha_0$ | 1/6      | 19/120   | 3/16     |
| $\alpha_1$ | 5/6      | 3/4      | 251/360  |
| $\alpha_2$ | 1        | 1        | 1        |
| $\alpha_3$ | 1/3      | 1/2      | 11/18    |
| $\alpha_4$ | ---      | 1/12     | 1/6      |
| $\alpha_5$ | ---      | ---      | 1/60     |

Table 3-1: Values of  $\alpha_i$  for Gear Predictor-Corrector  
Algorithm<sup>2</sup>

We found it useful in some phases of this work to extend the Gear algorithm to perform in a variable time-stepping mode, where the integrator varies the size of the time-step automatically. The idea behind variable stepsize integrating algorithms is to estimate the error E in making a timestep by comparing the results of two

integrators of orders  $q$  and  $q+1$ . If the estimated error  $E$  is larger than the maximum allowed error  $E_{\max}$ , we repeat the step at a smaller stepsize. If the error is less than the maximum allowed, we accept the step and change the stepsize based on the difference. Let  $\underline{r}_i^{[q]}(t+\Delta t)$  and  $\underline{r}_i^{[q+1]}(t+\Delta t)$  be the positions calculated using integrators of order  $q$  and  $q+1$ . The estimated error for the time step is given by

$$E = \max_{i,k} \left| r_{i,k}^{[q+1]}(t+\Delta t) - r_{i,k}^{[q]}(t+\Delta t) \right| \quad (3.5)$$

where  $r_{i,k}$  is the  $k^{\text{th}}$  component of  $\underline{r}_i$ . The new stepsize  $\Delta t_{\text{new}}$  is calculated from the old stepsize  $\Delta t_{\text{old}}$  by <sup>48</sup>

$$\Delta t_{\text{new}} = \begin{cases} 0.1 \Delta t_{\text{old}} & \gamma \leq 0.1 \\ \gamma \Delta t_{\text{old}} & 0.1 < \gamma < 2.0 \\ 2.0 \Delta t_{\text{old}} & 2.0 \leq \gamma \end{cases} \quad (3.6)$$

and

$$\gamma = 0.9 (E_{\max} / E)^{1/(q+1)}$$

The new stepsize  $\Delta t_{\text{new}}$  is used if the maximum error is exceeded and we have to repeat the step, or if we don't exceed the maximum and the step is accepted.

The usefulness of the variable stepsize method is limited in the applications in this work. The major drawback of the method is that two function evaluations are necessary, which automatically makes it almost twice as slow as the fixed stepsize method. The time step size using the variable step algorithm is fairly constant during thermodynamic property calculations, and certainly does not vary by a factor of two. The advantage of using a variable stepsize method is that one does not have to select a stepsize and hence the amount of work the user has to do and the chance of user error are decreased. We took advantage of this in some of the property calculations; the variable stepsize integrator was used for 25-100 steps, and the smallest stepsize necessary during that period was used for the remainder of the run in a fixed stepsize mode.

### 3.3 Boundary and Initial Conditions

The specification of a differential equation problem is incomplete without boundary and initial conditions. Equation (3.1) is a second order ordinary differential equation in time and requires  $2N$  initial conditions, where  $N$  is the number of atoms and  $d$  is the number of dimensions. Physically, these initial conditions are the initial positions and velocities of the atoms.

As pointed out in the Introduction to this Chapter,

it is essential to exclude "unlikely" configurations when taking property averages. A "likely" configuration is one in which the atoms are evenly distributed in the system volume and the velocities are distributed in a Boltzmann distribution. It is possible to set up a configuration such as this by assigning the atoms to lattice sites of a lattice type such as fcc, and assigning initial velocities randomly according to a Boltzmann distribution. At a nonzero temperature, however, one does not expect to find the atoms located at perfect fcc sites but slightly displaced from these positions. The practical solution to this problem is to note that as the simulation proceeds, one expects that the system will approach more likely configurations, and hence regardless of the initial configuration the system eventually approaches configurations which are suitable for property averages. This process is called "equilibration" and may take a few hundred time steps<sup>47</sup>. For some property calculations the atoms were set at fcc lattice sites and the velocities were assigned from a uniform distribution. The simulation was started, but property averages were not taken until a few hundred time steps had passed. In other calculations, the final configuration from previous simulations was used as the initial configuration.

So far no mention has been made about the assignment of the initial velocities of the system except to say that

they are selected from some type of distribution or from previous runs. An important characteristic of MD using the periodic boundaries discussed below is that linear momentum is conserved. The initial linear momentum introduced into the system is maintained throughout the simulation. If this momentum is nonzero, the total system will translate over time and the temperature will be calculated incorrectly since it will include the translational velocity. Hence, it is important to insure that the linear momentum of the system is zero.

The initial velocities of the system provide a way of setting the approximate temperature of the system. Although it is not possible before actually doing the calculations to know the final average temperature of an ensemble, it is possible to calculate and/or set the instantaneous temperature of a configuration. If  $T$  is the current configuration temperature and  $T_{des}$  is the desired temperature, one can set the instantaneous temperature to  $T_{des}$  by multiplying all of the atom velocities by  $(T_{des}/T)^{1/2}$ . This is called velocity-scaling<sup>47</sup>. In this work, velocity-scaling was used over a few hundred preliminary time steps, during which the system equilibrated and no property averages were calculated. The system was then allowed to rest for twenty or more steps, and then property calculations were started. The



final average temperature was usually within ten percent of the desired temperature.

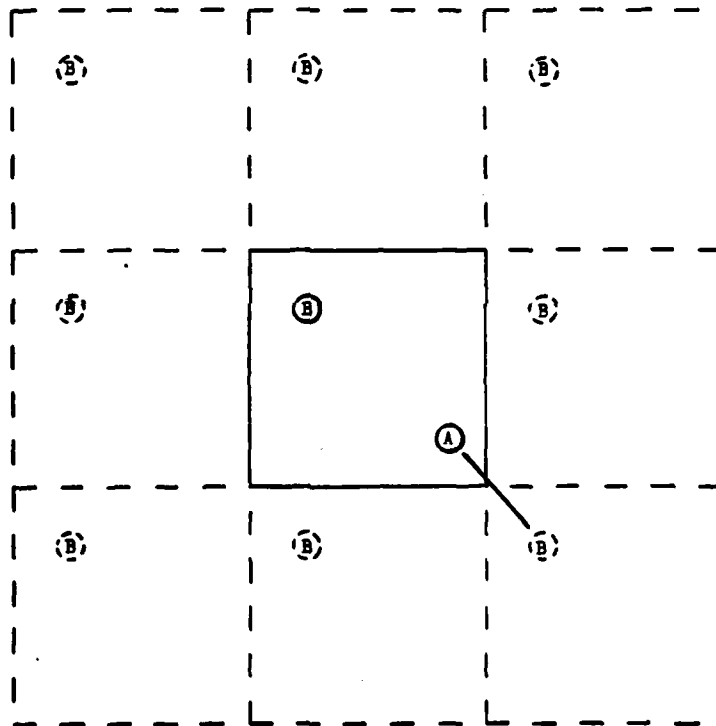
Since there are no spatial derivatives in (3.1) (recall that  $u(r_i)$  is a known function), it would seem that spatial boundaries should not be a problem. The problem arises, however, because we are trying to simulate a bulk material containing a large number of atoms, but are computationally limited to a few hundred atoms and simulation volumes with edge lengths of a few lattice constants. On a scale this size, where almost every atom can interact across the simulation boundary, the boundary conditions are very important. To overcome this difficulty, periodic boundaries in which the simulation volume is surrounded by images of itself as shown in Figure 3-1 are commonly employed<sup>47</sup>. In two dimensions, every atom has eight images. An atom interacts with the nearest image of another atom. This is shown in Figure 3-1 where atom A interacts with the image of B in the lower left volume.

### 3.4 Time-Saving Methods

It is possible to save considerable amounts of computer time by taking advantage of some time saving techniques. In this section we will discuss the techniques used in this code.

Figure 3-1: Periodic Boundaries

The simulation cell in the center is surrounded by images of itself. Atom A, only shown in the center cell, does not interact directly with atom B but with one of the images of B.



### 3.4.1 Verlet Neighbor List

As shown in Equation (3.1), it is necessary to calculate the force between each atom during every time step. In principle this requires  $N(N-1)/2$  evaluations of the potential function. As noted in Chapter 2, however, the potential function is normally truncated so that there are atoms in the simulation which do not directly interact with one another during some part of the run. The distance between the closest images of two atoms was greater than the cutoff distance for the potential, it is evident that the potential between the two atoms is trivial calculate since it is zero. At this point, however, computer time has already been wasted calculating the distance between two noninteracting atoms. Since we have  $N(N-1)/2$  interactions to calculate, this wastage can be considerable.

Of the suggested solutions to this problem, the standard Verlet list was used in this work<sup>49</sup>. The Verlet neighbor list is used to keep track of the atoms which have a nonzero interaction. One can think of the Verlet list as a  $N \times N$  truth matrix  $T_{ij}$ , where  $T_{ij} = 1$  or  $0$  if atoms  $i$  and  $j$  do or do not interact, respectively.  $T_{ij}$  is evaluated by actually calculating and checking the distances between all the atoms. For a subsequent given number of time steps, instead of calculating the distance

between atoms  $i$  and  $j$ , we just check to see if  $T_{ij}$  is 1 or 0, which is considerably quicker (and only calculate the distance if it is necessary to evaluate the potential). Since we are doing a dynamical calculation, it is evident that  $T_{ij}$  will eventually become out-of-date (in the worst case, after one time step). We overcome this difficulty by including atoms from slightly larger radii than the potential cutoff radius. Although we have a few extra atoms in the list, we still calculate fewer than  $N(N-1)/2$  radii and the list will remain up to date for a greater number of time steps. In this work, the cutoff range for the Verlet list was set at  $1.1r_c$ , where  $r_c$  is the cutoff radius for the potential, and the list was updated every ten potential evaluations. It is probably unnecessary to update the list this often since we were usually simulating solids, but it was found that the percentage of time spent updating the list at this frequency was relatively small.

The truth matrix  $T_{ij}$  is not usually implemented as a matrix on the computer for a number of reasons. Since  $T_{ij}$  is symmetric and the diagonal is all zeros, we actually only need to know the strictly upper triangle of  $T_{ij}$ . If the potential cutoff radius is much smaller than the simulation volume size, many elements  $T_{ij}$  are 0 and the matrix is sparse. Even though it is much quicker to test  $T_{ij}$  than calculate and test the distance between atoms  $i$  and  $j$ ,

we still have to test  $(N-1)(N-2)/2$  values. Finally, the number of elements in  $T_{ij}$  is proportional to  $N^2$ , so the matrix quickly gets large as  $N$  increases.

The standard way of implementing the neighbor list is illustrated schematically in Figure 3-2. The truth table  $T_{ij}$  is shown for a hypothetical system of  $N = 5$  atoms. As pointed out above, the upper triangle of  $T_{ij}$  is all we need to know. The idea behind the method is to keep track of only the 1's in  $T_{ij}$ . This is done with five vectors, one for each atom, where we note that the last vector is always null. The final step is to pack the vectors in a sequential list, where we keep track of the start of an atom's list using another vector.

### 3.4.2 Evaluation of the Potential

The potential function given by given by Lam<sup>1</sup> and discussed in Chapter 2 contain many transcendental functions which are time-consuming to calculate on a computer. Since most of the computer time in MD is usually spent calculating the potential for each atom-atom interaction for each time step, the potential in its analytic form is a serious practical problem. The common solution is to take the complicated potential and fit it to a functional form which is computationally easy to evaluate, such as polynomials, splines, or table-lookup.

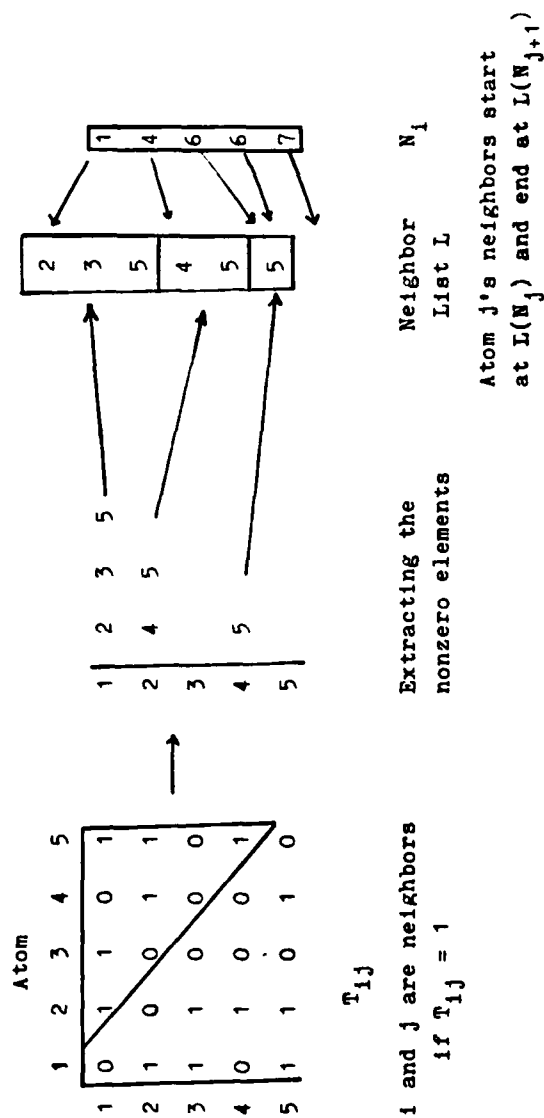


Figure 3-2: Implementation of Verlet Neighbor List

We used a spline fit which had maximum relative error of less than  $10^{-4}$  over the radii of interest.

In addition to using the spline fit to save time, we also used another computer-related method. During each time step in an MD simulation it is necessary to calculate the force between each atom. The general procedure is to calculate the radius  $r$  between the two atoms and then calculate the force for radius  $r$ . This requires calculating each component of  $r$  and then finding the Euclidean norm by taking the square root of the sum of the squares of the components. Depending on the computer used, the step that often takes the longest is taking the square root. If the potential function is particularly simple the calculation of  $r$  may take longer than calculating the force. For this reason it is possible to save a considerable amount of computer time if the evaluation of the square root can be avoided.

Let  $U(r)$  be a potential function, where  $r$  is the radius between two particles. During an MD run we need to calculate

$$F_k^{ij} = - \left. \frac{dU}{dr} \right|_{r=r_{ij}} \times \frac{r_k^{ij}}{r_{ij}} \quad (3.7)$$

where  $r_k^{ij}$  is the  $k$ th component of  $\underline{r}_i - \underline{r}_j$ . Also define another potential  $W(s)$

$$W(s) = U(r) \quad (3.8)$$

where  $s = r^2$ . It is readily shown

$$\frac{dW(s)}{ds} = \frac{1}{2r} \times \frac{dU(r)}{dr} \quad (3.9)$$

and

$$F_k(r_{ij}) = -2 \frac{dW(s)}{ds} r_{ij} \quad (3.10)$$

In most simulations involving thermodynamic property calculations the virial term must be evaluated to calculate the pressure. This can be expressed

$$r \frac{dU(r)}{dr} = 2s \frac{dW(s)}{ds}$$

Hence, if the potential function can be expressed as a function of  $s = r^2$ , we can calculate the energy, force components, and virial term without taking a square root. In this work this involved fitting the potential to  $s$  instead of  $r$ . The run times on the Compupro 8086 system were reduced by approximately forty percent. We also note that the commonly used Lennard-Jones 6-12 potential is easily expressed as a function of  $r^2$ , although the shifted force method in its common form cannot since that puts an  $r^{47}$  term in the potential. It is possible to shift the force using an  $r^2$  term, however, which probably has as much physical significance as the standard way.



### 3.5 Thermodynamic Property Calculations

Three basic thermodynamic properties are normally calculated in MD simulations: the total energy  $E$ , the temperature  $T$ , and the pressure  $P$ . In the microcanonical simulations performed using conventional molecular dynamics, the simulation volume is fixed and hence the mass density is predetermined. Since the total energy should be constant, it is also a useful measure of the correctness of the computer code. In this section we will outline how  $E$ ,  $T$ , and  $P$  are calculated using molecular dynamics following Haile<sup>47</sup>. Other properties which are also calculated simultaneously with the thermodynamics properties, the radial distribution function, order parameter, and the mean-square displacement, will also be discussed in this Section.

The total energy  $E$  is the sum of the kinetic energy K.E. and potential energy P.E. of the system,

$$E = \text{K.E.} + \text{P.E.} \quad (3.11)$$

The instantaneous kinetic energy is given by

$$\text{K.E.}(t) = \frac{3m}{2} \sum_i v_i^2(t), \quad (3.12)$$

i.e., the sum of the kinetic energies of each atom. The instantaneous potential energy is the sum of the interactions between each atom,

$$P.E.(t) = \sum_{j<i} u(r_{ij}) \quad (3.13)$$

Since we are solving Newton's equations of motion, we expect the total energy  $E$  to be constant, but because of numerical errors,  $E$  varies by about  $10^{-4}$ .

The instantaneous temperature  $T$  can be extracted from the kinetic energy since

$$\frac{3}{2} NkT = K.E. \quad (3.14)$$

and solving for  $T$

$$T = \frac{2}{3Nk} K.E. \quad (3.15)$$

The simulation pressure  $P$  is more difficult to calculate than  $U$  and  $T$ . The instantaneous pressure  $P$  is given by

$$P = \frac{NkT}{V} - \frac{1}{3V} \sum_{i<j} r_{ij} \frac{du(r_{ij})}{dr_{ij}} \quad (3.16)$$

where  $T$  and  $V$  are instantaneous temperature and volume. The virial sum, which is the second term on the right hand side, can be calculated concurrently with the right hand side of (3.1) since  $du/dr$  must be calculated anyway. Given the system pressure, we can now calculate the enthalpy  $H$  from

$$H = E + PV \quad (3.17)$$

where  $V$  is the system volume.

The radial distribution function  $g(r)$  is an unnormalized probability density function for finding an atom at a radius  $r$  from another atom. It can be calculated using

$$g(r) = \frac{\langle N(r \pm \Delta r/2) \rangle}{V(r \pm \Delta r/2)\rho} \quad (3.18)$$

where  $\langle N(r \pm \Delta r/2) \rangle$  is the time average number of atoms between  $r - \Delta r/2$  and  $r + \Delta r/2$ ,  $V(r \pm \Delta r/2)$  is the volume of the spherical shell between these two radii, and  $\rho$  is the number density.

The mean-square displacement  $MSD(t)$  is the square of the average displacement of all the atoms in the system at time  $t$ . For a system containing  $N$  atoms, it is given by

$$MSD(t) = \frac{1}{N} \sum_i [\underline{r}_i(t) - \underline{r}_i(0)]^2 \quad (3.19)$$

where  $\underline{r}_i(t)$  is the position of atom  $i$  at time  $t$ .

The order parameter is a measure of the order of the system. The short range order parameter used in this work is given by

$$\rho = \sum_{i,j}' \exp(i\mathbf{K} \cdot \underline{r}_{ij}) \quad (3.20)$$

where  $\underline{K}$  is a reciprocal lattice vector and  $\underline{r}_{ij}$  is the vector between atoms  $i$  and  $j$ . In this work three values of  $\underline{K}$  were used:

$$\underline{K}_1 = \frac{4\pi}{a} [1,0,0] \quad (3.21)$$

$$\underline{K}_2 = \frac{4\pi}{a} [0,1,0] \quad (3.22)$$

$$\underline{K}_3 = \frac{4\pi}{a} [0,0,1] \quad (3.23)$$

The order parameter results given in Chapter 5 are the averages of the individual order parameters calculated with these three reciprocal-lattice vectors.

All the these quantities (except for the total energy) fluctuate during the simulation and averages must be calculated. For a simulation of  $M$  time steps, the average of a property  $A(t)$  is

$$\langle A \rangle = \frac{1}{M} \sum_{m=1}^M A(t_m)$$

### 3.6 The Parrinello-Rahman Method

One of the disadvantages of using conventional molecular dynamics is the that the constants of motion are the number of atoms  $N$ , the volume  $V$  and the total energy  $E$ , which is called a microcanonical ensemble. The initial conditions (atom positions and velocities) and the system volume specify  $N$ ,  $V$  and  $E$  at the beginning of the

simulation and these values do not fluctuate. The temperature and pressure, however, fluctuate with time which requires us to calculate a few thousand time steps to accurately calculate their average values. Consequently, we don't know the temperature and pressure of the system until after the run is finished. Unfortunately, experimental data for solids is usually given for a single pressure (i.e., atmospheric pressure), which makes it difficult to compare MD results with experimental results. A way to overcome this difficulty was proposed by Andersen<sup>27</sup>, in which one could apply a pressure to the system and the volume would fluctuate. This was generalized by Parrinello and Rahman, who developed a method to apply a general stress to the system by allowing the shape to change<sup>28, 51</sup>. Parrinello and Rahman's method was implemented in this work to allow us to calculate thermodynamic properties at a given pressure.

Let the system volume be a parallelepiped, as shown in Figure 3-3, whose edges are the three vectors  $\underline{a}$ ,  $\underline{b}$ ,  $\underline{c}$ . Let  $\underline{r}_i$  be the position of atom  $i$  in the volume. We can now define a vector  $\underline{s}_i$  such that

$$\underline{r}_i = \underline{h} \underline{s}_i \quad (3.24)$$

where  $\underline{h}$  is a 3x3 matrix  $\underline{h} = \{\underline{a}, \underline{b}, \underline{c}\}$ . Since each atom is confined to the volume,  $0 \leq s_i^k \leq 1$ , where  $s_i^k$  is the  $k$ th component of  $\underline{s}_i$ . We now observe that we can easily change

the volume and shape of the system by changing  $\underline{h}$ . The key to the flexible boundary method is define equations of motion for  $\underline{h}$  (and alter the equations of motions of the atoms) such that we can apply a given hydrostatic pressure to the system. If  $u(r)$  is a pairwise interatomic potential, these equations are given by

$$\ddot{\underline{s}}_i = -m_i^{-1} \sum_{j \neq i} (u'/r_{ij}) (\underline{s}_i - \underline{s}_j) - \underline{G}^{-1} \underline{G} \dot{\underline{s}}_i, \quad i, j = 1, 2, \dots, N \quad (3.25)$$

$$\ddot{\underline{h}} = W^{-1} (\underline{\Omega} - p_{\text{ext}}) \underline{\sigma} \quad (3.26)$$

where

$$\underline{\sigma} = (\underline{h}^T)^{-1} \quad (3.27)$$

$$\underline{G} = \underline{h}^T \underline{h} \quad (3.28)$$

$$\underline{\Omega} = || \underline{h} || \quad (3.29)$$

$$\underline{\Omega} \underline{\Omega} = \sum_i m_i \underline{v}_i \underline{v}_i^T - \sum_{j>i} (u'/r_{ij}) \underline{r}_{ij} \underline{r}_{ij}^T \quad (3.30)$$

and  $m_i$  is the mass of the  $i^{\text{th}}$  atom.  $W$  is physically equivalent to a wall mass and provides inertia for the boundaries of the simulation volume. Equations (3.25) and (3.26) are valid when a hydrostatic pressure is applied to the system, but they can be generalized for an arbitrary external stress<sup>51</sup> which is not necessary in this work.

We now make some observations about the trajectories generated by solving (3.25) and (3.26). The Hamiltonian corresponding to equations (3.25) and (3.26) is

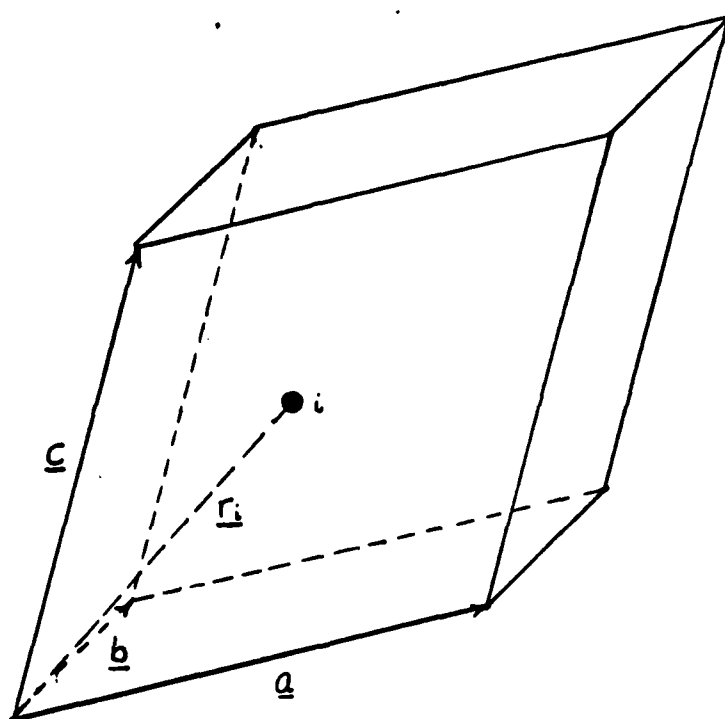
$$\mathcal{H} = \frac{1}{2} \sum_i m_i \underline{\dot{v}}_i^2 + \sum_{j>i} u(r_{ij}) + \frac{1}{2} W \text{Tr} \underline{\dot{h}}^T \underline{\dot{h}} + p\Omega \quad (3.31)$$

where  $p$  is the applied hydrostatic pressure. The first two terms comprise the Hamiltonian for conventional molecular dynamics, i.e., a microcanonical ensemble, in which the total energy  $E$  is constant. The fourth term is the pressure work contribution to the enthalpy. Except for third term, the constant of motion is then the enthalpy

$$H = E + p\Omega \quad (3.32)$$

The third term of (3.31) is the kinetic energy of the boundary. Its magnitude can be estimated by noting that it contains nine degrees of freedom (one for each element

Figure 3-3: Simulation Volume of a  
Flexible Boundary System





of  $\underline{h}$ ), and the average amount of energy in the boundary will be  $9/2kT$ , where  $k$  is Boltzmann's constant. On the other hand, the first term of (3.31) is the kinetic energy of the atoms and on average is  $3N/2kT$ , where  $N$  is the number of atoms. Ignoring the third term results in an error of  $3:N$ , and consequently the enthalpy  $H$  is the constant of motion within this error.

One ambiguity in using the Parrinello-Rahman flexible boundary method is the selection of the wall mass  $W$ . For calculation of equilibrium averages, the selection of the value of  $W$  is immaterial since the averages are independent of the masses, as long as the property averages are accumulated over a few oscillations of the walls. In this work, we followed Andersen<sup>27</sup> and Parrinello<sup>51</sup> and Rahman and used  $W = 20m$ . Recently, De Leeuw et al<sup>34</sup> used a wall mass of  $W = m$  so that the energy transfer between the walls and atoms was optimized. They also tested other values of  $W$  and found that their static results were independent of the selection.

Chapter 4  
Molecular Statics

4.1 Introduction

Molecular statics (MS) is a method of obtaining stable and metastable configurations of static systems. A stable configuration is the lowest energy configuration of the system. A configuration is metastable when it is at a local energy minimum such that small perturbations of the configuration will return to the metastable configuration. If a metastable or stable configuration is used as an initial configuration for a molecular dynamics (MD) run, the atoms would never move provided they have no initial velocities, i.e., the initial temperature of the system is zero. One can therefore consider MS as a way of calculating the properties of a system at a temperature of absolute zero. The two methods differ in the desired goal, however. The centerpiece of molecular dynamics is the faithful solution of Newton's equations of motion. In molecular statics, one is interested in determining stable and metastable configurations at  $T = 0K$ ; the main concern is getting to those configurations as quickly as possible and insuring the configuration is indeed stable or metastable.

Since the earliest computational defect studies by Tewardt et al<sup>20</sup> and Girifalco et al<sup>18</sup>, MS has been the preferred method compared to MD for calculating defect formation, migration, and binding energies. There are two reasons for this. The first is that MS is computationally much faster than MD. In MS one is interested in a single configuration -- the lowest energy configuration for a given system. Once this configuration is reached, usually after no more than a few hundred "time" steps, the computer run is finished. On the other hand, using MD one is simulating a material at a given temperature and one must wait for events to happen. For example, if a vacancy jumps once a picosecond on the average, one must calculate a thousand time steps between each jump using a time step size of 0.001 picoseconds. To accumulate good statistics for calculating the average jump time and other properties, a hundred and preferably more jumps are necessary which will require at least a hundred thousand time steps. In this example, MS is three orders of magnitude faster than MD. It also should be pointed out that the calculation of defect energies using MD requires results at different temperatures, so at least two such long runs must be made. The second reason MS is preferred over MD is that data analysis is considerably easier. The result of an MS calculation is a single configuration of atoms in which the atoms are motionless. This final

configuration can be analyzed on-line, i.e., just after the run, and/or saved for future reference. In MD, however, one has generated thousands of configurations during a run. To make matters worse, the atoms are moving and are almost certainly displaced from their average positions. This makes it difficult to even locate the defect, especially at high temperatures.

Regardless of the advantages of MS over MD for the purpose of calculating defect energies, it must be pointed out that MS results are strictly valid only at  $T = 0K$ . Some defect properties (see, for example, grain-boundary melting transition work of Ciccotti et al<sup>50</sup>) cannot be simulated using MS. For those properties which can be calculated using MS, however, one can argue that the temperature dependence of the property is overshadowed by the uncertainty in the interatomic potential. If the given interatomic potential will only reproduce the migration energy of a vacancy within ten percent of the experimental value, it could be pointless to attempt MD calculations since the variation of the migration energy with temperature may be less than this. The only extensive comparison of MD and MS defect calculation was done by Guinan et al<sup>52</sup>. Guinan et al<sup>52</sup> calculated the migration energy of interstitials in tungsten using both MD and MS, and found the results agreed within the uncertainties of the methods.

Since MS and MD are closely related, much of the discussion in the previous Chapter will apply to MS, especially techniques for speeding up the calculation of the potential function between atom pairs discussed in Section 3.4. In this Chapter the methods for getting the metastable and stable configurations which will be discussed since these are peculiar to molecular statics. The following section will cover previously used methods; after that a new method which is computationally orders of magnitude faster than previous methods will be presented and all the methods will be compared using some simple test cases. Since MS is used exclusively in this work to calculate defect formation, binding, and migration energies, the techniques necessary to calculate these quantities will be discussed in Section 4.

#### 4.2 Review of Molecular Statics Methods

Different computational methods can be used to determine the minimum energy configuration of a system of atoms. Before discussing these methods, however, it is useful to first point out the characteristics of the minimization problem itself. The primary characteristic is that the energy depends on a large number of variables, in fact  $3N$  variables where  $N$  is the number of atoms in the system and the variables are the atom coordinates. Another characteristic is that we can normally expect that

the gradient vector, which is the first derivatives of the the energy with respect to the variables, is available since the derivatives are used to calculate the interatomic forces. On the other hand, the second derivatives of the energy with respect to the variables, mathematically called the hessian matrix and proportional to the force constant matrix, is not so easy to calculate. The hessian matrix is not required for MD calculations as discussed in the previous Chapter. Finally, we note the system variables are not bound by any mathematical constraints. Although the periodic boundaries discussed in Section 3.3 appear to constrain the atoms to the simulation cell, physically an atom can leave the cell because one of its images will enter from the opposite boundary. A constraint in the mathematical sense is physically equivalent to the wall of an infinite well, and the periodic boundaries allow us to avoid using this type of boundary.

Historically, molecular statics methods have been divided into two categories. The first are methods in which Newton's equations of motion are solved for the system of atoms, modified such that energy is removed from the system as it approaches the minimum energy state. These methods can be implemented by converting a standard molecular dynamics code since the code already solves the equations of motion and will be called "quasidynamic"

methods. The other category whose methods completely dispense with solving Newton's equations and use general mathematical minimization techniques to minimize the<sup>53</sup> energy. These are often called "variational" methods. These methods converge more quickly to the minimum energy, although some believe that the first category of techniques will converge more reliably to the global<sup>53</sup> energy minimum and not to some local minimum. Mathematically, however, there is no evidence that methods in the first category are more reliable than those in the second, and this author believes that in general one should use the fastest method available.

There are two MS quasidynamic methods which are still commonly used. (These methods not universally considered MS methods, but are nevertheless included here since they are used for the same purposes as the methods discussed below.) The principle behind the first method is to apply a frictional or braking force to the atoms which is proportional to their velocities<sup>33</sup>. This will be called the "frictional" method in this work. The justification for this method comes from the fact that the total energy, the sum of the kinetic and potential energies, for the system is constant. When the potential energy of the system is lowest, the kinetic energy and hence the atom velocities are highest and the braking force slows the system down near this configuration. The second

quasidynamic method involves setting the velocity of an atom to zero whenever the dot product of the velocity and acceleration of an atom is negative<sup>54</sup>. This will be called the "v.a" method here. This technique prevents an atom from climbing out of a local energy well. The main advantage of these methods is that they can be implemented by making relatively trivial modifications to an existing MD computer code.

Two mathematical methods which used to minimize a function of many variables are the steepest-descent and conjugate-gradient methods. These methods, like the quasidynamic methods discussed above, only require the gradient vector to be calculated. When one has a working MD computer code, the main disadvantage of the steepest-descent and conjugate gradient methods is that one must make more extensive modifications to an existing MD code to implement them.

Probably the fastest minimization schemes for unconstrained problems are Newton-like methods<sup>55</sup>. (Note: Newton-like mathematical minimization methods are not related to Newton's equations motion.) These techniques use calculated or approximated first and second derivatives, i.e. the gradient and the hessian, to perform the minimization. Let  $r_m$  be the atom positions at the end of the  $m$  iteration, and  $g_m$  and  $[Q_m]$  be the corresponding gradient and hessian matrix. The next iteration  $r_{m+1}$  is then given by



$$r_{m+1} = r_m - [Q]_m^{-1} g_m \quad (4.1)$$

The Newton method has recently be used by Wolf in grain boundary statics calculations<sup>56</sup>. Wolf found that only a few iterations were required to minimize grain boundary configuration which would required hundreds of iterations using gradient methods<sup>56</sup>.

There are some important drawbacks to this Newton's method, however. The first is a drawback to the programmer: it is necessary to calculate to hessian matrix [Q]. This is not a trivial task, but if it only has to be programmed once and a great improvement in computer efficiency can be achieved, then it is probably warranted. The second drawback is the requirements on computer memory. [Q] is a 3Nx3N symmetric matrix. Assuming four bytes per real number and N=500, 4.5 Megabytes of computer memory are required if one takes advantage of symmetry. This amount of memory was not available for this work, but most modern computers (including microcomputers) can be so equipped and this alone does not make the method intractable. The third drawback is the most important. In molecular dynamics and many molecular statics methods, most of the computer time is spent evaluating the interatomics forces, i.e., the function evaluation. In these situations the number of function evaluations required is a good comparison point since it is

approximately proportional to the total computer time. This is not true when using Newton's method on large systems, however, because the method introduces overhead which is comparable to the time required to evaluate the forces. Part of the overhead stems from the calculation of the hessian matrix  $[Q]$ . The interaction of two atoms generates a 3-component force vector and a  $3 \times 3$  matrix of second derivatives. If the evaluation of the potential has been optimized, the additional time required to construct the hessian is significant (recall that it is also necessary to calculate the second derivative of the potential). The other source of the overhead is the solution of the set of linear equations for  $r_{m+1}$  ( $[Q]$  is not actually inverted). The time required to solve these equations is proportional to  $N^3$  and hence is important for large  $N$ .<sup>57</sup>

#### 4.3 A New Method

A special implementation of a method due to Fletcher and Powell<sup>58</sup> allows us to avoid the drawbacks of Newton's method. What is avoided in this implementation is: 1) storage of a  $3N \times 3N$  matrix, 2) direct calculation of the hessian, and 3) solution of a set of  $3N$  linear equations. We retain, however, the excellent convergence properties of Newton-like methods. The standard implementation of Fletcher's method is shown in the algorithm in Figure 4-1.

The key to the method is the calculation of a matrix  $H_{m+1}$  which converges to  $[Q]^{-1}$ , the inverse of the hessian. Instead of calculating  $[Q]$  directly and solving a set of equations for  $r_{m+1}$ , we update  $H_m$  and do a matrix multiplication.

The algorithm in Figure 4-1 overcomes two of the three drawbacks of the Newton method because the hessian does not have to be directly calculated and a system  $3N$  linear equations does not have to be solved. Unfortunately, we still have to store a  $3N \times 3N/2$  matrix which was beyond the capabilities of the computers used for this work. The solution to this problem is found by noting that although  $A_m$  and  $B_m$  are  $3N \times 3N$  matrices, all of the information they contain is also contained in the  $3N$ -vectors  $d_m$  and  $z_m$  and two scalars  $a_m$  and  $b_m$  such that

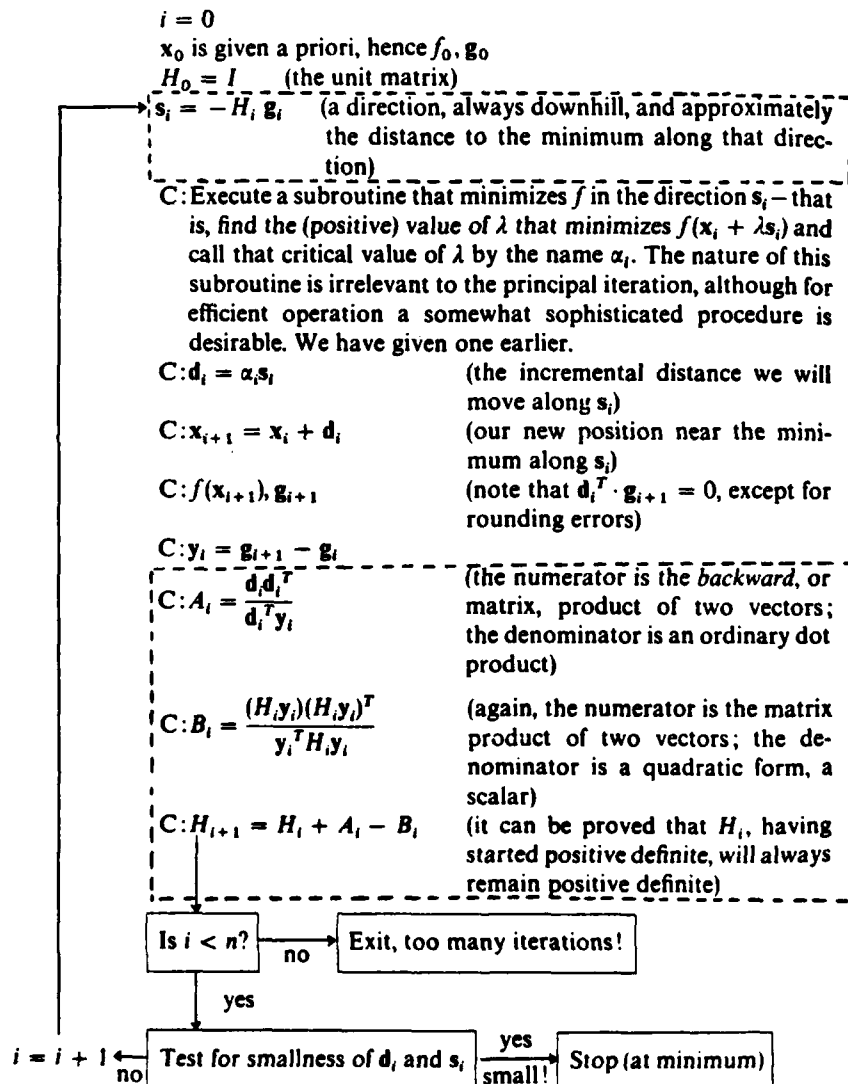
$$A_m = \frac{\begin{matrix} & & T \\ & d & d \\ & m & m \end{matrix}}{a_m} \quad (4.2)$$

$$B_m = \frac{\begin{matrix} & & T \\ & z & z \\ & m & m \end{matrix}}{b_m} \quad (4.3)$$

where

**Figure 4-1: Conventional Algorithm for Fletcher's Method**

The portions of the algorithm which are replaced in the modified algorithm in Figure 4-2 are enclosed in the hashed rectangles (from 59 Acton )



$$z_m = H_m y_m \quad (4.4)$$

$$a_m = d_m^T y_i \quad (4.5)$$

$$b_m = y_m^T H_m y_m \quad (4.6)$$

We can rewrite  $H_m$  as

$$H_m = I + \sum_{j=0}^{m-1} (A_j - B_j) \quad (4.7)$$

Two key observations can be made at this point. The first is that we do not have to store  $H$  directly, but instead we can store the sequence of vectors and scalars  $d_m$ ,  $z_m$ ,  $a_m$ , and  $b_m$ , since they contain all of the information in  $A_m$  and  $B_m$ . As long as  $m < 3N/4$ , we will be using less storage than the conventional implementation. It would appear that the price of the reduced memory requirement is a sacrifice in efficiency since to multiply the  $3N \times 3N$  matrix  $H_m$  times a vector, we have to actually multiply the vector by  $2m$   $3N \times 3N$  matrices. This leads to the second observation, where we rewrite the multiplication of the vector  $w$  by  $A_m$  as

$$A_m w = \frac{d_m^T d_m}{a_m} w \quad (4.8)$$

$$= \{d_m \{ \{d_m^T w\} / a_m \} \} \quad (4.9)$$

where the braces indicate the order of evaluation. Noting that  $d_m^T w$  is a scalar, we have reduced the matrix multiplication of  $w$  by a  $3N \times 3N$  matrix to the evaluation of the dot product of two  $3N$  vectors and the multiplication of a  $3N$  vector by a scalar. The net result is that this implementation is actually faster than the conventional method for  $m < 3N/2$ , which is definitely the case for the molecular statics problems in this work.

In Figure 4-2 the revised algorithm is presented. It was found that this method converged in about ten to a hundred iterations, such that  $m \ll 3N/4$  for realistic  $N$ .

#### 4.4 Comparisons of Methods

Some of the MS methods discussed in the previous sections were implemented to compare their ability to determine static configurations. The frictional and v.a methods were implemented since many workers are familiar with them. The steepest-descent method was also

**Figure 4-2: Modified Algorithm for Fletcher's Method**

$i = 0$   
 $\mathbf{x}_0$  is given a priori, hence  $f_0, \mathbf{g}_0$   
 $H_0 = I$  (the unit matrix)

$$\mathbf{s}_i = - \left[ \mathbf{g}_i + \sum_{j=0}^{i-1} \frac{\mathbf{d}_j^T \mathbf{g}_i}{\mathbf{d}_j^T \mathbf{d}_j} \mathbf{d}_j - \sum_{j=0}^{i-1} \frac{\mathbf{z}_j^T \mathbf{g}_i}{\mathbf{z}_j^T \mathbf{z}_j} \mathbf{z}_j \right]$$

C: Execute a subroutine that minimizes  $f$  in the direction  $\mathbf{s}_i$ —that is, find the (positive) value of  $\lambda$  that minimizes  $f(\mathbf{x}_i + \lambda \mathbf{s}_i)$  and call that critical value of  $\lambda$  by the name  $\alpha_i$ . The nature of this subroutine is irrelevant to the principal iteration, although for efficient operation a somewhat sophisticated procedure is desirable. We have given one earlier.

C:  $\mathbf{d}_i = \alpha_i \mathbf{s}_i$  (the incremental distance we will move along  $\mathbf{s}_i$ )

C:  $\mathbf{x}_{i+1} = \mathbf{x}_i + \mathbf{d}_i$  (our new position near the minimum along  $\mathbf{s}_i$ )

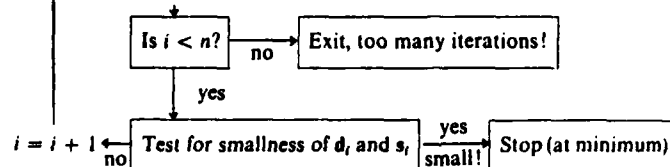
C:  $f(\mathbf{x}_{i+1}), \mathbf{g}_{i+1}$  (note that  $\mathbf{d}_i^T \cdot \mathbf{g}_{i+1} = 0$ , except for rounding errors)

C:  $\mathbf{y}_i = \mathbf{g}_{i+1} - \mathbf{g}_i$

$$\mathbf{z}_i = \mathbf{y}_i + \sum_{j=0}^{i-1} \frac{\mathbf{d}_j^T \mathbf{y}_i}{\mathbf{d}_j^T \mathbf{d}_j} \mathbf{d}_j - \sum_{j=0}^{i-1} \frac{\mathbf{z}_j^T \mathbf{y}_i}{\mathbf{z}_j^T \mathbf{z}_j} \mathbf{z}_j$$

$$\mathbf{a}_i = \mathbf{d}_i^T \mathbf{y}_i$$

$$\mathbf{b}_i = \mathbf{y}_i^T \mathbf{z}_i$$



implemented; the conjugate gradient method did not appear to converge significantly faster in some tests, although those results are not given here. Because of memory limitations, Newton's method could not be implemented for this test. Finally, the Fletcher-Powell method as discussed in the previous section was implemented.

Three test cases were selected to compare the methods. Case I is the minimization of a single vacancy system. A single atom was removed from a 108 atom fcc cube, and this was used as the initial configuration. In Case II the methods were used to minimize a system containing an 19-vacancy platelet. The initial configuration was created by removing 19 atoms forming a hexagon from a (111) plane of a 108 atom fcc cube. Since more atoms are removed in the Case II than Case I, one expects that more atoms will be displaced and the displacements will be larger. Case III is a defect migration calculation for a single vacancy. In this Case the system is constrained above the minimum energy configuration which makes minimization more difficult than in Cases I and II (this method is discussed in more detail in the following section). The impetus to find a faster MS technique was because the migration calculations took so long using existing methods.

The results of the comparisons are shown in Figures 4-3, 4-4 and 4-5. It is evident that the both the



steepest descent and Fletcher-Powell methods are considerably faster than the frictional and v.a techniques in Figure 4-3 and 4-4. The steepest-descent method is only about a factor of two slower in these two Cases. In the migration calculation in Case III, it is apparent the Fletcher-Powell method is far and away the best technique. It converges an order of magnitude faster than the steepest-descent method, and within 500 steps the frictional and v.a methods have converged to about four significant figures.

#### 4.5 Defect Energy Calculations

##### 4.5.1 Formation Energy

The defect quantities calculated in this work are the formation, migration, and binding energies of defect clusters. In this section we discuss the use of molecular statics to calculate these defect properties. The calculation of the formation and binding energy of a defect requires the use of molecular statics in a straightforward manner to determine the metastable configurations and energies of a defect, and then the proper manipulation of the energies to get the formation and binding energies. To calculate the migration energy, however, one must make some minor modifications to a standard molecular statics code.

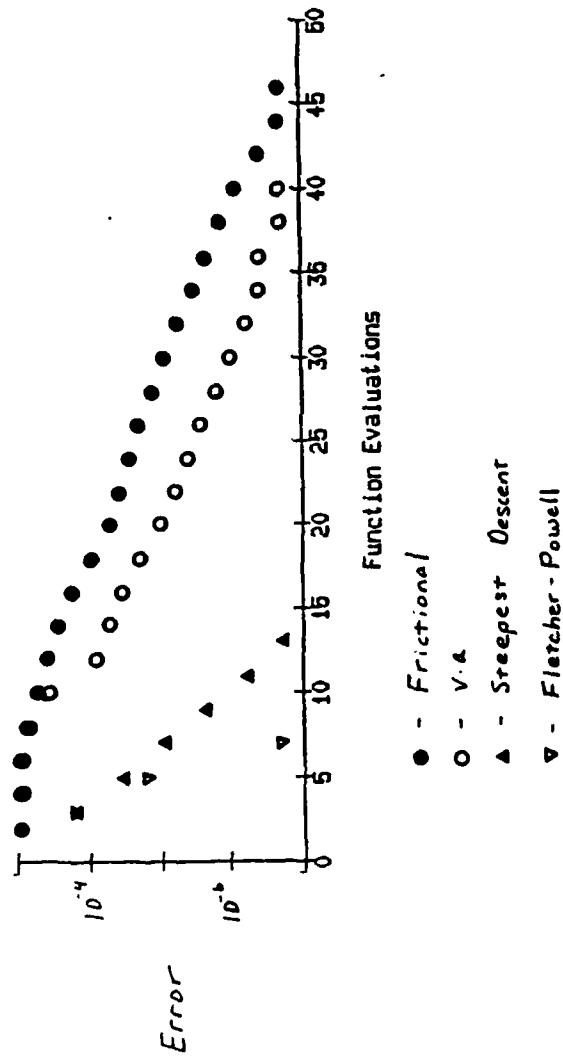


Figure 4-3: Comparison of MS Methods for Case 1

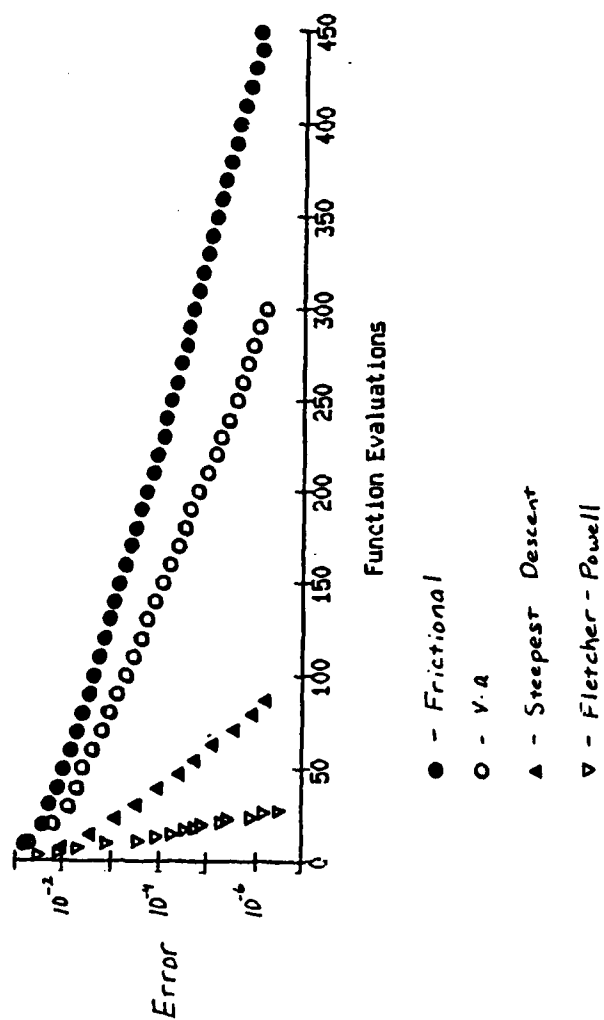


Figure 4-4: Comparison of MS Methods for Case 2

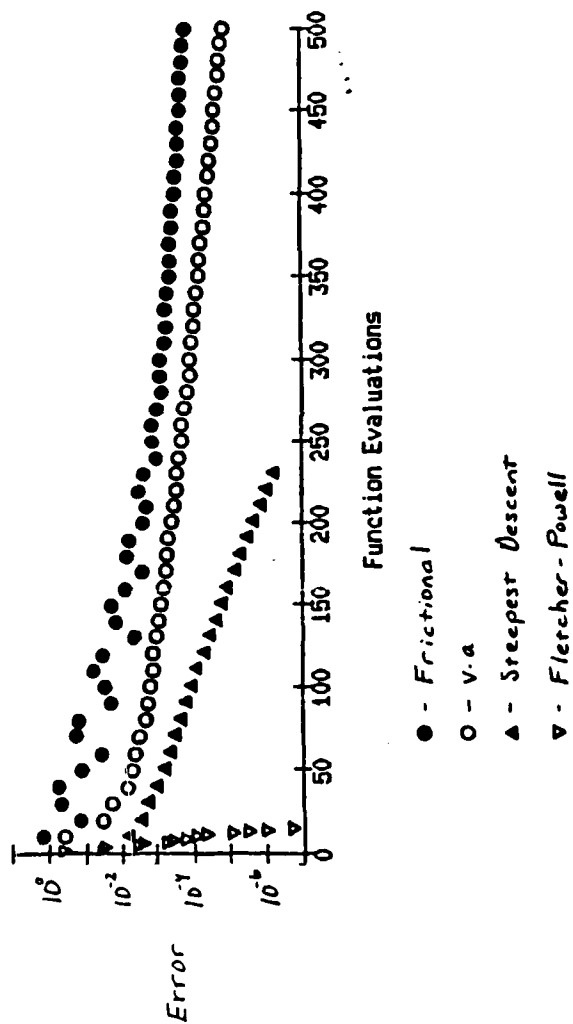


Figure 4-5: Comparison of MS Methods for Case 3

The formation energy of a defect is the difference in energy between a system S containing the defect and an otherwise identical system S\* which does not. The formation energy of almost any defect can be defined for a system S\*, such as an interstitial, vacancy, defect cluster, etc. S\* is normally selected to be the ideal or perfect lattice, and the formation energy is the energy required to introduce a defect into a perfect lattice. Generally speaking, S\* does not have to be a perfect lattice; for example, S\* can be a system containing a grain boundary and the "defect" could be a vacancy. In this instance the formation energy is the energy required to introduce a vacancy near a grain-boundary. In the context of this work, S\* will always be the perfect lattice and the defects will be vacancies and vacancy clusters.

To calculate the formation energy of a vacancy using molecular statics, it is necessary to calculate the enthalpies of both a system S containing a vacancy and the corresponding perfect lattice system S\*. S and S\* should both contain the same number of atoms N'. Let H and H\* be the enthalpies of S and S\*. The formation energy is then

$$E_{vl}^f = H - H^* \quad (4.10)$$

Unfortunately, it is not possible to calculate H\* directly

using molecular statics. To simulate a perfect FCC lattice, the number of atoms  $N = 4ijk$ , where  $i$ ,  $j$ , and  $k$  are positive integers, and to simulate a lattice with a vacancy,  $N' = 4ijk - 1$ . In defect simulations one normally uses  $i=j=k$ , which further limits the choice of  $N$  and  $N'$ . The result is that we cannot directly simulate both  $S$  and  $S^*$  because there are not corresponding values of  $N$  and  $N'$ . The solution to this difficulty is to take advantage of the equivalence of each atom in the perfect lattice. Assuming the atoms are indistinguishable, the neighborhood of each atom, i.e., the number and positions of surrounding atoms, is identical. For this reason the total enthalpy of a perfect lattice is proportional to the number of atoms in the system  $N$ . If  $H_0$  is the enthalpy of a perfect lattice containing  $N$  atoms, and  $H^*$  is the enthalpy of a perfect lattice with  $N'$  atoms, then

$$H^* = \frac{N'}{N} H_0 \quad (4.11)$$

and

$$\frac{f}{E_{vl}} = H - \frac{N'}{N} H_0 \quad (4.12)$$

In practice, the perfect lattice system  $S_0$  consists of  $N$  atoms and the system  $S$  containing the vacancy contains  $N' = N-1$  atoms.  $N$  will be selected such that  $N = 4ijk$ . Thus,

$$\frac{E_f}{N} = H - \frac{N-1}{N} H_0 \quad (4.13)$$

$S$  is the system  $S_0$  with a single atom removed, but both systems have the same volume.

It is possible to rewrite (4.13) in a form more amenable for molecular statics calculations. Let  $U$ ,  $P$ , and  $V$  be the internal energy, pressure, and volume of  $S$ , and  $U_0$ ,  $P_0$ , and  $V_0$  be the corresponding values for  $S_0$ . Then  $H_0 = U_0 + P_0 V_0$  and  $H = U + P V$ . Assuming  $P = P_0$ , we get

$$\begin{aligned} \frac{E_f}{N} &= U - \frac{N-1}{N} U_0 + P_0 \left[ V - \frac{N-1}{N} V_0 \right] \\ &= U - \frac{N-1}{N} U_0 + \langle \text{Virial} \rangle \end{aligned} \quad (4.14)$$

where

$$\langle \text{Virial} \rangle = P_0 \left[ V - \frac{N-1}{N} V_0 \right] \quad (4.15)$$

As noted above,  $V = V_0$ . The pressure is calculated from

$$P_0 = \frac{1}{6V_0} \sum_i \sum_{j \neq i} r_{ij} \frac{du(r_{ij})}{dr}, \quad 1 \leq i \leq N \quad (4.16)$$

Substituting into (4.15),

$$\langle \text{Virial} \rangle = \frac{1}{6N} \sum_i \sum_{j \neq i} r_{ij} \frac{du(r_{ij})}{dr}, \quad 1 \leq i \leq N \quad (4.17)$$

As noted above, every atom in the perfect lattice is equivalent. This allows us to rewrite the sum over  $i$  as

$$\sum_i \sum_{j \neq i} r_{ij} \frac{du(r_{ij})}{dr} = N \sum_{j \neq 1} r_{1j} \frac{du(r_{1j})}{dr}, \quad 1 \leq i \leq N \quad (4.18)$$

where we have arbitrarily chosen  $i = 1$  on the right hand side. The virial term then becomes

$$\langle \text{virial} \rangle = \frac{1}{6} \sum_{j \neq 1} r_{1j} \frac{du(r_{1j})}{dr} \quad (4.19)$$

The quantity  $\langle \text{virial} \rangle$  is thus the virial contribution of a single atom in the perfect lattice. For any given lattice constant and potential cutoff radius we only have to calculate  $\langle \text{virial} \rangle$  once since it is independent of  $N$ .

Equation (4.14) can be generalized to calculate the formation energy  $E_{Vn}^f$  of a cluster of  $n$  vacancies to get

$$E_{Vn}^f = U_n - \frac{N-n}{N} U_0 + n \langle \text{Virial} \rangle \quad (4.20)$$



where  $U$  is the internal energy of a system containing an  $n$ -vacancy cluster.

Molecular statics is used to calculate the internal energy values required in Equation (4.20). We normally initialize the atoms to positions near the desired configuration and use the molecular statics code to minimize the configurational internal energy and determine the positions of the atoms in a stable or metastable state. As noted above, we only have to calculate the perfect lattice energy  $U_0$  and the virial term  $\langle \text{virial} \rangle$  once for a given lattice constant and potential, where potentials are distinguished between different materials, cutoff radii, etc. (Recall  $U_0$  scales linearly with the number of atoms  $N$ , and that  $\langle \text{virial} \rangle$  is independent of  $N$ ). The internal energy  $U$  of the lattice with the defect will be  $N$ -dependent to some extent and will obviously depend on the choice of potential.

#### 4.5.2 Binding Energy

The binding energy  $E_{Vn}^b$  of a cluster of  $n$  defects is the difference in formation energies  $E_{Vn}^f$  of the cluster and of  $n$  isolated defects,

$$E_{Vn}^b = nE_{V1}^f - E_{Vn}^f \quad (4.21)$$

Substituting (4.20) into (4.21),

$$E_{Vn}^b = n(U_1 - U_0) - (U_n - U_0) \quad (4.22)$$

where the virial term cancels.

Molecular statics is used to calculate the binding energy in the same way it is used to calculate the formation energy, and the same comments apply in this case. Note that it is not necessary to calculate the virial term  $\langle \text{virial} \rangle$  to calculate the binding energy.

#### 4.5.3 Migration Energy

In a static lattice, the migration energy of a defect is defined as the energy barrier that the defect must overcome to move from one position or configuration to another. In this section we will discuss a modification to the molecular statics method which allows one to calculate the migration energies of defects.

Let us look at a system of  $N$  atoms with coordinates  $r_i$ , where  $i = 1 \dots N$ , and configurational internal energy  $U(r_i)$ . Let site A be the current position of a vacancy, and site B be one neighboring sites to which the vacancy can jump. Coordinates  $r_i^A$  and  $r_i^B$  are the atomic coordinates corresponding sites A and B, and  $U_i^A = U(r_i^A)$  and  $U_i^B = U(r_i^B)$ . In Figure 4-6 a single vacancy is shown at site A in a two dimensional square lattice. For the

vacancy to jump to site B, atom 1 must jump in the reverse direction as shown. There are an infinite number of ways this jump can be accomplished. No matter what path is taken, however, atom 1 must cross a line drawn perpendicular to the jump direction. Let us define the position of this line by a reaction coordinate  $\eta$ , which in this simple case will be the y-coordinate of atom 1 when it is on the line,

$$\eta(r_i) = r_{1,y} \quad (4.23)$$

where  $r_1$  is the position of atom 1 and  $r_1 = (r_{1,x}, r_{1,y})$ . Every trajectory  $r_i(t)$  which goes from A to B must pass through a given  $\eta$ . The energy at the crossing is  $U(r_i | \eta(r_i) = \eta)$ . Let us define  $U(\eta)$  as the minimum of  $U(r_i | \eta(r_i) = \eta)$ , i.e.,

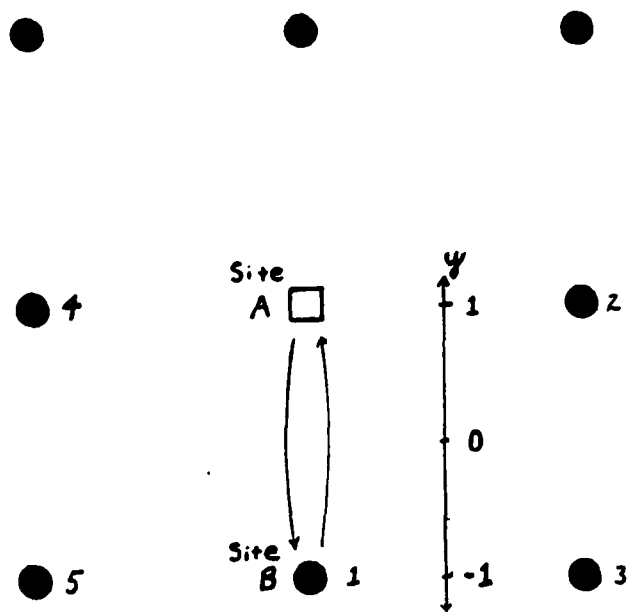
$$U(\eta) = \min_i U(r_i | \eta(r_i) = \eta) \quad (4.24)$$

$U(\eta)$  is thus the lowest possible energy at the crossing  $\eta(r_i) = \eta$ . The jumping atom must pass through all of the  $\eta$  values between -1 and 1 to make a successful jump. Even if an atom follows the lowest energy path (defined when  $U(r_i) = U(\eta(r_i))$ ), it will have to pass through the maximum of  $U(\eta)$ . We now define the migration energy  $E_{v1}^m$  by

$$E_{V1}^m = \max U(\eta) - U^A \quad (4.25)$$

Before developing the method for an fcc lattice, we need to make some revisions in our definition of the reaction coordinate  $\eta$ . Effectively,  $\eta$  serves as a constraint on the system by limiting the possible configurations. (Note: this is a constraint in the physical sense because we are forcing the system to be in a higher energy state; this is not what is considered a constraint in the mathematical sense.) Equations (4.23) and (4.24) constrain the system by forcing atom 1 to have a specific absolute y coordinate. In molecular statics with periodic boundaries, the system can be translated in any direction without affecting the energy of the system because the energies are all calculated from relative distances between atoms. If a single atom is constrained to a specific absolute location, the whole lattice will slowly drift to a minimum energy which is independent of the constraint (i.e., there is not a one-to-one correspondence between the reaction coordinate and the system energy). The solution to this problem is to define a reaction coordinate which is anchored to the atoms in the lattice but which has a similar physical meaning. A reasonable choice in the two dimensional case is

Figure 4-6: Vacancy Jump in a Square Lattice



$$\eta_i(r_i) = r_{1,y} - \frac{r_{2,y} + r_{3,y} + r_{4,y} + r_{5,y}}{4} \quad (4.26)$$

As long as atoms 2 through 5 stay in reasonable positions, the reaction coordinate  $\eta$  is well-defined, is anchored to the lattice, and has the same physical meaning as Equation (4.23).

Now that we have looked at the basic ideas of the technique in two dimensions, let us develop the method for an fcc lattice and look at the details of computer implementation. We will first define the reaction coordinate  $\eta$  for the three dimensional case. In Figure 4-7 atom 1 must move through the "gate" of atoms 2 through 5 to make a successful jump. As before we wish to define a reaction coordinate  $\eta$  which in this case refers to a plane instead of a line. We can define a reaction coordinate  $\eta$  to describe the position of atom 1 during the jump,

$$\eta_i(r_i) = \gamma \underline{u} \cdot r_1 - \frac{r_2 + r_3 + r_4 + r_5}{4} \quad (4.27)$$

where  $\underline{u} = [\sqrt{2}/2, \sqrt{2}/2, 0]$  and  $\gamma$  is a scaling factor. We set  $\gamma = (\sqrt{2}a/4)^{-1}$ , where  $a$  is the lattice constant, so that  $-1 < \eta < 1$ .

Now let us look at the details of the implementation

AD-A166 742

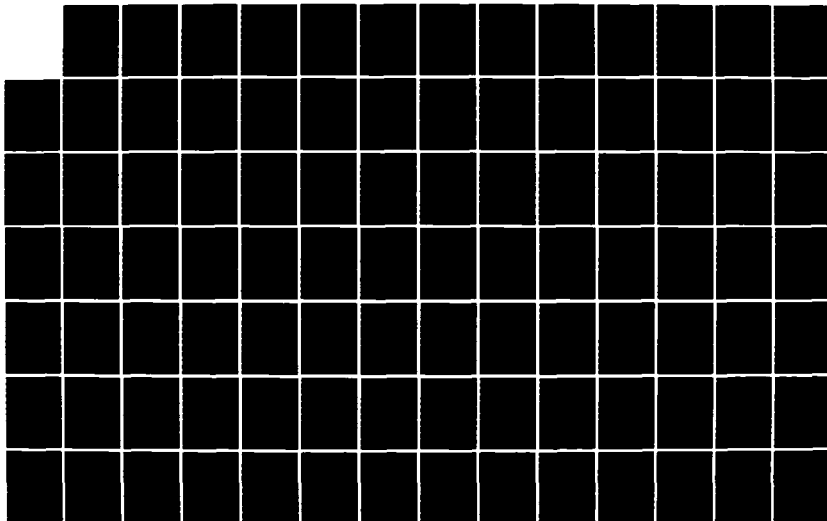
ATOMISTIC SIMULATION STUDY OF VACANCY CLUSTERS IN  
COPPER(U) AIR FORCE INST OF TECH WRIGHT-PATTERSON AFB  
OH W J SABOCHICK 1985 AFIT/CI/NR-86-350

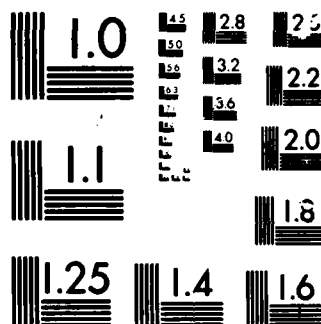
2/3

UNCLASSIFIED

F/G 11/6

NL



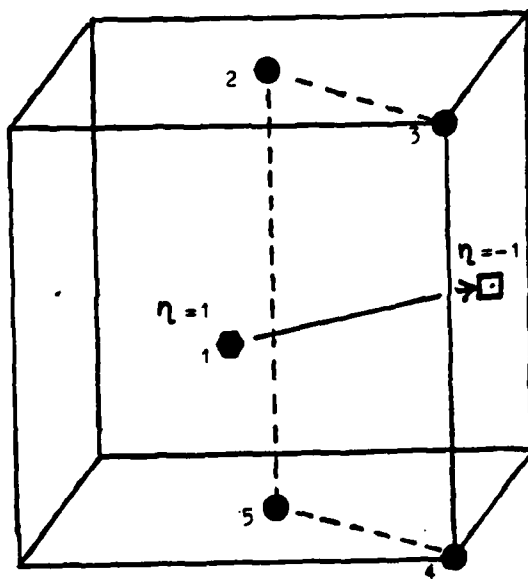


MICROCOPY

CHART



Figure 4-7: Migration Path for a Vacancy Jump



of the method. The basic problem is to calculate  $U(\eta)$  as given by Equation (4.24), Note that an energy minimization is required to determine  $U(\eta)$  from Equation (4.24). Molecular statics is ideally suited for this, provided we can find a way to enforce the constraint  $\eta(r_i) = \eta$ . The most natural way to add the constraint is to add an extra term to the Lagrangian for the system. For the unconstrained system, the Lagrangian  $L$  is

$$L = T - U \quad (4.28)$$

where  $T$  and  $U$  are the kinetic and potential energies, respectively. Lagrange's equations are then

$$\frac{d}{dt} \frac{\partial L}{\partial p_j} - \frac{\partial L}{\partial q_j} = 0 \quad (4.29)$$

$$\frac{d}{dt} \frac{\partial T}{\partial p_j} + \frac{\partial U}{\partial q_j} = 0 \quad (4.30)$$

where  $q_j$  is a coordinate and  $p_j = dq_j/dt$ . The constrained Lagrangian  $LC$  is the same as Equation (4.28) with an extra term,

$$LC = T - (U + UC) \quad (4.31)$$

where  $UC = UC(\eta)$ . Lagrange's equations for  $LC$  are

$$\frac{d}{dt} \frac{\partial T}{\partial p_j} + \frac{\partial U}{\partial q_j} + \frac{\partial UC}{\partial q_j} = 0 \quad (4.32)$$

where the first two terms are the same as in (4.30), and we assume that UC is not a function of  $p_j$ . The third term can be expanded

$$\frac{\partial UC}{\partial q_j} = \frac{dUC}{d\eta} \cdot \frac{\partial \eta}{\partial q_j} \quad (4.33)$$

Newton's equations for the constrained system are then

$$m \frac{dv_{km}}{dt} = \frac{\partial U}{\partial r_{km}} - \frac{dUC}{d\eta} \cdot \frac{\partial \eta}{\partial r_{km}} \quad (4.34)$$

where  $q_j = r_{km}$ ,  $p_j = v_{km}$ ,  $k$  is the atom number, and  $m$  is the coordinate ( $x$ ,  $y$ , or  $z$ ).

We now need to specify  $UC(\eta)$ . The effect of  $UC(\eta)$  on the system should be to artificially increase the potential energy when the system deviates from the desired constrained configuration. In this case,  $UC(\eta)$  should increase when  $\eta(r_i)$  deviates from the desired value of  $\eta$ . Another feature of  $UC(\eta)$  imposed by limitations of numerical integrating schemes is that it should not contain discontinuities. A simple form for  $UC(\eta)$  which has these qualities is

$$UC(\eta) = \gamma [\eta(r_i) - \beta]^2 \quad (4.35)$$

where  $\beta$  is the desired value of  $\eta(r_i)$  and  $\gamma$  is a constant. Figure 4-8 shows the effect of adding  $UC(\eta)$  defined by (4.35) to the unconstrained potential energy  $U(\eta)$ . The

energy minimum is now near the desired value of  $\eta$ , and the molecular statics code will converge to this configuration. Substituting into (4.33) and letting  $r_{km} = q_j$ ,

$$\frac{\partial UC}{\partial r_{km}} = 2 \gamma [\eta(r_i) - \beta] \cdot \frac{\partial \eta}{\partial r_{km}} \quad (4.36)$$

and from (4.27)

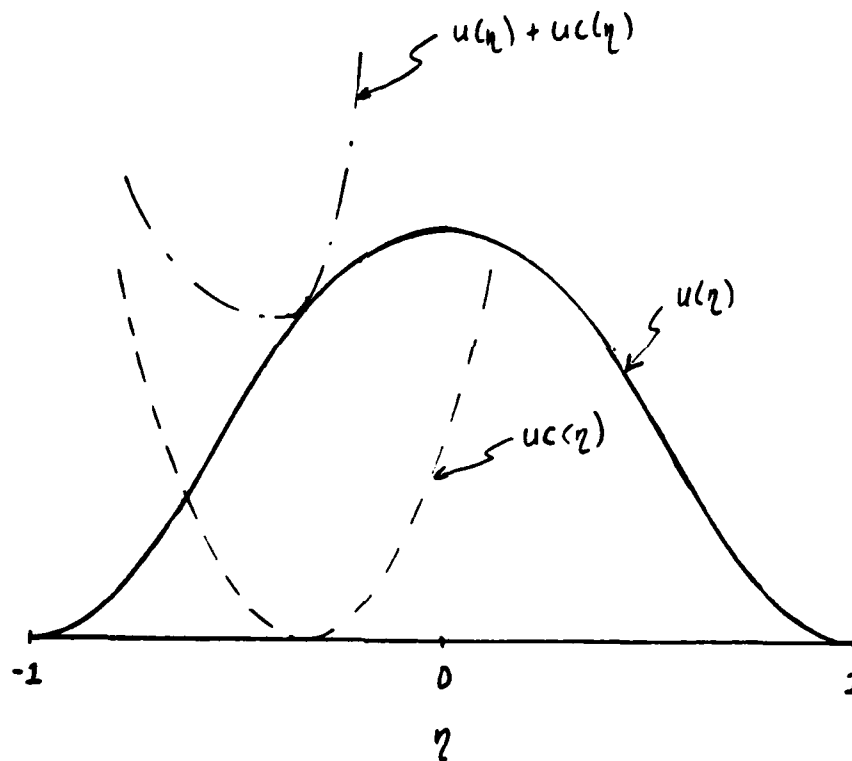
$$\frac{\partial \eta}{\partial r_{km}} = \begin{cases} -j_m \gamma & k = 1 \\ \frac{1}{4} j_m \gamma & k = 2 \dots 5 \\ 0 & k > 5 \end{cases} \quad (4.37)$$

where  $j_m$  is the  $m^{th}$  component of  $j$ .

The simplicity of the method is shown in Equation (4.37). The only atoms that contribute to the constraint implementation are those specifically included in the definition of  $\eta$ , and only these atoms are directly affected. Also note that we can implement the constraint technique independently of the calculation of the interatomic forces, which means that it can be superimposed on those calculations. The molecular statics code runs in basically the same way as when it is unconstrained. The difference is that we add  $UC(\eta)$  from Equation (4.35) to the configurational internal (or total potential) energy, and we add contributions to the forces

**Figure 4-8: Effect of Constraint on the Potential Energy**

$U(\eta)$  is the unconstrained potential energy;  $UC(\eta)$  is the additional energy added from the constraint. Note how the minimum of  $U(\eta) + UC(\eta)$  is now near the minimum of  $UC(\eta)$ .



given by Equations (4.36) and (4.37). The effect of these additions is to constrain the system near some desired value of  $\eta(r_i)$ .

## Chapter 5

### Bulk Properties

#### 5.1 Introduction

The main thrust of this work is the calculation of the properties of vacancy defects in copper. As was pointed out in Chapter 1, many defect properties have not been experimentally determined and hence the computational results are difficult to verify. The molecular statics (MS) and molecular dynamics (MD) methods are powerful enough, however, to allow one to calculate many different physical properties using the same interatomic potential. The purpose of the work discussed in this Chapter is to calculate the thermodynamic and vibrational properties of the copper potential using MD techniques and compare them with experimental results. While correspondence between calculations and experiment in one property does not guarantee the same in another, this way of testing a given potential is just about the only way of determining its range of applicability.

To make the test of the Dagens' potential even more complete, similar calculations are also performed using the modified Morse potential<sup>29</sup> discussed in Section 2.2.

By repeating the calculations with a different potential, one can better evaluate the sensitivity of the calculated property to detailed features of the potential. As is well-known, there are not many materials for which a single potential is recommended for all properties, and as was discussed in Chapter 2, many interatomic potentials have been used for copper.

## 5.2 Thermodynamic Properties

The thermodynamic properties calculated in this Chapter are the temperature, volume, pressure, total energy and enthalpy. The behavior of these properties with temperature allow us to estimate the specific heat and linear thermal expansion coefficient. To obtain some information on the structure of the system, the order parameter and mean-square displacement are also calculated. Melting is a first order transition, and properties such as the total energy and enthalpy are discontinuous at the melting point. This transition can be determined from a series of runs, and combined with information given by the order parameter, mean-square displacement, and the radial distribution function, can be used to estimate the melting point of the system. The results of these calculations are presented in this Section.

The formulas and methodology for the calculation of



thermodynamics properties were discussed in Chapter 3. It was noted that all of the properties calculated in this work are functions of positions and velocities. From a single configuration of the system, i.e., a single set of positions  $r$  and velocities  $v$  of all the atoms, a single or instantaneous value of some property  $A(r, v)$  can be calculated. In a constant-volume or microcanonical simulation, however, all of the thermodynamic properties fluctuate except for the total energy  $E$ , the volume  $V$ , and the number of atoms  $N$ . If the system remains in a single phase, the properties fluctuate about an average value  $\langle A \rangle$ , where  $\langle A \rangle$  is the average of  $A(r, v)$  over all time. As one might expect, the value of  $A(r, v)$  between one time step and the next are correlated (because of limitations of the integrator, atoms can only move a short distance during a step). Consequently, thousands of time steps are required to get a reliable estimate of  $\langle A \rangle$ .

In Chapter 2 it was noted that the structure-independent part of Dagens' noble metal potential is very difficult to calculate and was not available for this work. Since the simulation pressure depends on the structure-independent contribution, only a limited number of derived thermodynamic properties could be calculated. Furthermore, it was impossible to calculate the properties at ambient pressure, where experimental results are usually quoted. To attempt a comparison with experimental

data, thermodynamic properties were calculated at three specific volumes using conventional (constant-volume) molecular dynamics. The simulation volumes  $V_0$ ,  $V_s$ , and  $V_l$  correspond, respectively, to the density of copper at ambient pressure and temperature (1 atmosphere and 298K); the density of solid copper at melting at ambient pressure; and the density of liquid copper at melting under ambient pressure. This is summarized in Table 5-1, in which  $T_m = 1357K$  is the melting temperature of copper. At these volumes one can calculate the melting point of the potential and make some tentative comparisons with real copper, assuming the thermal expansion of the computer and real copper are identical. The structure-dependent part of Dagens' potential, which is the part of the potential used in MD and MS, is also volume dependent. Even if the structure-independent part of the potential was available, strictly speaking a different interatomic potential must be used at each simulation volume. Only the single interatomic potential given by  $\lambda_m$  and specified by equation (2.7) was available for this work and was used in all calculations. It is not possible to say how sensitive the form of the interatomic potential is to the total volume without actually deriving the potential at different volumes.

The modified Morse potential used for the parallel property calculations is not volume dependent nor does it

|       | Volume of<br>Unit Cell [ $\text{\AA}^3$ ] | Corresponding State in<br>Real Copper              |
|-------|---|--|
| $V_0$ | 47.242                                    | $T = 298\text{K}, P = 1 \text{ atm}$               |
| $V_s$ | 50.489                                    | $T = T_m, P = 1 \text{ atm}, \text{ solid phase}$  |
| $V_l$ | 53.115                                    | $T = T_m, P = 1 \text{ atm}, \text{ liquid phase}$ |

Table 5-1: Simulation Volumes Used in  
Property Calculations with Dagens'  
Copper Potential

have a structure-independent component. Consequently, it is possible to calculate all of thermodynamic properties of the potential including the pressure. To take advantage of this fact, the flexible border Parrinello-Rahman method was used for the property calculations. The system pressure was set to 0 GPa (effectively, 1 atmosphere). Since experimental properties are normally calculated at this pressure, direct comparisons of all properties could be made.

In all of the thermodynamic property calculations, 256 atoms were used. In the opinion of the author, this is probably a sufficient number of atoms based on previous experience with calculations done for argon using the Lennard-Jones 6-12 potential. The cutoff radius for Dagens' potential was set at 4.9241  $\text{\AA}$ , which is shorter than the cutoff radius used in the defect calculations reported in Chapters 6 and 7. This cutoff is equivalent to  $1.4a$ , where  $a$  is the lattice constant. While the

author believes that the results of this work would not be significantly different if a longer cutoff radius was used, this possibility was not extensively tested. As noted above, thousands of time steps are necessary to calculate reliable averages of the fluctuating properties. Most of the properties reported in the following sections were averaged over 4000 to 6000 time steps; in some cases, longer runs were made when it was suspected that the system was in a metastable state. This point will be addressed in more detail below.

The results of the thermodynamic and related property calculations are presented in Tables 5-2 through 5-5. All of the thermodynamic property values shown are time averages except for the total energy  $E$  and unit cell volume  $V$  for Dagens' potential and the total enthalpy  $H$  for the modified Morse potential, which are constants of motion in these simulations. The numbers of time steps over which properties and their averages were calculated are given in Table 5-3 and 5-5 for each run. In most cases the averages were calculated over 4000 steps. Some the properties are plotted in Figures 5-1 through 5-7 and will be discussed below. The melting transition is indicated in many of the Figures; the discussion of melting will follow the presentation of the results.

The mean-square displacements (MSD) for the pseudopotential and the modified Morse potentials in the

| Run | <T><br>[K] | <P><br>[KJ/Kg] | <U><br>[KJ/Kg] | <V><br><sup>3</sup><br>[A ] | <E><br>[KJ/Kg] |
|-----|------------|----------------|----------------|-----------------------------|----------------|
| 1   | 0.0        | 22.7           | 494.           | 47.242                      | 493.94         |
| 2   | 280.2      | 23.6           | 550.           | 47.242                      | 604.95         |
| 3   | 285.8      | 23.7           | 551.           | 47.242                      | 606.91         |
| 4   | 921.5      | 26.1           | 683.           | 47.242                      | 863.77         |
| 5   | 1402.2     | 28.2           | 790.           | 47.242                      | 1065.80        |
| 6   | 1904.6     | 30.6           | 917.           | 47.242                      | 1291.16        |
| 7   | 2187.5     | 32.6           | 1032.          | 47.242                      | 1460.93        |
| 8   | 1917.3     | 33.5           | 1085.          | 47.242                      | 1461.04        |
| 9   | 2518.5     | 36.5           | 1222.          | 47.242                      | 1716.37        |
| 10  | 2767.9     | 37.8           | 1284.          | 47.242                      | 1826.88        |
| 11  | 449.9      | 15.9           | 446.           | 50.489                      | 534.27         |
| 12  | 895.6      | 17.8           | 540.           | 50.489                      | 716.06         |
| 13  | 1459.2     | 20.5           | 672.           | 50.489                      | 958.00         |
| 14  | 1576.2     | 21.2           | 705.           | 50.489                      | 1015.18        |
| 15  | 1585.0     | 21.3           | 704.           | 50.489                      | 1015.20        |
| 16  | 1775.1     | 22.4           | 758.           | 50.489                      | 1106.21        |
| 17  | 1827.4     | 24.9           | 885.           | 50.489                      | 1243.21        |
| a17 | 1758.2     | 25.3           | 898.           | 50.489                      | 1243.21        |
| 18  | 2101.5     | 27.2           | 982.           | 50.489                      | 1394.43        |
| 19  | 2558.1     | 29.4           | 1079.          | 50.489                      | 1581.44        |
| 20  | 773.3      | 12.2           | 445.           | 53.115                      | 598.77         |
| 21  | 931.3      | 13.0           | 482.           | 53.115                      | 665.11         |
| 22  | 1193.4     | 14.5           | 544.           | 53.115                      | 778.59         |
| 23  | 1219.3     | 14.7           | 551.           | 53.115                      | 790.61         |
| 24  | 1294.6     | 15.0           | 567.           | 53.115                      | 821.33         |
| 25  | 1357.1     | 18.8           | 728.           | 53.115                      | 994.27         |
| 26  | 1952.8     | 22.1           | 869.           | 53.115                      | 1252.35        |
| 27  | 2460.3     | 24.5           | 962.           | 53.115                      | 1444.87        |

Table 5-2: Thermodynamic Properties of  
Dagens' Potential (Part I)

solid phase are plotted in Figures 5-1 and 5-2. The MSD is calculated using equation (3.19). It is evident from Figure 5-1 and 5-2 that the MSD increases with increasing temperature. This can be explained by imagining that each

| Run | <T><br>[K] | Order | MSD <sup>2</sup><br>[A ] | Phase | Steps |
|-----|------------|-------|--------------------------|-------|-------|
| 1   | 0.0        | 1.00  | 0.0                      | s     | 1     |
| 2   | 280.2      | 0.91  | 0.07                     | s     | 2000  |
| 3   | 285.8      | 0.91  | 0.05                     | s     | 4000  |
| 4   | 921.5      | 0.75  | 0.18                     | s     | 4000  |
| 5   | 1402.2     | 0.62  | 0.24                     | s     | 4000  |
| 6   | 1904.6     | 0.46  | 0.44                     | s     | 4000  |
| 7   | 2187.5     | 0.27  | 1.07                     | s->l  | 4000  |
| 8   | 1917.3     | 0.01  | 13.97                    | l     | 6000  |
| 9   | 2518.5     | 0.00  | 9.27                     | l     | 2000  |
| 10  | 2767.9     | 0.00  | 8.90                     | l     | 2000  |
| 11  | 449.9      | 0.88  | 0.07                     | s     | 4000  |
| 12  | 895.6      | 0.76  | 0.14                     | s     | 4000  |
| 13  | 1459.2     | 0.57  | 0.35                     | s     | 4000  |
| 14  | 1576.2     | 0.50  | 0.34                     | s     | 4000  |
| 15  | 1585.0     | 0.53  | 0.38                     | s     | 4000  |
| 16  | 1775.1     | 0.45  | 0.42                     | s     | 4000  |
| 17  | 1827.4     | 0.09  | 6.88                     | s->l  | 4000  |
| a17 | 1758.2     | 0.00  |                          | l     | 1000  |
| 18  | 2101.5     | 0.00  | 10.67                    | l     | 3000  |
| 19  | 2558.1     | 0.00  | 16.78                    | l     | 3000  |
| 20  | 773.3      | 0.75  | 0.16                     | s     | 4000  |
| 21  | 931.3      | 0.70  | 0.19                     | s     | 4000  |
| 22  | 1193.4     | 0.61  | 0.32                     | s     | 4000  |
| 23  | 1219.3     | 0.62  | 0.30                     | s     | 4000  |
| 24  | 1294.6     | 0.60  | 0.31                     | s     | 4000  |
| 25  | 1357.1     | 0.01  | 6.78                     | l     | 4000  |
| 26  | 1952.8     | 0.00  | 10.90                    | l     | 3000  |
| 27  | 2460.3     | 0.00  | 16.99                    | l     | 3000  |

Table 5-3: Thermodynamic Properties of  
Dagens' Potential (Part II)

atom is inside of a local energy well whose minimum is at the perfect lattice site. As the temperature increases, the atom is able to climb further up the sides of the well and hence the average displacement of the atom also

| Run | <T><br>[K] | <P><br>[GPa] | <U><br>[KJ/Kg] | <V><br>3<br>[A ] | <H><br>[KJ/Kg] |
|-----|------------|--------------|----------------|------------------|----------------|
| 28  | 0.0        | 0.0          | -1962.         | 46.8             | -1962.10       |
| 29  | 283.7      | 0.0          | -1902.         | 47.5             | -1846.18       |
| 30  | 295.2      | 0.1          | -1900.         | 47.5             | -1841.15       |
| 31  | 302.1      | 0.0          | -1899.         | 47.1             | -1838.74       |
| 32  | 921.5      | 0.1          | -1741.         | 49.6             | -1557.00       |
| 33  | 1180.6     | 0.0          | -1654.         | 51.0             | -1417.78       |
| 34  | 1329.3     | 0.0          | -1600.         | 51.9             | -1335.93       |
| 35  | 1401.9     | 0.0          | -1563.         | 52.6             | -1284.82       |
| 36  | 1416.0     | 0.0          | -1566.         | 52.5             | -1284.76       |
| 37  | 1226.2     | 0.0          | -1444.         | 54.9             | -1172.84       |
| 38  | 1359.8     | 0.0          | -1415.         | 55.7             | -1172.78       |
| 39  | 1512.5     | 0.0          | -1282.         | 59.4             | -982.54        |
| 40  | 1766.0     | 0.1          | -1147.         | 65.0             | -797.80        |

Table 5-4: Thermodynamic Properties of  
Modified Morse Potential (Part I)

increases. The MSD for Dagens' potential shown in Figure 5-1 is calculated at three different system volumes. Note that as the system volume increases from  $V_0$  to  $V_1$ , the MSD also increases at constant temperature. Dagens' potential is repulsive at these volumes (note that the system pressure is always positive), and hence the local potential energy well of an atom becomes shallower as the volume increases which allows atoms to be displaced further at larger volumes. It has been estimated that when the the root-mean-square displacement exceeds 15-20% of the nearest neighbor distance, the solid phase is unstable and a phase change to the liquid phase should

| Run | <T><br>[K] | Order | MSD <sup>2</sup><br>[A ] | Phase | Steps |
|-----|------------|-------|--------------------------|-------|-------|
| 28  | 0.0        | 1.00  | 0.00                     | s     | 1     |
| 29  | 283.7      | 0.94  | 0.06                     | s     | 4000  |
| 30  | 295.2      | 0.94  | 0.06                     | s     | 3000  |
| 31  | 302.1      | 0.93  | 0.07                     | s     | 2000  |
| 32  | 921.5      | 0.77  | 0.27                     | s     | 3000  |
| 33  | 1180.6     | 0.67  | 0.42                     | s     | 5000  |
| 34  | 1329.3     | 0.60  | 0.49                     | s     | 4000  |
| 35  | 1401.9     | 0.50  | 0.75                     | s     | 1000  |
| 36  | 1416.0     | 0.56  | 0.74                     | s     | 6000  |
| 37  | 1226.2     | 0.01  | 10.05                    | l     | 4000  |
| 38  | 1359.8     | 0.13  | 6.58                     | s->l  | 5000  |
| 39  | 1512.5     | 0.00  | 15.85                    | l     | 3000  |
| 40  | 1766.0     | 0.00  | 23.47                    | l     | 3000  |

Table 5-5: Thermodynamic Properties of  
Modified Morse Potential (Part II)

60 occur . The MSD corresponding to the root-mean-square displacement of 20% of the nearest neighbor distance is indicated in Figures 5-1 and 5-2, and in all cases the calculated MSD exceeded this value without a phase change occurring. It is possible that the simulation run times were not sufficiently long for the phase change to occur, although it is noted that the particularly high value of 0.74 A in Figure 5-2 was averaged over 7000 time steps. The problems associated with determining the melting point will be discussed in more detail below.

The calculated total energy for Dagens' potential is



Figure 5-1: MSD vs Temperature for Dagens' Potential

The arrow indicates a root-mean square displacement of the 20% of the nearest neighbor distance.

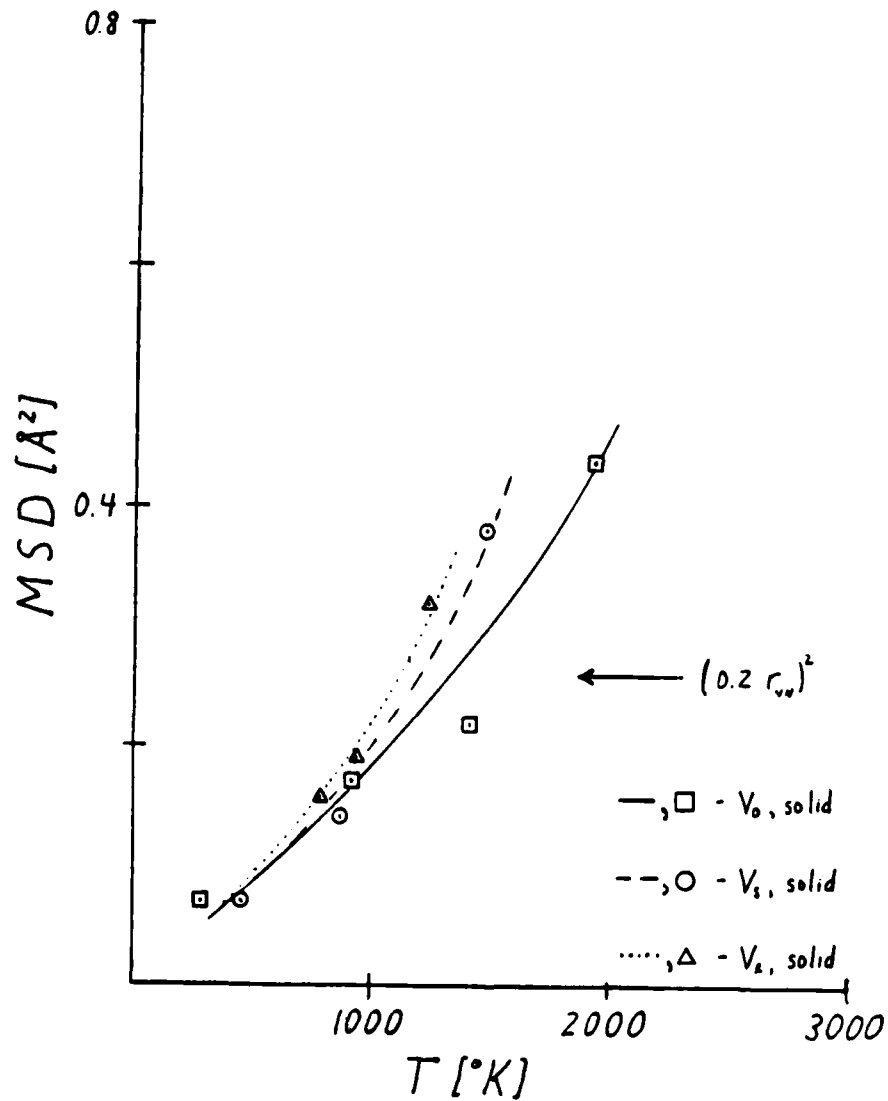
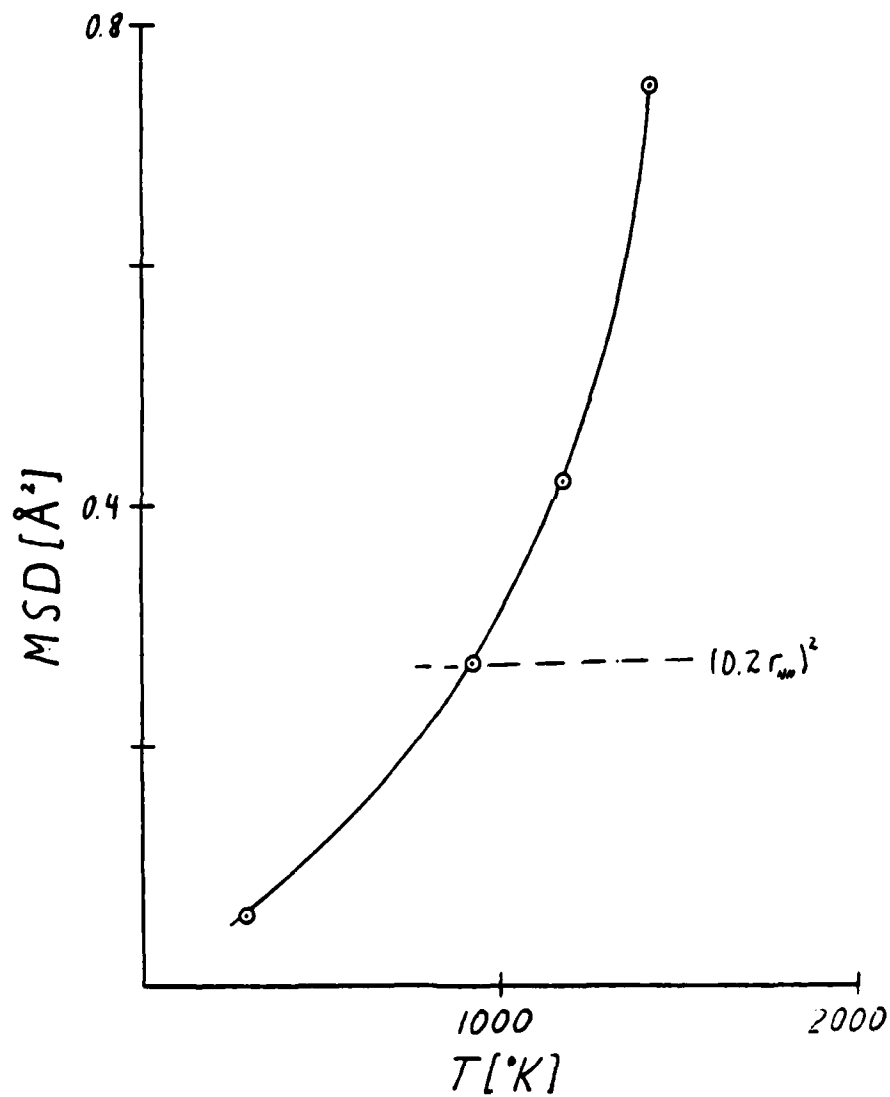


**Figure 5-2: MSD vs Temperature for the Modified Morse Potential**

The dashed line indicates a root-mean square displacement of 20% of the nearest neighbor distance.



plotted in Figure 5-3. The total energy  $E$  is the sum of the kinetic and potential energies of the system and is calculated using equations (3.11) through (3.13). As noted above, three different system volumes were used for the thermodynamic property calculations using Dagens' potential. As the volume of the system is increased at constant temperature, the total energy of the system decreases. This is caused by the repulsive nature of the potential at these densities, which causes the interaction energy between atoms to decrease as they are moved apart from one another. Figure 5-3 also indicates that the total energy increases with increasing temperature for a fixed volume. This is caused not only by the increase in the kinetic energy of the system, which is proportional to the temperature as shown in equation (3.15), but also by the fact that the atoms on average are further displaced from the ideal lattice sites as the temperature increases as shown in Figure 5-1 and 5-2. Consequently, the total energy increases as the temperature increases. At some point on each curve, a vertical bar indicates that a transition occurs and the total energy increases abruptly. This point indicates the melting point at the given volumes, which will be discussed in more detail below. It is also noted that the two data points, marked A and B, are slightly supercooled, although the difference in temperatures between these points and their corresponding

melting points are within the uncertainties of the melting temperatures.

The calculated enthalpy for the modified Morse potential is plotted in Figure 5-4. The enthalpy is calculated using equation (3.17). All of the modified Morse thermodynamic calculations were performed at zero pressure. As in Figure 5-3, the enthalpy also increases with increasing temperature for the same reasons. Assuming that the indicated melting point of the potential is correct, the point marked C is definitely supercooled. This point is Run 37 in Tables 5-4 and 5-5, and the properties were calculated over 4000 time steps.

The pressure, calculated using equation (3.16), is plotted for Dagens' potential in Figure 5-5. It is apparent from Figure 5-5 that a large external pressure is necessary to maintain the system at the given volumes. The reason the pressure is so large is that the cohesive energy provided by the electrons has not been included in the pressure calculations as discussed in Section 3.3. Figure 5-5 indicates that the calculated pressure increases with increasing temperature. This behavior is caused by the anharmonicity of the interatomic potential as indicated in Figure 2-1. As noted above, as the temperature is increased, the displacement of the atoms from their perfect lattice sites also increases. In Figure 2-1, we note that the potential energy increases

**Figure 5-3: Total Energy vs Temperature for the Pseudopotential**

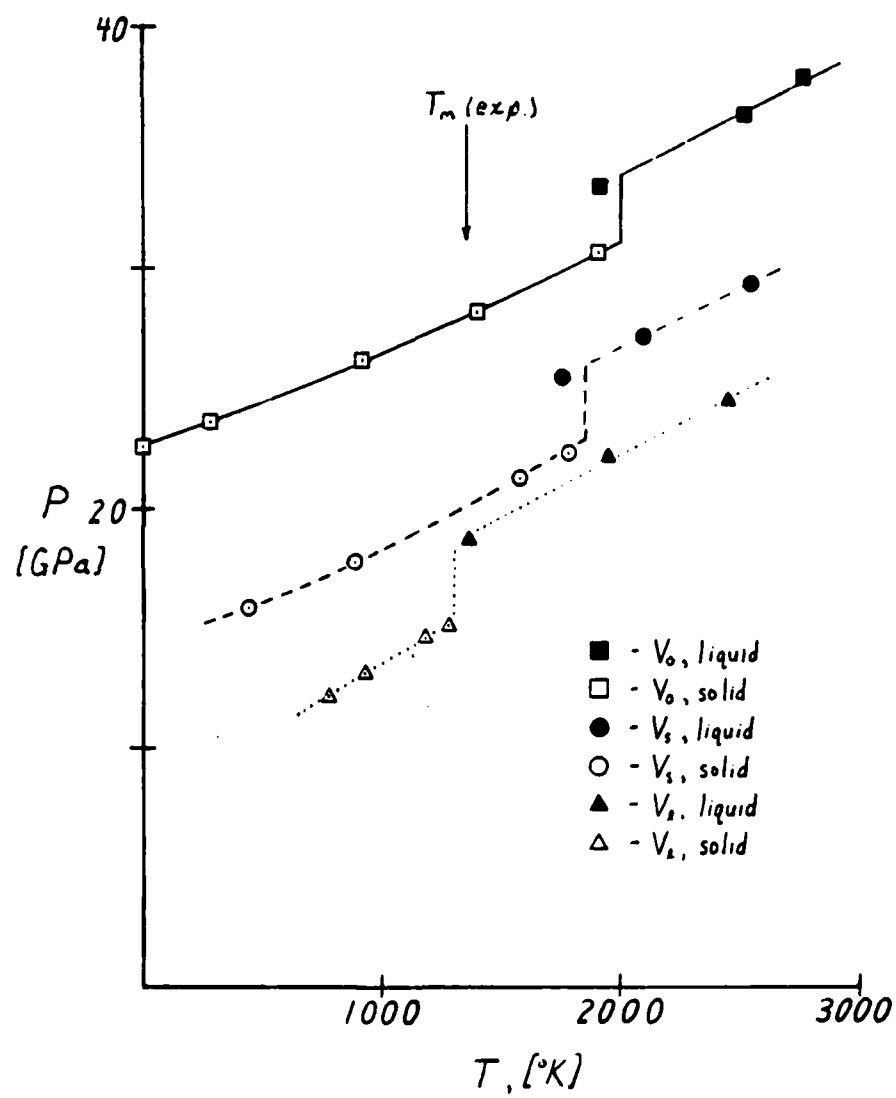
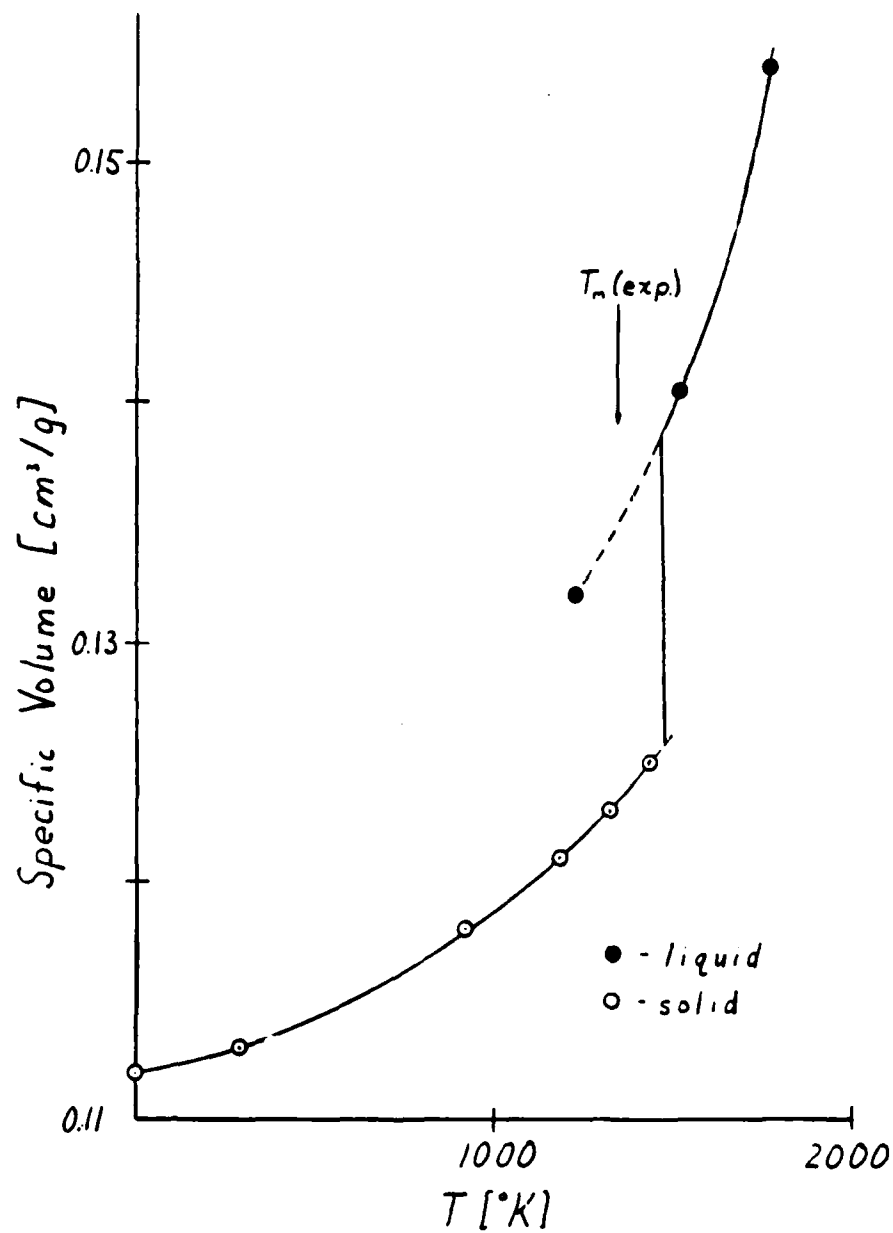


Figure 5-4: Enthalpy vs Temperature for the Modified Morse Potential



dramatically with decreasing interatomic radius compared to the change as the interatomic radius increases. At greater average displacements, the average position of an atom will tend to be at larger interatomic radii. Consequently, to maintain the same average position and the same volume, an external pressure must be applied. As with the total energy, the pressure also experiences a first order transition at melting indicated by the vertical bars.

The specific volumes of the modified Morse potential simulations versus temperature are plotted in Figure 5-6. The behavior of the volume in a constant pressure simulation is qualitatively similar to the behavior of the pressure in a constant volume simulation. The volume of the system increases with increasing temperature, indicating that the potential is anharmonic. The specific volume also increases at the melting point, indicating that the system is less dense as a liquid.

In Figure 5-7 the order parameter defined by equation (3.20) is plotted for Dagens' potential. The order parameter can be used to determine the order of a state and thus whether or not the system is a solid or liquid. The parameter is designed to range between 0 and 1 inclusive, such that a 1 refers to a perfectly ordered system (a cold fcc lattice, for example), and 0 refers to a totally disordered system. In Figure 5-7 the parameter

**Figure 5-5:** Pressure vs Temperature for Dagens' Potential

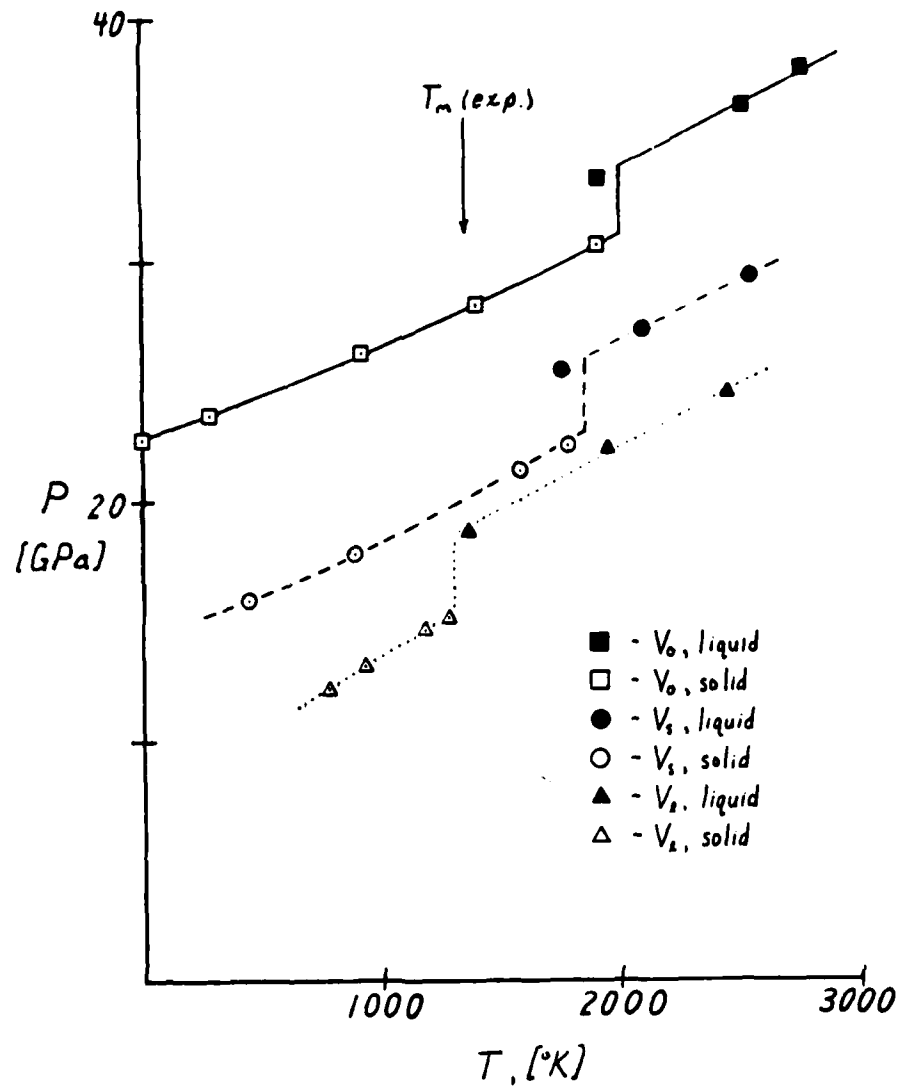
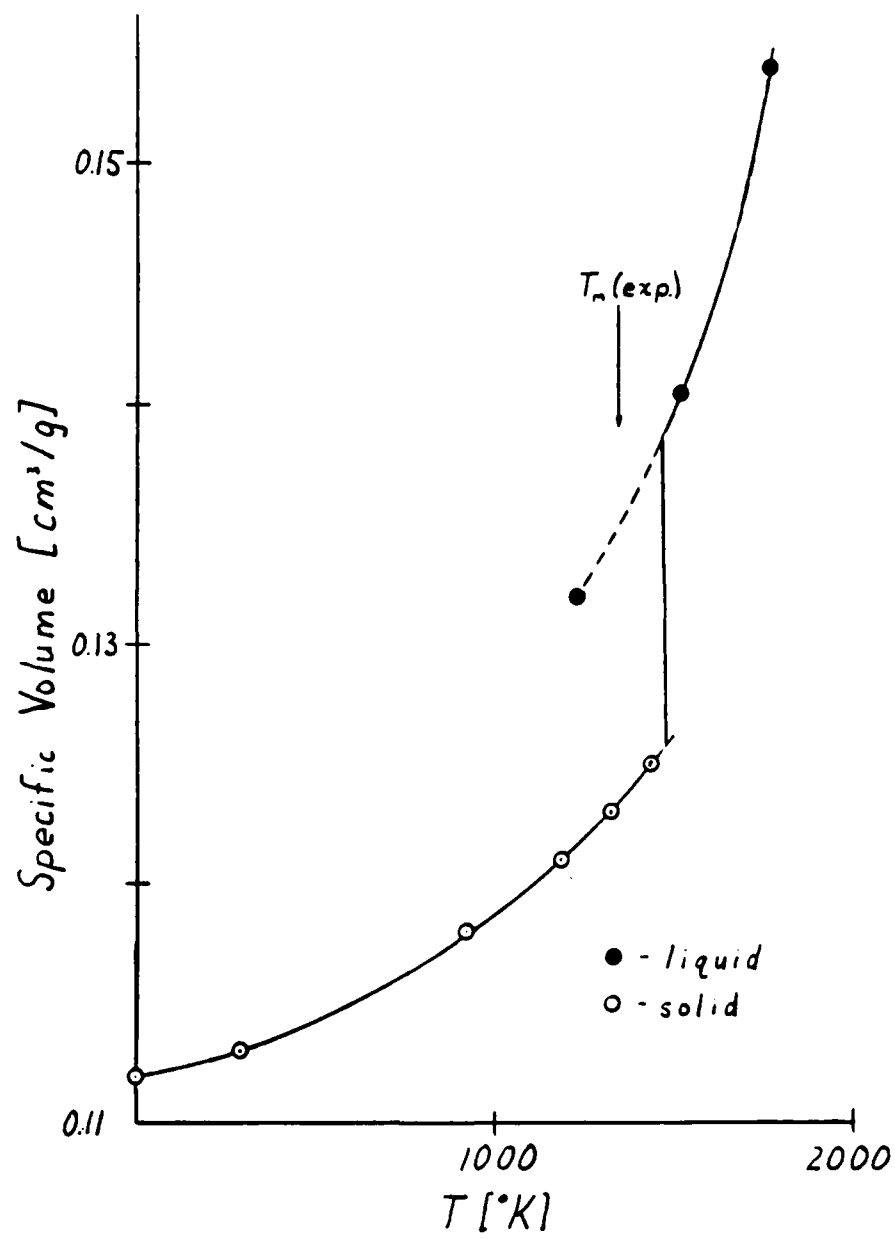




Figure 5-6: Volume vs Temperature for the Modified Morse Potential



is plotted for the volume  $V_0$  for the pseudopotential. It is interesting to note that in the simulations at the largest volume,  $V_1$ , the order parameter only decreases to 0.6 before melting, whereas it decreases to 0.45 at volumes  $V_s$  and  $V_0$ .

Derived thermodynamic properties can be determined from the thermodynamic data in Tables 5-2 and 5-4. The following properties are calculated as derivatives and differences of the properties in these Tables:

- Specific heat at constant volume:

$$c_v = \left. \frac{dE}{dT} \right|_{\text{constant } V} \quad (5.1)$$

- Specific heat at constant pressure:

$$c_p = \left. \frac{dH}{dT} \right|_{\text{constant } P} \quad (5.2)$$

- Bulk modulus:

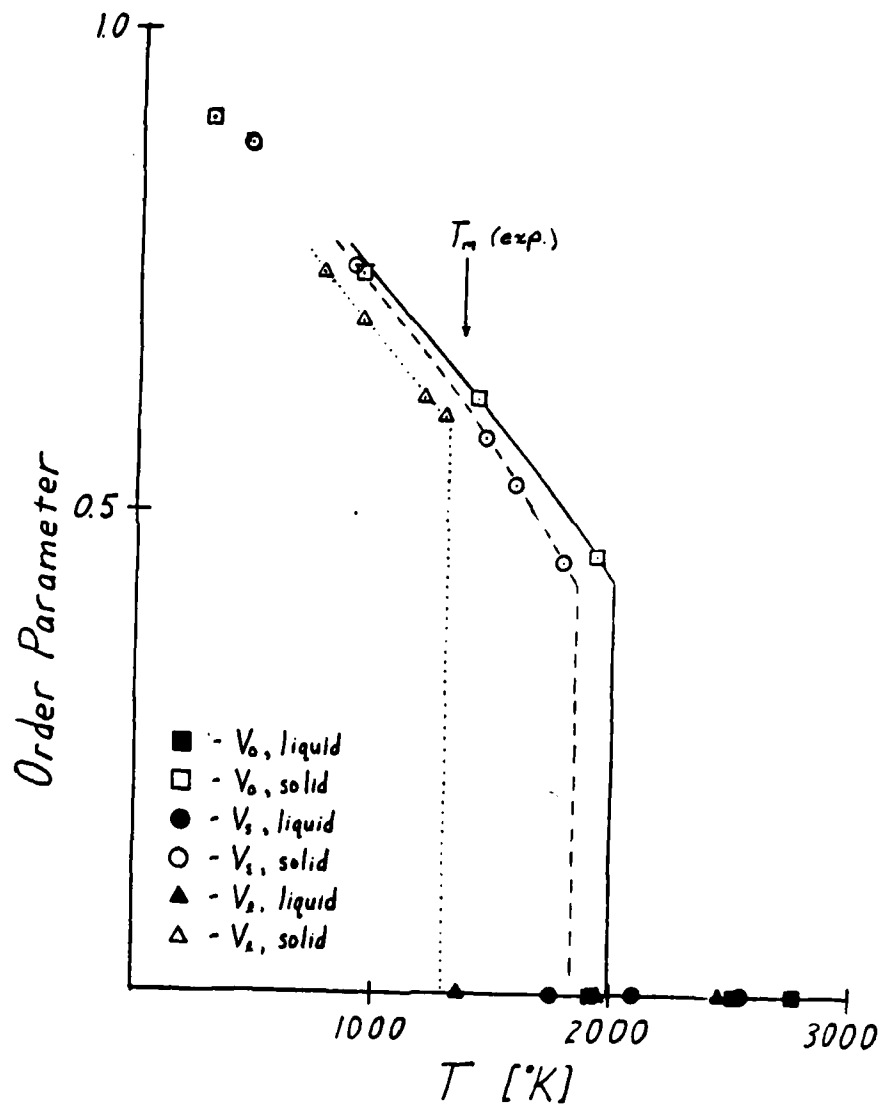
$$B = -V \frac{dP}{dV} \quad (5.3)$$

- Bulk thermal expansion coefficient:

$$\alpha_T = \frac{dV}{dT} \quad (5.4)$$

The latent heat of melting  $\Delta H_m$  and  $\Delta E_m$ , are given by the differences in the enthalpy and the total energy,

**Figure 5-7: Order Parameter vs Temperature for Dagens' Potential**



respectively, of the liquid and solid states at the melting temperature. The volume change on melting is given by the change in volume during the melting transition, at a constant temperature. The results of the calculations of these properties are shown in Table 5-6. It is noted that the selection of the system volumes for the Dagens' potential property calculations already assumes that the thermal expansion properties are correct, and hence the thermal expansion coefficient and the volume change on melting cannot be determined from these calculations.

Table 5-6 indicates that many of the of derived properties for both potentials are in good agreement with experimental results. The bulk modulus for Dagens' potential is within twenty percent of the experimental value at 293K. It is noted that a bulk modulus of 140 GPa for Dagens' potential has already been calculated at 0K, <sup>15</sup> which gives even better agreement. The specific heats calculated using both potentials are within ten percent of the experimental values. The thermal expansion coefficient for the modified Morse potential is within five percent of the experimental value at 293K. Table 5-6 therefore shows that both potentials are more accurate at low temperatures, and near the melting point the calculations differ significantly from experimental data. Near melting, however, there are large differences in the

| <u>Property</u>      | <u>Dagens</u> | <u>Mod. Morse</u>     | <u>Exp</u>            |
|----------------------|---------------|-----------------------|-----------------------|
| B [GPa]              | 122           |                       | 142                   |
| $\Delta H_m$ [KJ/Kg] | 74            | 246                   | 205                   |
| $c_v$ [J/kg-K]       | 393           |                       | 367                   |
| $c_p$ [J/Kg-K]       |               | 413                   | 386                   |
| $\alpha_T$ (293K)    |               | $5.1 \times 10^{-5}$  | $4.85 \times 10^{-5}$ |
| $\alpha_T$ (1000K)   |               | $10.4 \times 10^{-5}$ | $6.72 \times 10^{-5}$ |
| $\Delta V_m$         |               | 11%                   | 5.17%                 |
| $T_m$ [K]            | 1600          | 1480                  | 1358                  |

Table 5-6: Derived Thermodynamic Properties

calculated and experimental results. The latent heat of melting for Dagens' potential is less than half of the experimental value. The latent heat of melting calculated using modified Morse potential is more reasonable and is about twenty-five percent larger than the experimental result, but there are appreciable discrepancies in the values of the bulk thermal expansion coefficient at 1000K and the volume change on melting. It is concluded that the both potentials appear to be fairly good at low temperatures, but are not accurate at high temperatures.

All of the properties calculated in this Section can be used to determine whether or not the system is in the solid or liquid phase (except for the volume and pressure in constant-volume and constant-pressure simulations, respectively). In plots of the thermodynamic properties such as those in Figures 5-3 to 5-6, the data will fall into two separate curves if both liquid and solid phases were simulated, and if no phase transitions occurred while property averages were calculated. If property averages were calculated during the phase transition, the average value will fall between the solid and liquid curves. In the solid phase, atoms vibrate about their perfect lattice positions and remain near those positions as long as the temperature is not too close to melting. Consequently, the mean-square displacement (MSD) will increase from its initial value of zero and then fluctuate about an average value which can be uniquely associated with temperature. In a liquid, there are no equilibrium positions and atoms are able to diffuse throughout the volume, and the MSD continuously increases (the increase is linear if the motion is diffusive). Hence, the time evolution of the MSD indicates the phase of the system. All the properties discussed thus far can only be used to determine the phase of the system when values of the property are compared between separate runs at different temperatures or from the behavior of the property over time during a

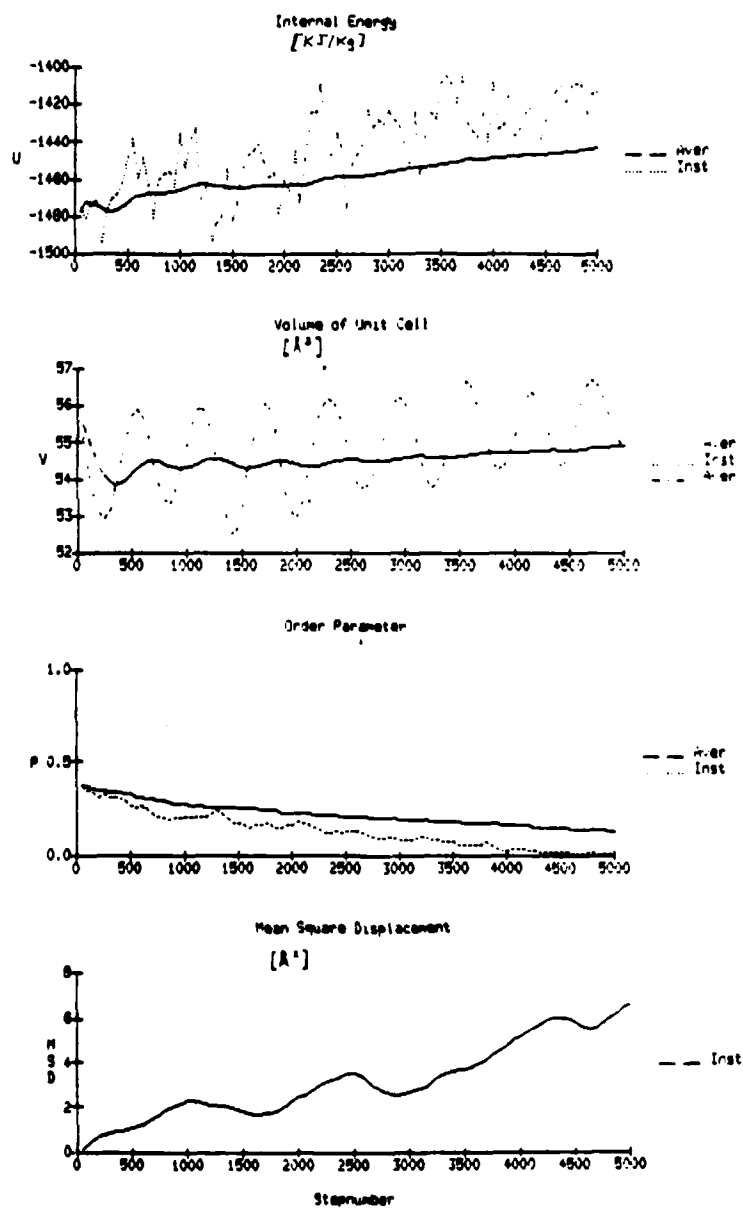
simulation. A property which can indicate the phase of the system from a single instantaneous value is the order parameter. As noted above, the order parameter defined by equation (3.20) has a value of 1 for a perfectly ordered system and 0 if the system is completely disordered. Although the order parameter fluctuates during a simulation, the fluctuations are small enough such that a single value can often indicate the state of the system.

An example of how some of these properties can be used to monitor a phase transition is shown in Figure 5-8. The internal energy  $U$  increases during the run as the system leaves the low potential energy solid state and enters the higher energy liquid phase. The volume also increases since the liquid is less dense than the solid. The order parameter decreases during the phase change; note that the fluctuations in the order parameter are much less than the fluctuations in the internal energy and the volume, and that it decreases in a smoother fashion. The MSD increases over the length of the run although it also fluctuates a great deal. The advantage of having all of these properties available is that they can be used to independently confirm one another. For example, the decrease at early times in the order parameter is matched by the increase in the internal energy.

Even though one has all of these properties available to determine the phase of the system, the melting point of

**Figure 5-8: Properties During a Modified Morse  
Potential Melting Transition**

(This is Run 38 in Tables 5-4 and 5-5)





a potential is difficult to estimate accurately for a number of reasons. One problem is that the velocity scaling method discussed in Section 3.3 generates an ensemble which has an average temperature within about five percent of the desired temperature. At 1400K this means that the simulation temperature can be plus or minus 70K of the desired temperature. Hence, it is difficult to accurately preset the temperature of the simulation near the melting point of the metals. Techniques have been devised to overcome this problem<sup>27</sup>, but unfortunately a more serious difficulty exists.

Ideally, the best way to determine the melting point of the a system is to calculate the free energy of the system in the solid and liquid states at different temperatures. The intersection of the two curves is the<sup>61</sup> thermodynamic melting point. Unfortunately, however, the free energy is very difficult to calculate. Instead of calculating the free energy, a more commonly used method is to initialize the simulation at a given temperature and phase and then observe whether or not the system stays in that phase. If one waits long enough, the system will eventually enter the phase with the lowest free energy. Unfortunately, it may take a long time for the transition to nucleate, and the information available to us from simulation cannot tell us how long this will take. (Note that the transition shown in Figure 5-8 took

over 3000 time steps). As one moves away from the thermodynamic melting point, however, the activation energy for nucleation of the transition from a higher to a lower free energy phase decreases and the melting transition can occur within reasonable simulation times of a few picoseconds. Consequently, if one continues to raise the temperature of the system, at some point melting will occur. The melting point under these circumstances is called the structural melting point, and the temperature at which it occurs is higher than the thermodynamic melting temperature<sup>61</sup>.

Keeping these difficulties in mind, the melting points for Dagens potential for the different simulation volumes are estimated to be 2000K, 1850K, and 1300K at  $V_0$ ,  $V_s$ , and  $V_1$ , respectively. The value of the melting point corresponding to ambient pressure is taken to be the average of the two latter values, i.e., about 1600K. The melting point of the modified-Morse potential (at ambient pressure) was found to be about 1480K. All of these values are larger than the experimental melting temperature of copper at 1357K.

### 5.3 Vibrational Properties

The vibrational properties of a solid can be calculated from the positions and velocities of the atoms at discrete times during the simulation. Although it is possible to calculate the vibrational frequency spectrum directly from the velocities<sup>62</sup>, the usual method is to calculate the velocity autocorrelation function (VACF) and then take its Fourier transform. The VACF is given by

$$\text{VACF}(t) = \frac{1}{N} \left\langle \sum_i \frac{\underline{v}_i(0) \cdot \underline{v}_i(t)}{\underline{v}_i(0) \cdot \underline{v}_i(0)} \right\rangle \quad (5.5)$$

where  $\underline{v}_i(t)$  is the velocity of atom  $i$  at time  $t$ . The  $\langle \rangle$  brackets indicate a time average which emphasizes that it is necessary (especially for the number of atoms used in these simulations) to average over many VACF values calculated for a particular time  $t$ . As the simulation proceeds, the time "origins" denoted by  $t_0$  created periodically. The atom velocities and their dot product are saved for each origin. To calculate the VACF at a particular time  $t'$ , we wait until that number of time steps has passed a given origin  $n$ , i.e., until  $t - t_n = t'$ , and calculate the numerator of (5.5). In this manner each origin contributes one value to the average for a given time  $t'$  of the VACF. For the results that follow, 100 origins separated by 30 time steps were used, which gave

contributions to each time  $t$  of the VACF. The VACF for the pseudopotential and the modified Morse potentials at about 298K are shown in Figure 5-9. The pseudopotential VACF was calculated at  $V_0$ ; the modified Morse VACF at ambient pressure.

The Fourier transform of the VACF yields the vibrational frequency spectrum of the atoms. The vibrational spectra for the two potentials are plotted in Figure 5-10. This plot also shows experimentally observed spectra for copper at 49K and 298K<sup>63</sup>. The spectrum for the pseudopotential match the experimental observations fairly well, giving good agreement at the positions of the peaks and valleys. This confirms the conclusions of Upadhyaya et al, who found that the phonon spectra for the pseudopotential were in excellent agreement with experimental data<sup>17</sup>. The spectrum of the modified Morse potential does not match quite as well and slightly misses the high frequency peak. It is noted that the system volume using the modified Morse potential is very close to the volume of real copper so that this cannot be the source of the discrepancy.

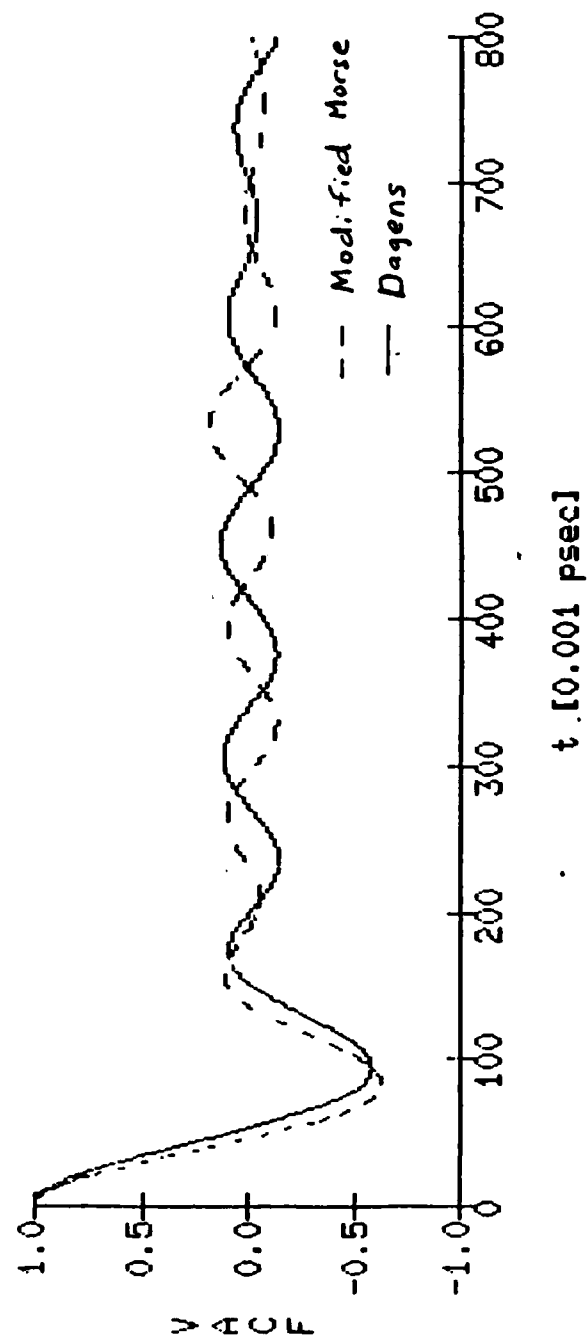
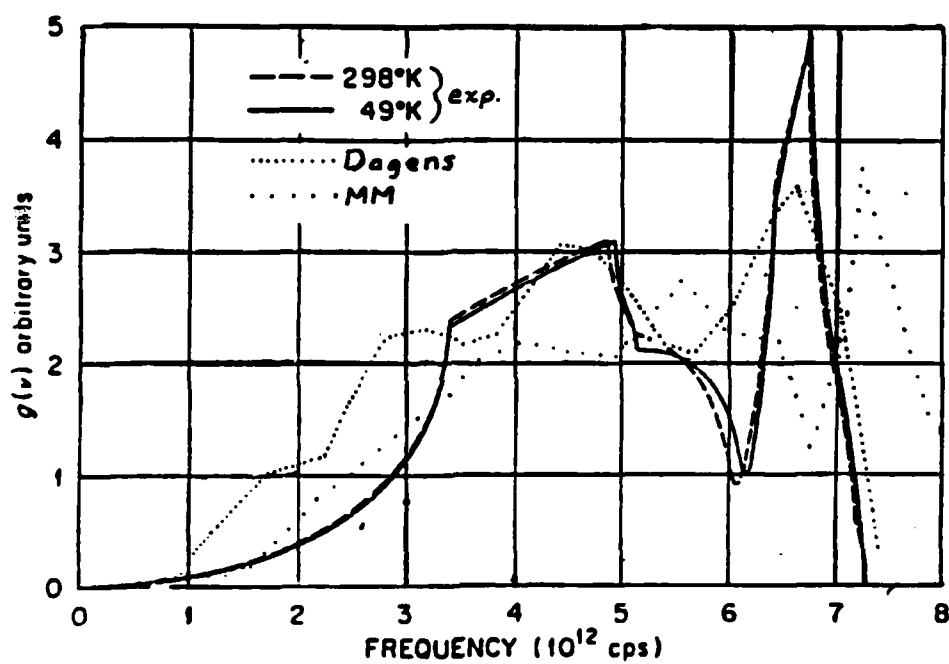


Figure 5-9: VACF at  $\sim 298K$

Figure 5-10: Frequency Spectra at ~298K



#### 5.4 Discussion

As indicated in Table 5-6, both potentials appear to perform better at low temperatures and have difficulty in giving satisfactory high temperature properties near melting. The reason for the excellent low temperature behavior is probably that both potentials, and especially Dagens' potential, reproduce the experimentally calculated phonon spectra fairly well, as indicated in Figure 5-10. Of course, Dagens' potential has the additional justification that it is derived using the pseudopotential method and is closer to a first principles calculation. Because of this, it is probably better to use Dagens' potential in the low temperature regime. It is noted once again, however, that the Dagens' interatomic potential is incomplete for these types of calculations without the structure independent contribution.

Although the structure-independent contribution to Dagens' potential was not available for these calculations, it is possible to speculate as to whether or not it could make a difference. If Dagens' potential is assumed to be correct at a given volume, the volume derivative of the structure independent energy is given by the difference in the simulation pressure and the experimental pressure of copper under the same conditions. This value, which can be called a pressure correction to

the simulation pressure, should be valid over all temperatures for the given volume if the potential is correct. At  $V_0$ , the volume of real copper at ambient temperature and pressure, the simulation pressure is about 23.6 GPa and hence the pressure correction at this volume is -23.6 GPa. We can calculate the pressure of real copper at ambient temperature at the volume  $V_s$  by using the bulk modulus of real copper; this yields a pressure of -9.8 GPa since copper must be expanded to this volume. The simulation at this volume and temperature gives a pressure of 15 GPa; the pressure correction at volume  $V_s$  is thus  $-9.8 - 15 = -25$  GPa. We can also calculate the pressure correction at  $V_s$  at the melting temperature, since by definition of  $V_s$  real copper is at 0 GPa. From Figure 5-5 we find that the simulation pressure at the melting point of real copper, 1357K, is about 20 GPa. This gives a volume dependent contribution to the potential of -20 GPa, which differs from the estimate at ambient temperature of -25 GPa by 20 percent. Noting that the bulk modulus is very sensitive to pressures of this magnitude since it is calculated from a difference of two pressures, it is concluded that no volume dependent contribution could make the pseudopotential calculations match the experimental results.

The overall evaluation of the thermodynamic calculations of Dagens' potential is that the potential



appears to work well at low temperatures (less than ambient) but is not very successful at high temperatures. It is interesting to note that preliminary thermodynamic calculations for Dagens' silver potential<sup>15</sup>, which are discussed in Chapter 8, lead to the same conclusion. Although the silver appears to be successful in matching the melting temperature of real silver, it does not do well with other high temperature properties. On the other hand, the low temperature properties calculated by the silver potential are even better than the copper potential results.

Chapter 6  
Small Vacancy Cluster Migration

6.1 Introduction

The primary factors which control the concentration and migration of defect clusters are their binding and migration energies. In general, the equilibrium concentration and the migration (or diffusion) rate of a defect are described by an Arrhenius relationship with temperature. For example, the diffusion coefficient for a defect can be expressed as

$$D(T) = D_0 \exp(-E^m/kT) \quad (6.1)$$

where  $k$  is the Boltzmann constant,  $E^m$  is the migration energy for the defect, and  $D_0$  is a pre-exponential factor which is independent of or only weakly dependent on temperature. Since the defect energies appear as exponents, they overshadow any minor temperature dependence of the pre-exponential terms.

As discussed in Chapter 4, molecular statics can be used to calculate the formation, binding and migration energies of defects in a material, provided a suitable

interatomic potential can be found. The purpose of this Chapter is to present the results of molecular statics calculations of defect energies using Dagens' copper potential<sup>15</sup> discussed in Chapter 2. In the following section the results of migration energy calculations of the tri- and tetravacancies in copper are presented. This work extends the results given by Lam et al<sup>1, 3</sup> for small vacancy defects in copper. A common experimental method which has been used to determine small defect energies is isochronal annealing<sup>4</sup>. To make the comparisons with the annealing experiments less ambiguous, the experiments are modeled with rate equations using the defect model based on the migration and binding energies calculated in this work and by Lam<sup>1, 3</sup>. The annealing simulations are discussed in detail in Section 3. In the final section, the molecular statics results are compared to previous computer calculations and experimental data, and the applicability of the defect model for copper is critically discussed.

## 6.2 Migration Energy Calculations

As was discussed in Section 4.5, the migration energy between two vacancy defects which can transform from one to another by a single vacancy jump is given by the magnitude of the energy barrier which must be overcome during the jump. Many different migration energies can be

associated with a vacancy cluster of a given size since clusters have many different metastable configurations. Most of these migrations are of no practical interest, since a migration mechanism will be unlikely to occur if it involves configurations which have large formation energies compared to other configurations, or if other lower energy migration mechanisms exist. Consequently, one is interested in the minimum energy configurations of a cluster and in the low energy migration mechanisms of these configurations. The migration energy  $E_{nV}^m$  of a  $n$ -vacancy cluster is specifically defined as the energy barrier of the lowest energy mechanism which can move the the lowest energy configuration of the cluster from one position in a perfect, infinite crystal to any other position. A perfect, infinite crystal is specified to eliminate interactions with other defects and surfaces, which are not considered here. It is also important to specify that the mechanism be able to move the defect throughout the crystal, since some mechanisms may only be able to move the defect within a limited region. The strategy used to calculate the migration energy of a cluster is to calculate the binding energies of the cluster configurations to determine the most stable configuration. One then calculates the energy of each migration mechanism which can move the cluster from one position to another in a crystal.

All of the defect energy calculations were done using the techniques discussed in Section 4.5. The system consisted of a 500 atom lattice from which the necessary number of vacancies were removed. Dagens' copper potential was employed with a potential cutoff radius of 8.5515 Å and a Duesbury factor<sup>45</sup> of  $0.25a^{-1}$ , as discussed in Section 2.3. Lam et al<sup>1, 3</sup> have already calculated many of the energies of small vacancy clusters in copper using Dagens' potential, but with larger systems (864 to 2048 atoms) and longer cutoff radii. To insure that system used in this work was sufficiently large and the potential cutoff radius was sufficiently long, the small vacancy defect energies already calculated by Lam et al<sup>1, 3</sup> were calculated with the system used in this work. Given the relatively large cutoff radius and system size, and the use of the Duesbury factor, the results of this work should correspond closely to those of Lam et al<sup>1, 3</sup>. In Table 6-1 it is shown the difference in the calculations of this work and those of Lam<sup>1, 3</sup> less than two percent.

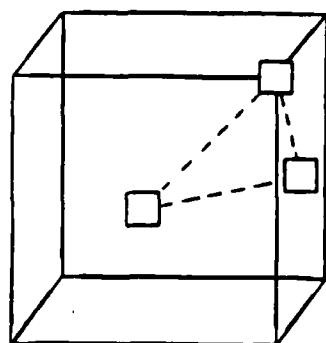
In Figure 6-1 a number of copper tri- and tetravacancy configurations are shown. Although many configurations are possible, these configurations are of particular interest because of the role they play in the migration of the clusters discussed below. The binding energies of these configurations are shown in Table 6-2.

| <u>Energy</u> | <u>Lam et al</u> | <u>This Work</u> |
|---------------|------------------|------------------|
| m             |                  |                  |
| E             | 0.82             | 0.81             |
| 1V            |                  |                  |
| b             |                  |                  |
| E             | 0.05             | 0.05             |
| 2V            |                  |                  |
| m             |                  |                  |
| E             | 0.55             | 0.55             |
| 2V            |                  |                  |
| b             |                  |                  |
| E             | 0.15             | 0.15             |
| 3V            |                  |                  |
| b             |                  |                  |
| E             | 0.28             | 0.28             |
| 4V            |                  |                  |

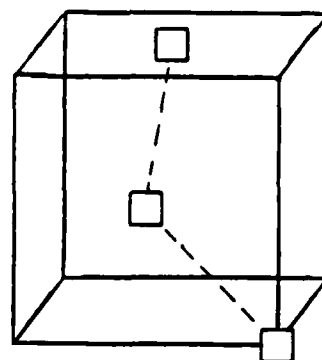
(Energies in ev)

Table 6-1: Comparison of Copper Results with  
<sup>1, 3</sup>  
Lam et al

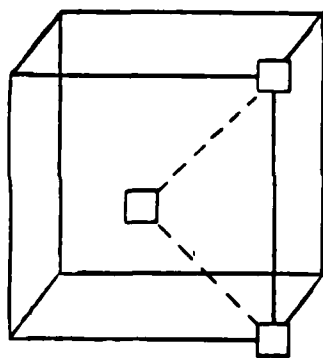
**Figure 6-1: Vacancy Cluster Configurations in Copper**



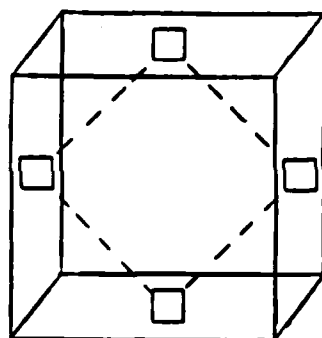
**3A**



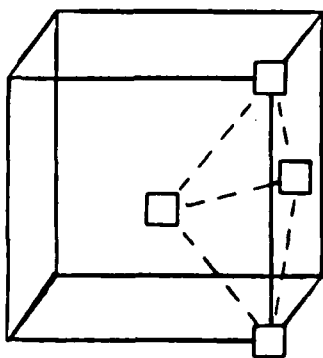
**3B**



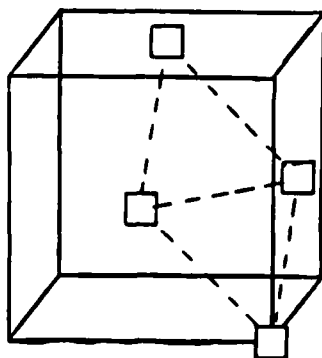
**3C**



**4A**



**4B**



**4C**

| <u>Cluster</u> | <u>Binding Energy (ev)</u> |
|----------------|----------------------------|
| 3A             | 0.155                      |
| 3B             | 0.109                      |
| 3C             | 0.095                      |
| 4A             | 0.285                      |
| 4B             | 0.268                      |
| 4C             | 0.268                      |

Table 6-2: Binding Energies of Tri-  
and Tetravacancies in Copper

In Figure 6-2 some migration mechanisms for the trivacancy are shown. In this Figure the primed and unprimed states indicate the same configurations but different positions or orientations. The first migration mechanism, indicated by the 3A->3A' transition, results in movement of the trivacancy to a different face of an fcc tetrahedral cell. Although the trivacancy can reorient itself within the tetrahedral cell, it is not possible for the trivacancy to escape the cell through this mechanism and thus it is not considered a true migration mechanism<sup>64</sup>. The other two mechanisms in Figure 6-2, 3A->3B->3A' and 3A->3C->3A', do result in migration because through them the trivacancy is not limited to a small region of the crystal. In these cases, the trivacancy moves through an intermediate metastable configuration before returning to the stable configuration at a new site. In Figure 6-3 configuration energy versus reaction coordinate is plotted. The plot for the reorientation mechanism is interesting because it



indicates that there is an intermediate configuration analagous to the stable trivacancy for the calculated for silver by Lam et al<sup>3</sup>. The plots for the two true migration mechanisms yield no surprises and show that the migration which passes through configuration 3B is energetically favored and  $E_{3V}^m = 0.56$  ev, which is about the same as the divacancy migration energy.

The migration mechanism for the copper tetravacancy is shown in Figure 6-4. The tetravacancy passes through three intermediate configurations to migrate, which can be written  $4A \rightarrow 4B \rightarrow 4C \rightarrow 4B' \rightarrow 4A'$ . The reaction coordinate plots in Figure 6-5 show that the migration from configuration 4A to 4B has the highest energy barrier, and hence it controls the energy for the overall migration. Thus,  $E_{4V}^m = 0.38$  ev, which is lower than the calculated migration energies of single, di-, and trivacancies.

### 6.3 Annealing Kinetics

The results of the calculations of the defect energies in copper are summarized in Table 6-3. An experimental method which has been used to determine these values in metals is isochronal annealing<sup>4</sup>. As Balluffi<sup>4</sup> points out, however, annealing experiments are not always easy to interpret, especially when complicated processes are involved. In copper, for example, only the single vacancy migration energy is known although the divacancy

**Figure 6-2: Copper Trivacancy Migration Mechanisms**

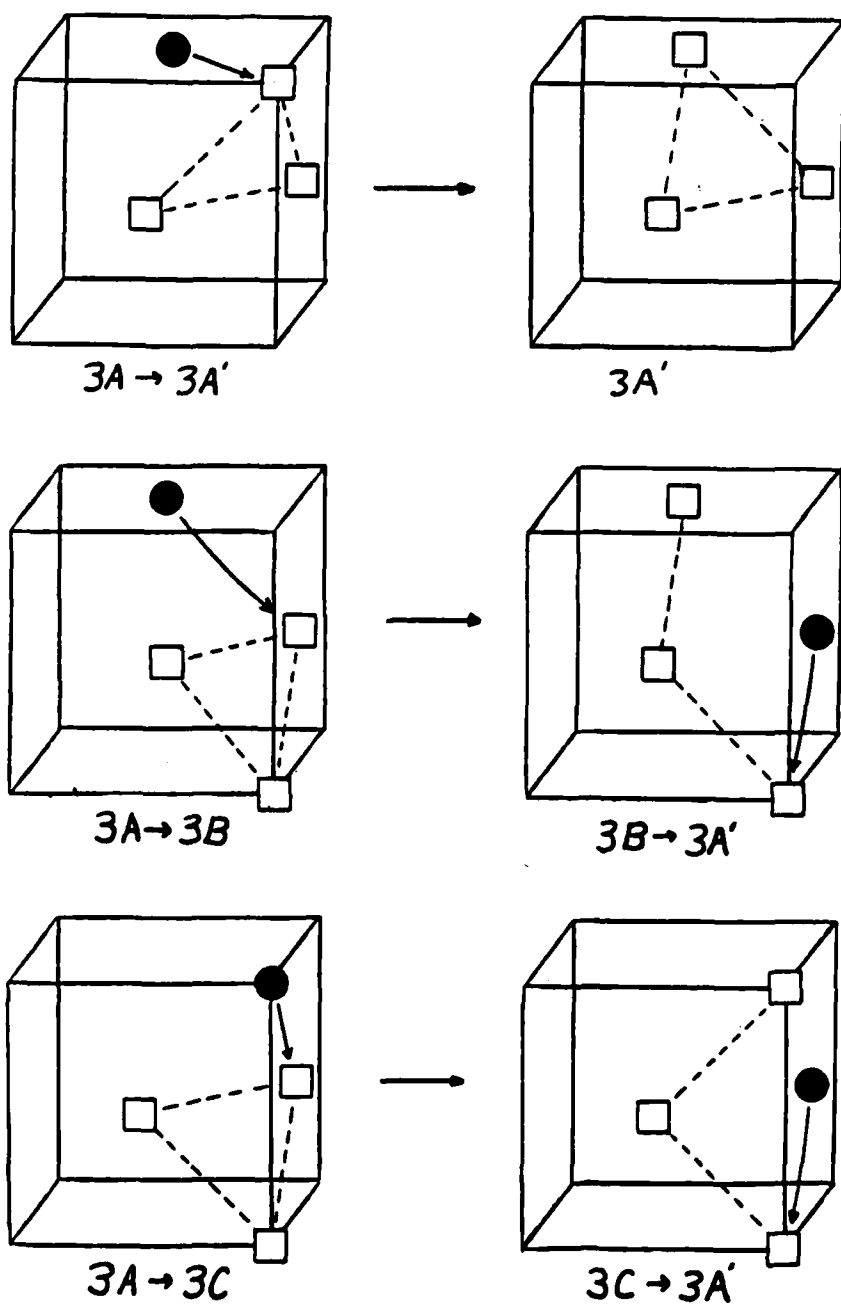


**Figure 6-3: Copper Trivacancy Migration Barriers**

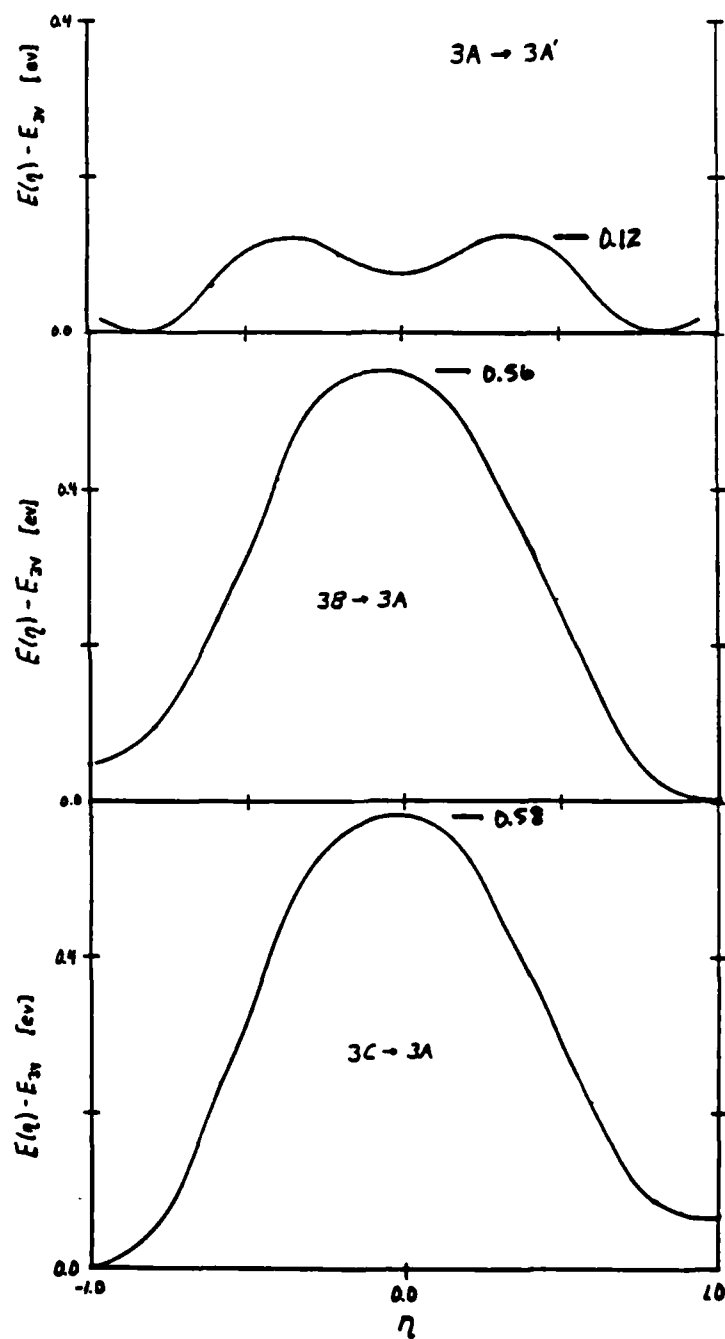


Figure 6-4: Copper Tetravacancy Migration Mechanism

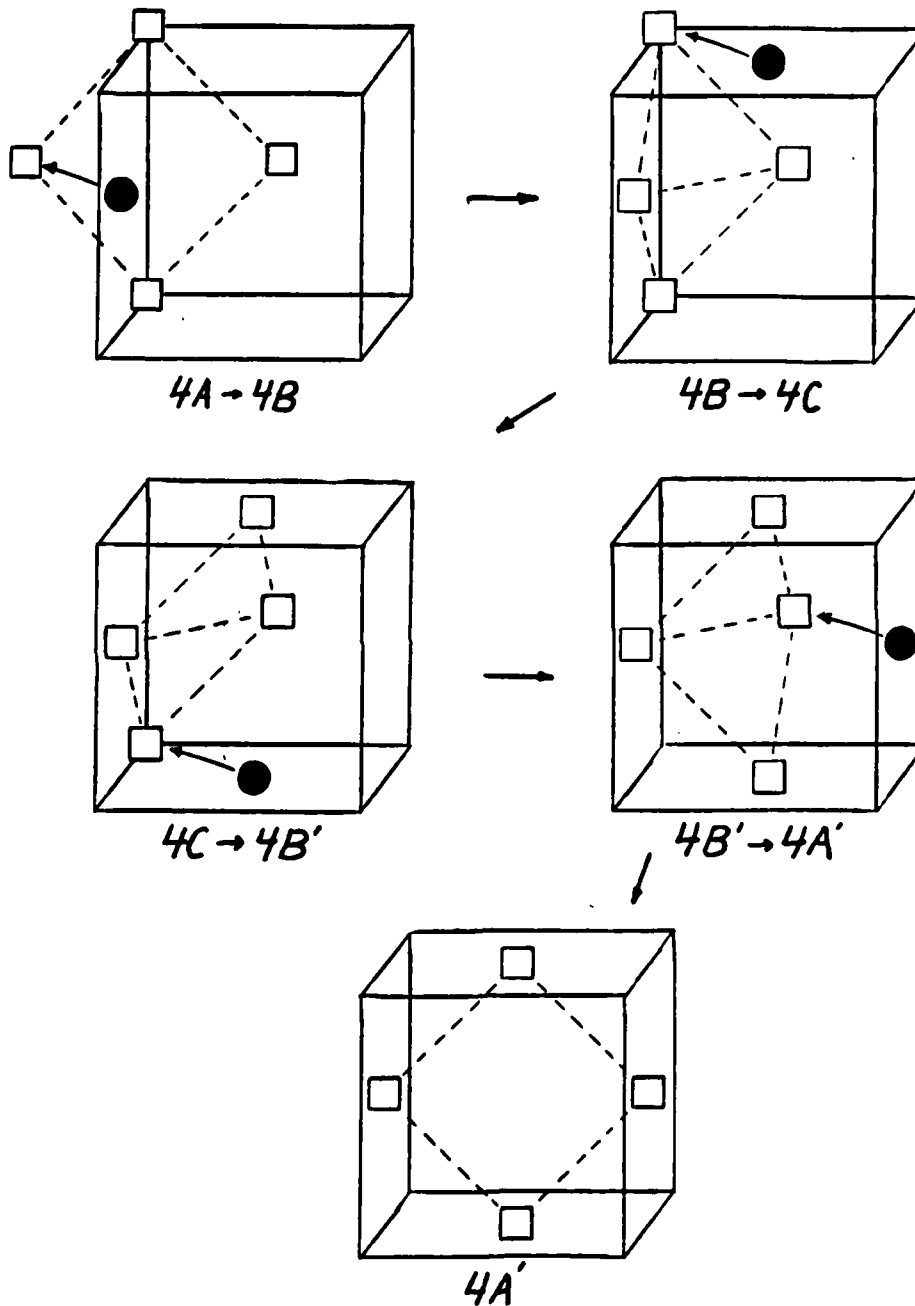
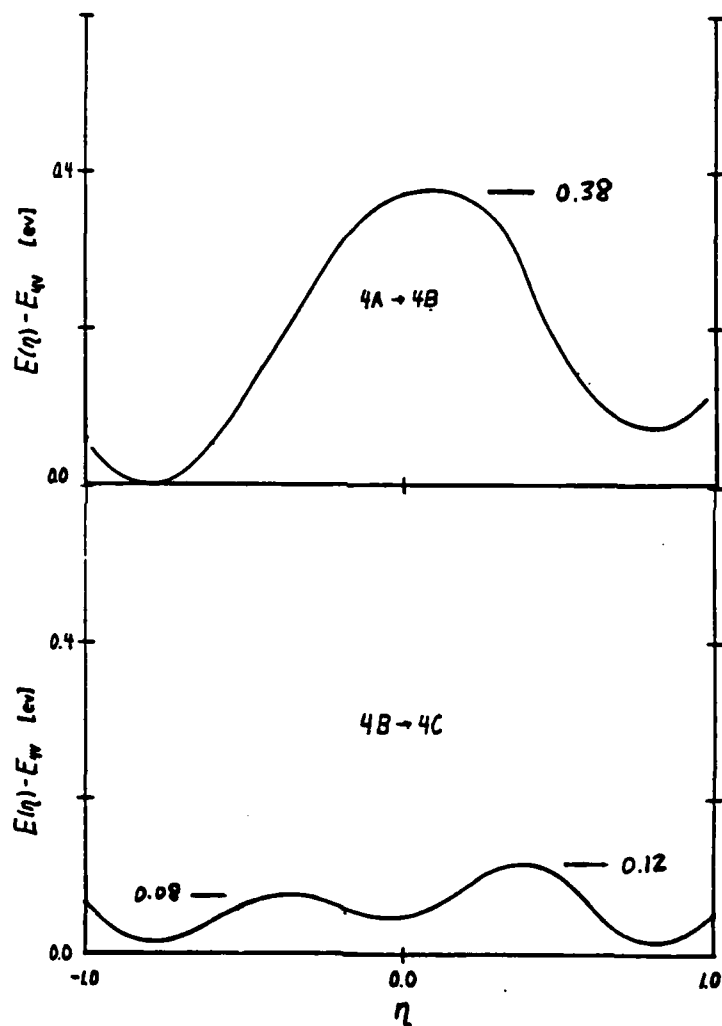


Figure 6-5: Copper Tetravacancy Migration Barriers



is believed to be more mobile<sup>4, 65</sup>. Direct comparison of the defect energies of large clusters with experimental values is hence not possible and another approach is necessary. The tri- and tetravacancy migration energies calculated in the previous section complete the set of binding and migration energies of vacancy clusters with one to four vacancies calculated by Lam et al<sup>1, 3</sup>. Although one cannot practically simulate annealing using molecular statics and dynamics, the defect energies can be used in other theoretical and computational methods which are capable of doing modeling annealing. In particular, rate equations<sup>66</sup> are very useful for modeling of large systems in which the defect distribution is homogeneous and is often used to interpret annealing results (for examples in particular metals, see De Jong and Koehler<sup>64</sup>, Seeger and Frank<sup>67</sup>, and Collins et al<sup>68</sup>). This gives one the ability to model defect annealing in copper and compare the results with experimental observations. In this section, a general background will first be given on annealing experiments, followed by the method and results of modeling the experiments using the defect energies calculated by molecular statics and dynamics.

The initial step of an annealing experiment is the introduction of defects into the material using, for example, electron-irradiation or quenching. The basic

| <u>Defect</u>  | <u>Energy (eV)</u><br><u>Binding</u> | <u>Migration</u> |
|----------------|--------------------------------------|------------------|
| V <sub>1</sub> |                                      | 0.82*            |
| V <sub>2</sub> | 0.05*                                | 0.55*            |
| V <sub>3</sub> | 0.15*                                | 0.56             |
| V <sub>4</sub> | 0.28*                                | 0.38             |

Table 6-3: Binding and Migration Energies of Small Vacancy Clusters in Copper

\*  
( from Lam et al<sup>1, 3</sup> )

idea behind annealing experiments is then to activate as few different types of defects at a time as possible by systematically raising the temperature of the specimen. Electron-irradiation creates single vacancies and interstitials in the material; at low temperatures the difference in the migration energies of vacancies and interstitials allows the latter to migrate while the former is effectively immobile. The general temperature regimes over which each type of defect anneals are called Stages. Within the one-interstitial annealing model<sup>69</sup>, as the temperature of the material is raised, the interstitials recombine with vacancies, anneal at sinks, and form interstitial clusters during Stage I. In Stage II, interstitial clusters coarsen and some interstitial

reactions with impurities may occur. In Stage III, which occurs at about 280K in copper<sup>4</sup>, there are no single interstitials and the remaining single vacancies begin to migrate. Similar to interstitials, the vacancies can form vacancy clusters and annihilate at the interstitial clusters formed during Stages I and II and at extended sinks. At higher temperatures, two additional Stages are found in most metals in which the vacancy clusters coarsen and eventually all of the original damage is annealed.

Another commonly used method of introducing defects into a material is quenching. The material is taken to a high temperature, near melting, and the relatively low formation energy of vacancies allows an appreciable number of vacancies to exist in equilibrium. The sample is then quenched to a very low temperature at which the vacancies are supersaturated but also immobile. The temperature of the specimen is then systematically increased as in electron-irradiation case, although of course we do not expect to observe Stages I and II since no interstitials are present. The advantage of quenching over electron-irradiation is that only vacancies are formed in quenching because the formation energy of interstitials is too high for them to exist at an appreciable concentration even at high temperatures. On the other hand, during the quench it is possible for vacancies to form clusters, which may make it difficult to interpret the experimental results.



The defect concentration is usually monitored using some macroscopic material property  $P$  (traditionally this has often been electrical resistivity<sup>4</sup>), and analysis of the changing concentration with time and temperature enables one to calculate the effective activation energy for the annealing process. If annealing is controlled by a single activation energy  $E^{act}$ , the annealing rate  $R$  is given by

$$R(t, T) = \frac{dP(T)}{dt} = R^0(t) \exp(-E^{act}/kT) \quad (6.2)$$

where  $t$  is time.  $R^0(t)$  depends on the vacancy defect concentrations at time  $t$ , but is independent of temperature. One method of determining the activation energy  $E^{act}$  from the measured annealing rate, called the change-of-slope method<sup>66</sup>, is to instantaneously change the sample temperature. Let  $T_1$  and  $T_2$  be the sample temperatures just before and just after an instantaneous temperature change, respectively, and let  $R_1$  and  $R_2$  be the annealing rates just before and after this change. Then

$$R_1 = R^0 \exp(-E^{act}/kT_1) \quad (6.3)$$

$$R_2 = R^0 \exp(-E^{act}/kT_2) \quad (6.4)$$

Since the temperature change is instantaneous,  $R_1^0 = R_2^0$  and we can solve equations (6.3) and (6.4) for  $E^{act}$  to get

$$E^{act} = \frac{-k \ln(R_1^0 / R_2^0)}{1/T_1 - 1/T_2} \quad (6.5)$$

If a single process (say single vacancy migration) is rate-limiting, then a well-defined activation energy  $E^{act}$  can be assigned to that process (providing the process itself can be identified). In general, however, various processes can take place simultaneously; the problem then is identifying the rate-limiting process or processes so that an effective activation energy can be assigned.

An annealing experiment can be modeled by solving a set of rate equations which describe the possible reactions in the sample. Let  $V_n$  denote an  $n$ -vacancy cluster where  $n = 1, \dots, 5$ ,  $VC$  denote all larger vacancy clusters, and  $S$  denote sinks. The reactions which are included in this work are then given in Table 6-4. Some of the possible cluster-cluster reactions have not been included in anticipation of the results in which they are not significant. The sinks  $S$  in Table 6-4 can represent, in the following analyses, both interstitial loops after electron-irradiation and the low concentration of sinks present after quenching. Although it is possible for appreciable concentrations of large vacancy clusters to

form, it is not practically possible to model all sizes of clusters. In the model in Table 6-4, all clusters with six or more vacancies are represented by VC. Although the size of the largest cluster which is explicitly modeled in Table 6-4 could have been increased to a larger value, the information about these larger clusters is limited. The rate constants for their reactions would have to be assumed without specific information about the interaction radii between the large clusters and other defects. The fractions in the VC reactions are an attempt to account for the reduced contribution a vacancy makes to the macroscopic property  $P$  when it is a member of a large cluster<sup>70</sup>. The justification for these fractional values will be discussed when the macroscopic property  $P$  is defined below.

A set of rate equations which describe the reactions in Table 6-4 can now be defined. Let the concentration of a vacancy cluster  $V_x$  be represented by  $c_x$ , and the sink concentration by  $c_s$ . The rate equations describing the reactions in Table 6-4 are then

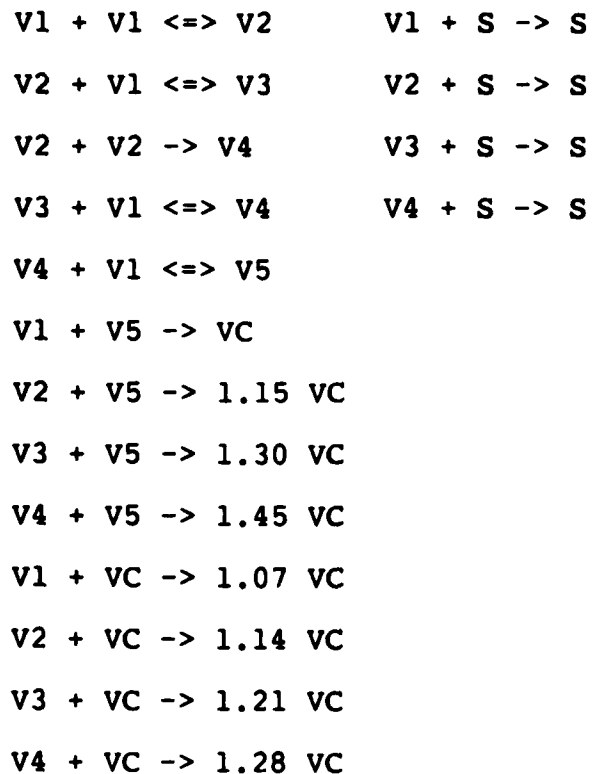


**Table 6-4: Reactions of Vacancy Defects  
with one another and with Internal  
Sinks**

$$\begin{aligned}
 \dot{c}_1 = & -2a_{11}^2 c_{11}^2 - a_{12} c_{11} c_{12} - a_{13} c_{11} c_{13} - \\
 & a_{14} c_{11} c_{14} - a_{15} c_{11} c_{15} - a_{1C} c_{11} c_C + \\
 & 2b_{22} c_{22} + b_{33} c_{33} - \\
 & a_{S1} c_{S1} c_1
 \end{aligned}$$

(6.6)

$$\begin{aligned} \dot{c}_2 = & a_{11}^2 c_1^2 - a_{12}^2 c_1 c_2 - 2a_{22}^2 c_2^2 - \\ & a_{52}^2 c_2 c_5 - a_{C2}^2 c_2 c_C - a_{S2}^2 c_2 c_S - \\ & b_{22}^2 c_2 + b_{33}^2 c_3 \end{aligned} \quad (6.7)$$

$$\begin{aligned} \dot{c}_3 = & a_{12}^2 c_1 c_2 - a_{13}^2 c_1 c_3 - a_{53}^2 c_3 c_5 - \\ & a_{C3}^2 c_3 c_C - a_{S3}^2 c_3 c_S - \\ & b_{33}^2 c_3 + b_{44}^2 c_4 \end{aligned} \quad (6.8)$$

$$\begin{aligned} \dot{c}_4 = & a_{13}^2 c_1 c_3 + a_{22}^2 c_2^2 - a_{14}^2 c_1 c_4 - \\ & a_{54}^2 c_4 c_5 - a_{C4}^2 c_4 c_C - a_{S4}^2 c_4 c_S - \\ & b_{44}^2 c_4 + b_{55}^2 c_5 \end{aligned} \quad (6.9)$$

$$\begin{aligned} \dot{c}_5 = & a_{41}^2 c_1 c_4 - a_{51}^2 c_1 c_5 - a_{52}^2 c_2 c_5 - \\ & a_{53}^2 c_3 c_5 - a_{54}^2 c_4 c_5 - \\ & b_{55}^2 c_5 \end{aligned} \quad (6.10)$$

$$\begin{aligned} \dot{c}_C = & a_{51} c_1 c_4 + 1.15 a_{52} c_2 c_5 + 1.3 a_{53} c_3 c_5 + \\ & 1.45 a_{54} c_4 c_5 + 0.07 a_{C1} c_1 c_C + \\ & 0.14 a_{C2} c_2 c_C + 0.14 a_{C3} c_3 c_C + \\ & 0.28 a_{C4} c_4 c_C \end{aligned} \quad (6.11)$$

The rate constants  $a_{xy}$  are for association reactions between defects represented by the concentrations  $c_y$  and  $c_x$ . The second subscript denotes the more mobile component of the two defects. The rate constants  $b_x$  are for the breakup or dissociation of the clusters represented by concentration  $c_x$  into two smaller clusters.

The rate constants are selected following Johnson<sup>70</sup>. They consist of the following three parts: an attempt frequency  $f_y$ ; a geometrical factor  $g_x$ ; and an energy  $E_y$  which determines the temperature dependence of the rate constant. The rate constants are then

$$a_{xy} = f_y g_x \exp(-E_x / kT) \quad (6.12)$$

$$b_x = f_{b,x} g_{b,x} \exp(-E_{b,x} / kT) \quad (6.13)$$

where the subscript 'b' indicates a factor of a breakup reaction. The values used in this work are shown in Table 6-5. The main uncertainties are in the geometrical and frequency factors, since these quantities are difficult to

experimentally determine and have not been actually calculated here. A range of values were tested for these factors and, confirming Johnson's conclusions<sup>70</sup>, we found that the results were not very sensitive to them. The energies are the main quantities of interest here since these were calculated in the previous section using molecular statics, and are the values which are normally determined in annealing experiments. The migration energies are taken directly from the molecular statics results. The "breakup" or dissociation energy of a cluster into two smaller clusters is calculated by adding the migration energy of the most mobile component to the difference in binding energies of the original cluster and the binding energies of the components. For example, the dissociation energy of a trivacancy into a single and divacancy, where the divacancy is more mobile than the single vacancy, is given by

$$E_{3V}^{brk} = (E_{3V}^b - E_{2V}^b) + E_{2V}^m \quad (6.14)$$

As pointed out above, the defect concentrations are usually not directly measured in an annealing experiment, but instead some macroscopic property  $P$  which is a function of the concentrations is measured.  $P$  has traditionally been the electrical resistivity. It is believed that the contribution of a small vacancy cluster

| <u>Defect</u> | <u>f</u>           | <u>E [ev]</u> |            | <u>g</u>   |            |
|---------------|--------------------|---------------|------------|------------|------------|
|               |                    | <u>mig</u>    | <u>brk</u> | <u>mig</u> | <u>brk</u> |
| $V_1$         | $1 \times 10^{14}$ | 0.82          |            | 12         | 12         |
| $V_2$         | $2 \times 10^{13}$ | 0.55          | 0.87       | 84         | 14         |
| $V_3$         | $4 \times 10^{12}$ | 0.56          | 0.65       | 144        | 14         |
| $V_4$         | $4 \times 10^{12}$ | 0.39          | 0.69       | 164        | 14         |
| $V_5$         | $4 \times 10^{12}$ |               | 0.76       | 180        | 14         |
| $V_C$         |                    |               |            | 180        | 14         |
| S             |                    |               |            | 12         |            |

Table 6-5: Values of the Physical Parameters  
Used in Equations (6.12) and (6.13)

to the electrical resistivity is approximately proportional to the number of vacancies it contains, although it is also known the contribution per vacancy decreases as the cluster grows<sup>71</sup>. In this model the macroscopic property  $P$  is a simply a linear combination of the defect concentrations given by

$$P = \sum_{i=1}^5 i c_i + 6c_C \quad (6.15)$$



The decrease in contribution for larger vacancies is accounted for by the fractional terms in the  $V_C$  reactions in Table 6-4. Although this model is no doubt much simpler than what occurs in real metals, the model does predict the correct remaining resistivity after annealing of a quenched sample.

It is difficult to simplify the equations (6.6) to (6.11) without introducing unrealistic assumptions. Because of this, it was decided to solve the equations (6.6) to (6.11) numerically. The parameters which were varied between different runs were the initial single vacancy concentration  $c_1(0)$  and the sink concentration  $c_s$ . The ranges of these values covers the spectrum of standard annealing experiments.

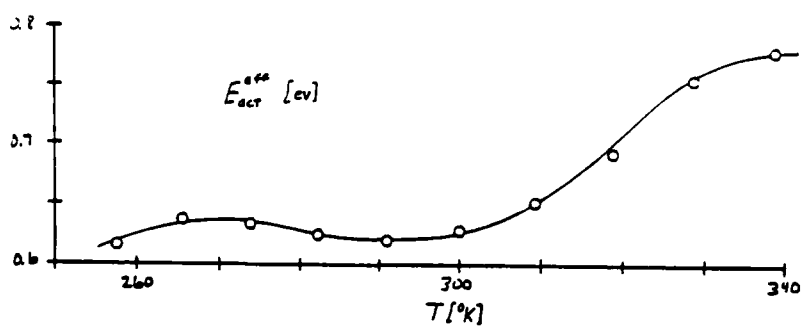
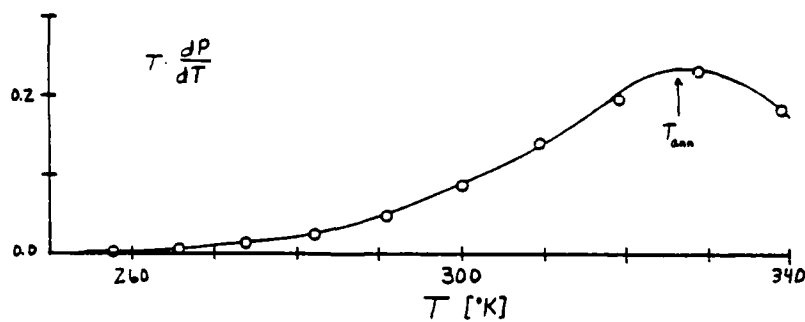
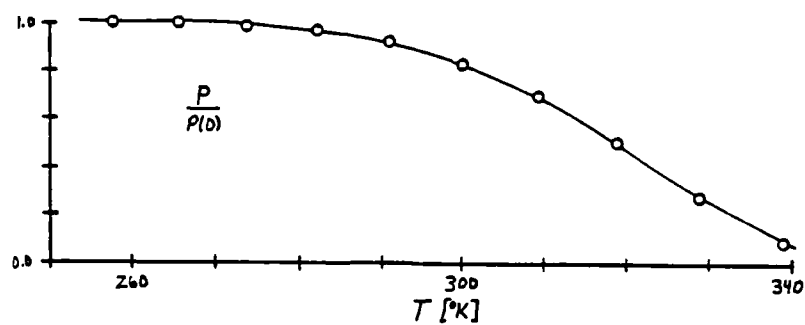
The primary quantities we wish to calculate in these runs are the temperature  $T_{ann}$  at which the annealing rate is greatest and the average activation energy calculated using the change-of-slope method. Figure 6-6 shows the results of an annealing run with  $c_1(0) = 10^{-5}$  and  $c_s = 10^{-6}$ . In these plots we show 1) the "resistivity"  $P$  versus temperature; 2) the temperature derivative of  $P$ ,  $T \cdot dP/dT$ ; and 3) the activation energy calculated at the temperature changes. Note that as the temperature is increased, a point is reached at which the annealing rate is maximum. The temperature at this point is  $T_{ann}$  for

this particular run. Since the effective activation energy may vary with temperature during the run, the average activation energy is calculate from the energy values between about 95% and 5% of the initial resistivity  $R_0$ .

The overall results of the rate equations solutions are shown in Table 6-6 and 6-7. Table 6-6 indicates that the activation energies do not follow an easily predictable pattern. In general, the effective activation energy is fairly close to the single vacancy migration energy of 0.82 eV. This indicates that single vacancy migration controls the annealing rate in most runs. The primary exception is the case in which  $c_1(0) = 10^{-5}$  and  $c_3 = 10^{-6}$ . This run is shown in Figure 6-6. In the beginning of the run the activation energy is relatively low and then increases to an energy similar to the average values in other runs. This indicates that initially another process in addition to single vacancy migration is also controlling the annealing. At early times the primary pathways for the annealing of vacancies is the combination of single vacancies to form divacancies, which then migrate to sinks. At later times, the single vacancy concentration decreases such that a single vacancy will annihilate at a sink before it can combine with another vacancy. Hence, at early times in this particular run,

**Figure 6-6: Results of an Annealing Run**

$$C_s = 10^{-6}, \quad C_i(0) = 10^{-5}$$



divacancy migration partially controls the annealing and the divacancy migration energy affects the calculated effective activation energy.

| $-\log(c_1(0))$ | $-\log(c_s)$ |      |      |      |
|-----------------|--------------|------|------|------|
|                 | 4            | 5    | 6    | 8    |
| 4               | 0.80         | 0.78 | 0.79 | 0.79 |
| 5               | 0.81         | 0.78 | 0.68 | 0.74 |
| 6               | 0.81         | 0.80 | 0.79 | 0.81 |

Table 6-6: Average Effective Activation Energies of Anneals (eV)

The behavior of the maximum annealing temperature  $T_{ann}$  with sink and initial vacancy concentration, shown in Table 6-7, is easier to explain than the behavior of the average annealing temperature. We find that at high sink concentrations,  $T_{ann}$  is relatively independent of initial vacancy concentration, but at low sink concentrations the initial vacancy concentration does affect  $T_{ann}$ . At high sink concentrations, the primary annihilation mechanism for vacancies is absorption by sinks. This is a first order reaction since its rate equation term is proportional to the single vacancy concentration, given by  $a_1 c_1 c_s$ . The probability that an individual vacancy will interact per unit time is simply the rate equation term divided by  $c_1$ , i.e.,  $a_1 c_s$ . Hence, the probability that a particular individual vacancy will interact with a sink is independent of vacancy concentration. As we increase the

vacancy concentration, we expect more vacancies to interact with sinks per unit time, but the peak annealing rate should occur at the same temperature. At low sink concentrations, instead migrating directly to sinks, single vacancies form divacancies first and which either migrate to a sink or perhaps form larger clusters. The rate-limiting step is the vacancy-vacancy interaction which is a second order reaction given by  $a c_v^2$ . (Strictly speaking, the overall reaction will not be quite second order, since the dissociation of divacancies, a first order reaction, will also play a role). The probability that an individual vacancy will interact with another vacancy is proportional to  $a c_v$ . Hence, the higher the concentration, the faster the reaction will occur and  $T_{ann}$  will occur at a lower temperature.

| $-\log(c_v(0))$ | $-\log(c_s)$ |     |     |     |
|-----------------|--------------|-----|-----|-----|
|                 | 4            | 5   | 6   | 8   |
| 4               | 282          | 285 | 287 | 287 |
| 5               | 291          | 306 | 325 | 325 |
| 6               | 291          | 312 | 335 | 383 |

Table 6-7: Temperatures for Maximum Annealing [K]

#### 6.4 Discussion

Compared to calculations of the binding energies of vacancy clusters, there have been very few calculations of their migration energies for other than divacancies. The

primary reason for this is that, although single and divacancy migrations in fcc metals occur through simple and predictable mechanisms, the large number of possible configurations of large clusters makes enumeration of their migration paths difficult. As was shown in Section 2, it is necessary to first determine the stable cluster configuration(s), and then calculate migration energies of favorable migration paths. The first work in this area was done by Johnson on vacancy clusters in nickel using the Johnson I potential<sup>22</sup>. After calculating the binding energies various vacancy clusters, Johnson discovered that the energies could be accurately estimated by bond counting (creation of a vacancy breaks twelve nearest neighbor bonds). Bond-counting suggests that the most compact clusters (voids) are the most stable, which is definitely not the case for the copper potential in this work. As is shown in the following Chapter, beyond clusters of ten or more vacancies, stacking fault tetrahedra and hexagonal loops are formed and voids are not observed. Johnson also noted that the calculated migration energies of vacancy clusters could be estimated by the divacancy migration energy added to one-half the difference in the binding energies of the initial and final configurations. Since, to migrate, a large cluster must partially disassociate, i.e., move through a higher-energy configuration, the large cluster migration

energies are always higher than the divacancy migration energy. This is obviously not the case in this work in which the tri- and tetravacancy were at least as mobile as the divacancy. The Johnson I potential probably yields such simple formulas for vacancy properties because it contains only first nearest neighbor contributions. Dagens' potential used in this work is truncated at the twelfth nearest neighbor distance, and the lattice must be held together by applying an external stress. Although simple formulations have been used to estimate the vacancy cluster migration energies<sup>72</sup>, the conclusion here is that vacancy migration energies are very sensitive to the potential and must be calculated using molecular statics.

The most interesting aspect of the tri- and tetravacancy migration results is that the trivacancy is about as mobile as divacancy, and the tetravacancy is more so. Trivacancies are believed to be more mobile than single and divacancies in some metals such as gold<sup>68</sup> and aluminum<sup>4</sup> based on experimental results, but experimental studies have not been able to determine migration energies for divacancies or larger vacancy clusters in copper. There is evidence for a vacancy cluster in copper which is more mobile than the single vacancy, but the number of vacancies in this cluster has not been unambiguously identified<sup>5, 6, 7</sup>. Wienhold et al<sup>5</sup> did annealing studies of electron-irradiated copper using doped and undoped

samples. Doping was used in electron-irradiation annealing experiments to suppress the formation of vacancy clusters. Wienhold et al<sup>5</sup> found that the doped and undoped samples both yielded the same activation energy of about 0.71 ev, which indicated that single vacancies have an activation energy of about 0.71 ev. On the other hand, the annealing of the doped sample was governed by first order kinetics and the undoped sample by second order kinetics. First order kinetics in the former sample indicates that the single vacancies are annihilating at sinks. Second order kinetics indicates that the rate-controlling step in the annealing is the association of a defect with another defect of the same type (e.g., two single vacancies combining to form divacancies). Hence, clusters must be forming, but apparently they do not affect the effective activation energy of the annealing. As Wienhold et al<sup>5</sup> point out, this can happen if the larger clusters (presumably divacancies) have a migration energy of about 0.71 ev, or if they are so mobile that they do not limit the rate of annealing (i.e., they combine with sinks or other vacancies almost instantly on formation because they migrate so quickly). The latter possibility was selected by Wienhold et al<sup>5</sup> as the more likely case.

<sup>4</sup> Balluffi has reviewed the annealing studies for various metals including copper. The main conclusion of



these studies is that the calculated activation energy using quenched materials is relatively constant and there is no indication of the effect of divacancies on the activation energy.

The results of the annealing runs summarized in Tables 6-6 and 6-7, however, do indicate that the larger clusters do affect the effective annealing activation energy. In one particular case, it was found that an activation energy of almost 0.2 eV less than the single vacancy migration energy was calculated. Although experimental uncertainties can mask some variation in the activation energy, it is difficult to believe that a range of 0.2 eV (i.e., close 25 percent) would be missed. It should be noted that the very low sink concentration runs are probably closest to quenching studies the activation energy was fairly constant. The high sink concentration runs correspond to electron-irradiation of doped samples, and in these cases the activation energy is also constant. The mid-range sink concentration runs, with  $c_s = 10^{-5}$  and  $10^{-6}$ , probably correspond to electron-irradiation of undoped copper, and it is in these cases where calculated and experimental results differ.

The results in Table 6-7 follow the behavior in doped and undoped copper reported by Wienhold<sup>5</sup>. At high sink concentrations, it is found that the primary reaction is

first order, but at low concentrations a slower reaction is also involved. This is not surprising since divacancies are included in the reaction scheme in Table 6-4, but it does show that neither larger vacancies nor the low binding energy of the divacancies suppress this behavior.

Other experimental evidence for highly mobile vacancy clusters in copper come from perturbed-angular-correlation (PAC) studies<sup>6, 7</sup>. PAC is a useful method because only defects which are mobile are identified<sup>73</sup>. PAC studies on copper indicate that two vacancy-like defects are mobile in stage III<sup>6, 7</sup>. Although other mobile defect clusters were not found, it is possible that the highly mobile tri- and tetravacancies calculated in this work would be invisible to PAC. The highest tri- and tetravacancy concentrations observed in the annealing runs in this work were  $10^{-9}$  and  $10^{-11}$ , respectively, which may be too low to be detected<sup>73</sup>. As Wichert points out, defects are also invisible to PAC if the defects do not bind to the probe atoms, or if the defect-probe configuration has cubic symmetry<sup>73</sup>. On the other hand, based on this work, we cannot say whether or not the mobile vacancy cluster identified by PAC is in fact the divacancy.

The general conclusion of the small defect cluster calculations is that tri- and tetravacancies are more mobile than single vacancies and at least as mobile as

divacancies in copper. Although these results are interesting in themselves, it is difficult to make comparisons with experiment because the data on tri- and tetravacancies in copper is nonexistent. Kinetic modeling of defect annealing in copper indicates that small vacancy clusters should affect the calculated effective activation energy at some defect and sink concentrations, but in most cases the effective activation energy is constant which is supported by experiment<sup>4</sup>. Since it is possible to question the ability of the rate equations to model annealing for a number of reasons<sup>5, 70, 74</sup>, a final conclusion cannot be made in this respect.

Chapter 7  
Large Clusters

7.1 Introduction

The small vacancy defects investigated in Chapter 6 are mobile at temperatures as low as 280K in copper. If vacancies are created at temperatures higher than about 280K, or if the temperature of the specimen is subsequently raised above this temperature, the vacancies will migrate until they combine with other defects or are absorbed by sinks. Experiments in quenched<sup>75</sup> and electron-irradiated<sup>5</sup> copper in Stage III, during which vacancies are mobile, indicate that much of the initial damage at the beginning of the Stage is not annealed, which suggests that large vacancy clusters are formed. These clusters grow, not by migrating, but by capturing single vacancies and small mobile vacancy clusters. The clusters, if sufficiently large, can be observed by transmission electron-microscopy<sup>8</sup>, and it is found that large vacancy clusters are in the form of hexagonal dislocation loops and stacking fault tetrahedra (SFT).

The purpose of this Chapter is to present and discuss the results of molecular statics calculations of the

properties of these large vacancy clusters in copper. Previous copper calculations<sup>76, 77</sup> using empirical potentials have determined the critical size at which the vacancy platelets collapse into loops or SFT. However, no calculations have been performed to determine which of the shapes are the most energetically stable. Since the stacking fault energy is an important factor in determining the stable large cluster configuration, it is calculated first using Dagen's copper potential. The displacement fields and binding energies of various shapes of large clusters are then evaluated. In the final section, these results are compared with previous calculations and experimental observations.

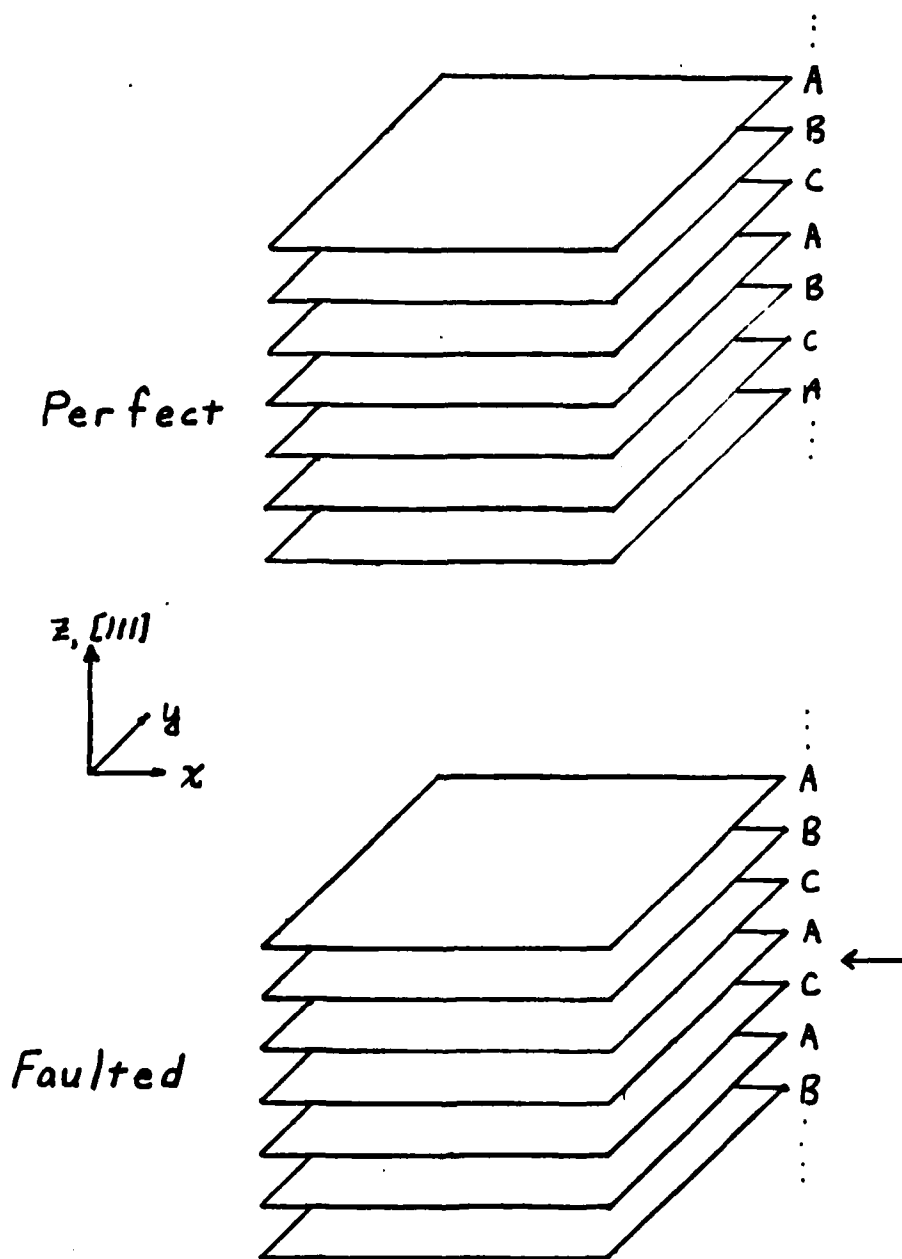
## 7.2 Stacking Fault Energy

It has traditionally been difficult to calculate accurate stacking energies using interatomic potentials and computer simulation. Probably the most important reason for this is that the stacking fault energy depends on the long range part of the potential, i.e, third nearest-neighbor distances and greater, which is not accounted for very well by empirical potentials. (Empirical potentials can, however, be fitted to the stacking fault energy<sup>76, 32</sup>). For example, Johnson's iron and nickel potentials only include second nearest-neighbor interactions, and so have a stacking fault energy of zero<sup>78</sup>.

The stacking fault calculations were performed by setting up an fcc lattice which was rotated so that the [111] direction was pointing in the z-direction, as shown in Figure 7-1. This was done because a stacking fault is a planar defect, and one can simulate an "infinite" fault by taking advantage of periodic boundaries. The lattice then consists of (111) or close-packed planes, which can be stacked in any order. To apply periodic boundary conditions to this rotated lattice, the number of planes required to simulate a perfect lattice must be  $3n$ , where  $n$  is an integer, or  $3n-1$  to simulate a lattice with a single stacking fault. For most of the calculations 14 (111) planes were used, and the boundaries in the x and y directions were made larger than twice the cutoff distance for the potential.

The results of the stacking fault calculations are shown in Table 7-1. Also included in this Table are results from calculations by Cotterill and Doyama using Born-Mayer and Morse potentials for copper<sup>12</sup>. The Born-Mayer potential yields almost negligible stacking fault energies. The Morse potential yields good results when shorter cutoff radii are used, which is probably fortuitous since the Morse potential is not designed to account for long range interactions. The results for Dagens' potential are similar and match the experimental results at short cutoff radii of less than 12 Å. At

**Figure 7-1: Schematic of System for  
Calculating the Stacking  
Fault Energy**



longer cutoff radii, the stacking fault energy becomes negative which means that the HCP lattice is more stable than the FCC lattice. Since Dagens<sup>15</sup> has shown that the FCC lattice is the more stable than the HCP lattice for the copper potential, the reason for this discrepancy is most likely that the fit presented by Lam et al<sup>1</sup> for the interatomic potential is inaccurate at the long range.

| <u>Potential</u>         | <u>Cutoff</u> | <u>Energy [mJ/m<sup>2</sup>]</u> |
|--------------------------|---------------|----------------------------------|
| This work                | 8.5155 A      | 65.3                             |
|                          | 12.0878 A     | 23.3                             |
|                          | 14.4194 A     | -22.0                            |
|                          | >14.4194 A    | negative                         |
| Born-Mayer <sup>12</sup> | 176 atoms     | 0.007                            |
|                          | 4000 atoms    | 0.007                            |
| Morse <sup>12</sup>      | 176 atoms     | 30.8                             |
|                          | 200 atoms     | 17.9                             |
|                          | 4000 atoms    | 0.422                            |
| Exp. <sup>76</sup>       |               | ~70                              |

Table 7-1: Comparison of Stacking Fault Energy Calculations

### 7.3 Large Cluster Configurations and Energies

For consistency, calculations of large vacancy cluster configurations and energies were performed using the same potential radius 8.5155 A and Duesbury factor 0.25a<sup>-1</sup> as for small clusters. A vacancy "platelet" was created in the perfect lattice by removing the desired

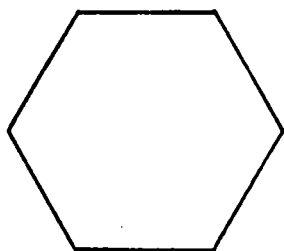


number of adjacent atoms from a (111) plane. The system was then relaxed to the minimum energy configuration, which took from 20 to 100 iterations.

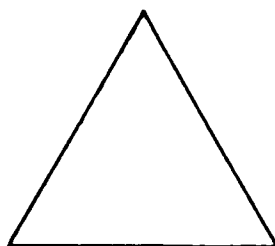
Various numbers of vacancies were removed from a (111) plane in the shapes shown in Figure 7-2. The number of vacancies in the hexagonal loop in a (111) plane are given by  $3n(n+1) + 1$ , where  $n$  is an integer. For  $n = 0$  one gets the trivial case of a single vacancy;  $n = 1$  gives a platelet with seven vacancies. Since Lam et al<sup>3</sup> has found that the lowest energy configuration of a nine vacancy cluster is not a loop, larger sizes were investigated. The two smallest hexagons formed by ten or more vacancies have 19 and 37 vacancies. The triangular shapes are given by  $n(n+1)/2$ ; sizes of 10, 15, 21, 28 were calculated. The number of vacancies in rhomboids can be specified by  $m \times n$ , where  $m$  and  $n$  are integers. Rhomboids of sizes  $4 \times 4$ ,  $4 \times 5$  and  $5 \times 5$  were simulated. The energies of three irregular shapes were calculated: a 19 vacancy hexagon with a side removed to give a 16 vacancy cluster; a 21 vacancy triangle with two corners removed to form a 19 vacancy cluster; and a 14 vacancy cluster formed by removing the acute corners of a 16 vacancy rhomboid.

The first goal of the calculations was to vacancy platelet with the fewest vacancies which would collapse. The criterion for collapse is that atoms above and below the loop move to almost first nearest-neighbor distance

Figure 7-2: Shapes of Vacancy Platelets Introduced into (111) Plane



Hexagon



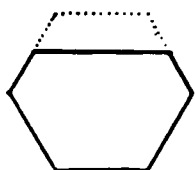
Triangle



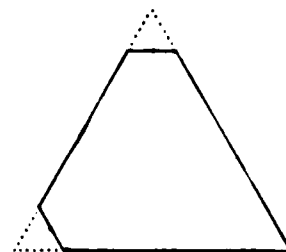
Rhomboid



Rhomboid w/o  
Acute Corners



Hexagon w/o  
Edge



Triangle w/o Two  
Corners

from each other, while remaining almost planar. Contrary to the results of Lam et al<sup>3</sup>, all the shapes that were tested collapsed, including the 19 vacancy hexagon. The displacement field above the 19 vacancy loop is shown in Figure 7-2, which shows that atoms just above the center of the loop are displaced by about half the distance between (111) planes. The planes below the loop are not shown but reflect the behavior above the loop, such that the opposing atoms are at first-neighbor distances from one another. The loop is a Frank loop since there is no evidence of shear. The 37-vacancy loop qualitatively collapsed in the same way.

The displacement field above the center of the 19 and 37 vacancy loops is plotted quantitatively in Figures 7-4 and 7-5. The plot is taken from Ohr<sup>30</sup> and shows the predictions of anisotropic elasticity theory for the displacement fields. The periodic boundaries used in the simulation force the displacement to zero midway between images of the loops, although this zero can in principle be extended to large radii using large simulation volumes. In the 19 vacancy loop, the displacement field appears have converged with increasing system size at short distances above the loop. At  $z/R = 2.5$ , the displacement field calculated in this work differs by at least 40 percent from anisotropic theory predictions. The 37 vacancy results are inconclusive here because the field has not converged with a system size of  $N_0 = 4000$ .

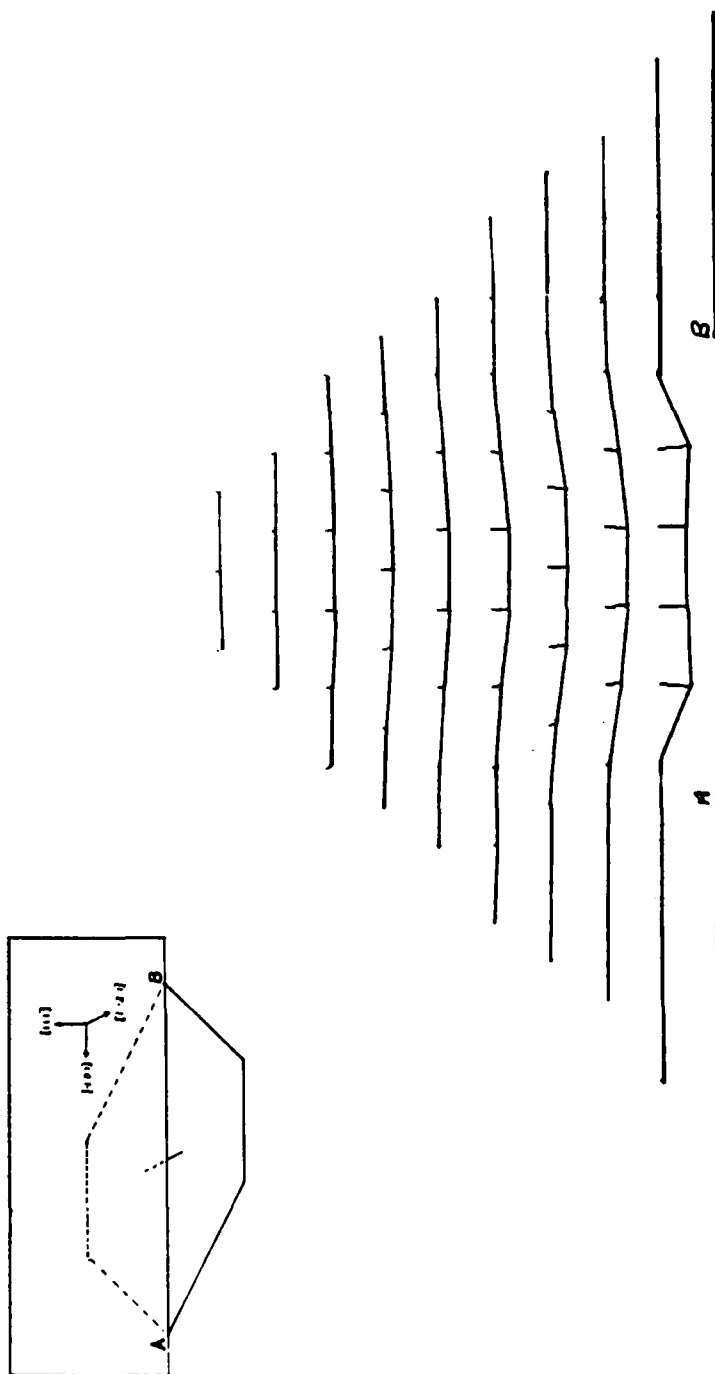
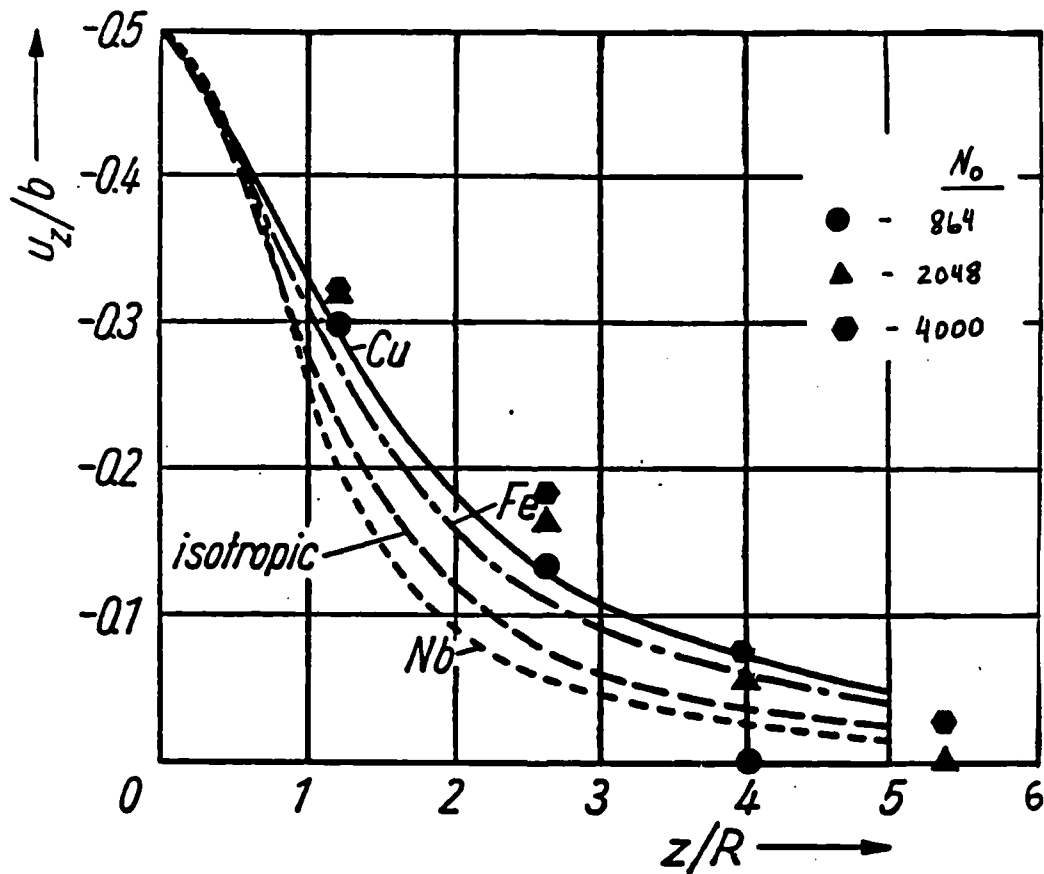


Figure 7-3: Displacement Field above the  
19 Vacancy Hexagon

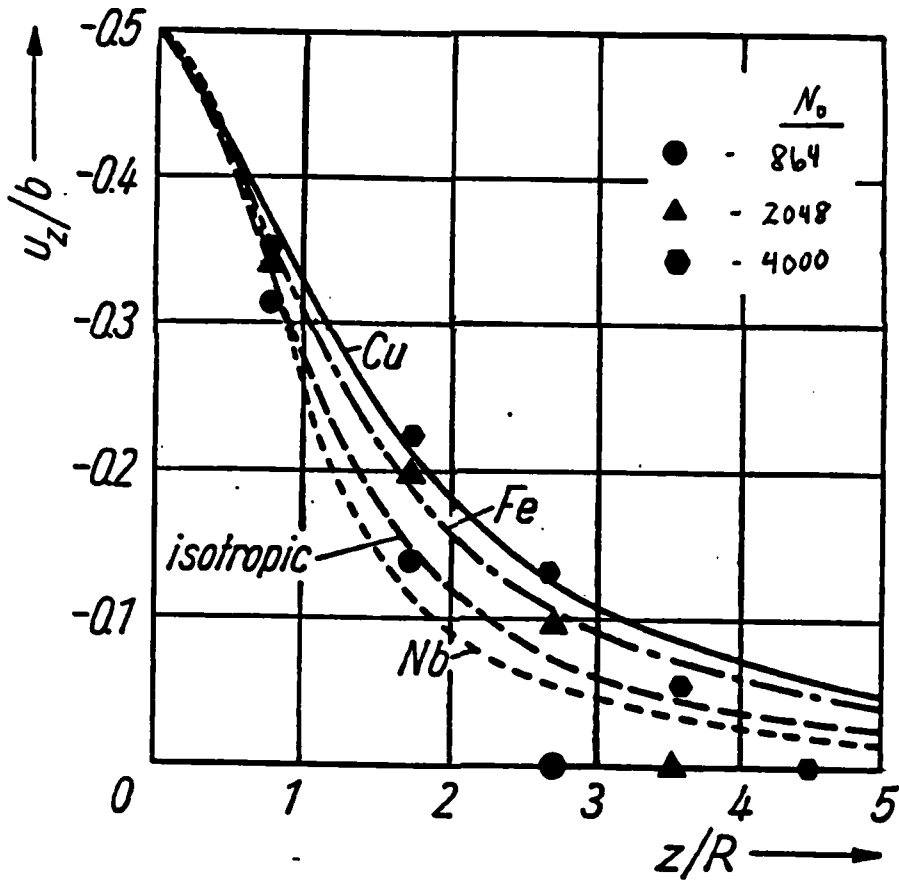
**Figure 7-4:** Displacement in z-direction Above  
19 Vacancy Loop

The lines indicate the predictions of anisotropic elasticity by Ohr<sup>30</sup> for various metals. The symbols are the results of this work for volumes containing the specified number of atoms before vacancies were created. R is the loop radius; b is the Burgers vector  $a[111]/3$ .



**Figure 7-5:** Displacement in z-direction Above  
37 Vacancy Loop

The lines indicate the predictions of anisotropic elasticity by Ohr<sup>30</sup> for various metals. The symbols are the results of this work for volumes containing the specified number of atoms before the vacancies were created. R is the loop radius; b is the Burgers vector  $a[111]/3$ .



The triangular vacancy platelets invariably formed stacking-fault tetrahedra (SFT). Figure 7-5 shows three adjacent (111) planes, including the plane from which the vacancies were removed. The nearest neighbor atoms one plane above the circle atoms after displacement are connected to form triangles. The triangles which contain the circled atoms are inverted in the region of the removed atoms which indicates the stacking fault. The displacement of the atoms after relaxation is shown more clearly in Figure 7-6, which is a cross-section of an SFT created by 21 vacancies. The stacking fault is indicated by the S-labelled triangles; the stair-rod jog by the J-labelled squares. Note that the atoms below the original vacancies have displaced only slightly, whereas the atoms above the vacancies have moved about 4/5 of the distance between (111) planes. In this view the atoms which were displaced the most form a triangle enclosed by the S-triangles and J-squares, and the atoms to the left and right of the triangle are only slightly displaced.

The collapsed rhomboids investigated in this work resulted in asymmetric displacement fields which can be thought of as two adjacent SFT which are inverted in relation to one another. In Figure 7-8 we see a  $(\bar{1}10)$  plane cross-section of a 25 vacancy rhombus. The dashed line indicates the position of the original vacancies; note that the direction of the collapse is opposite on

Figure 7-6: (111) Planes at the Face of an SFT

Three planes at the face of a 28-vacancy SFT are shown. The squares are the atoms in the plane from which the vacancies were removed; the circles and triangles are on the planes below and above, respectively.

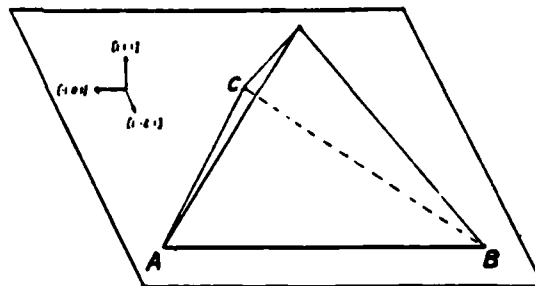
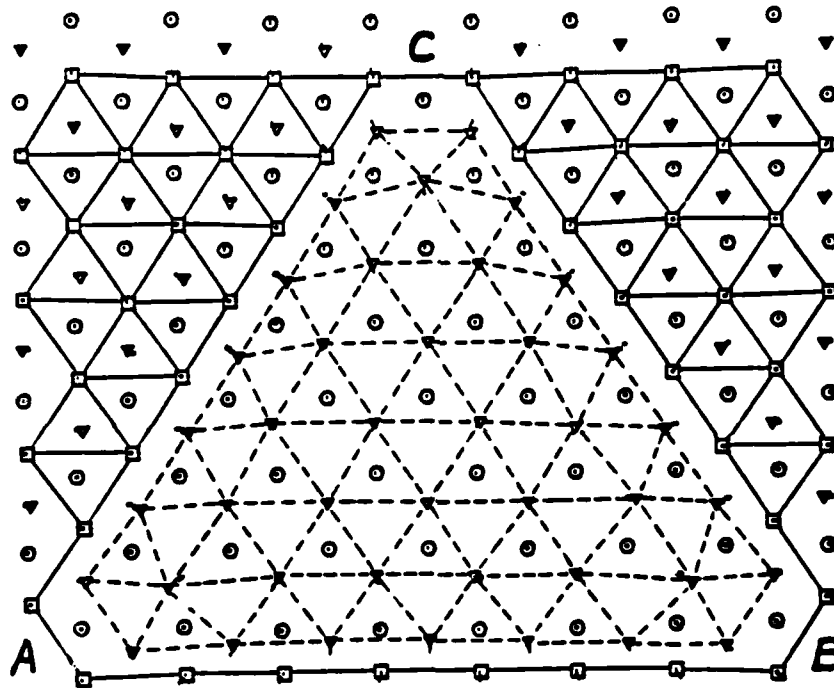
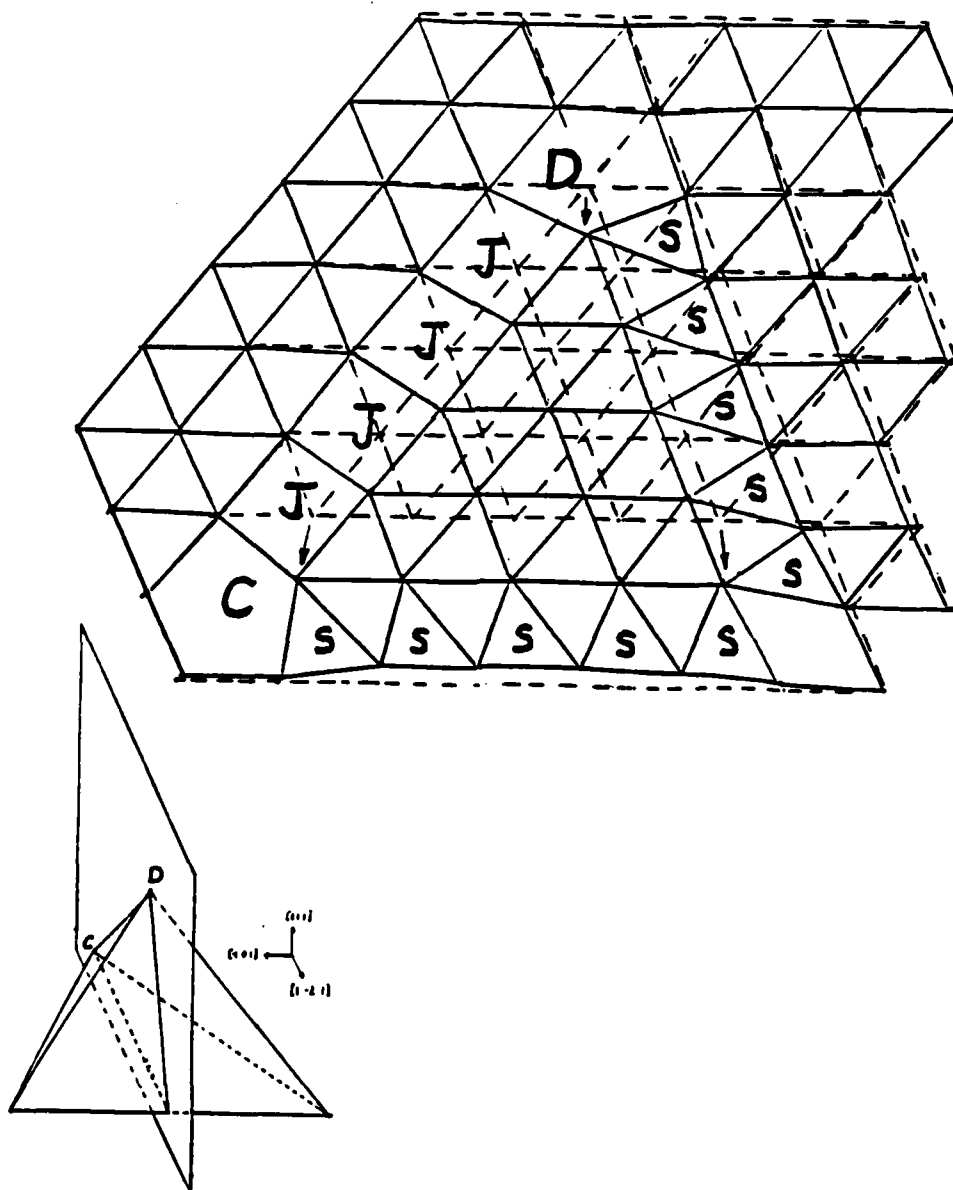




**Figure 7-7: Cross-Section of 21-Vacancy SFT**

The position of the cross-section is shown in the caption. The solid lines connect nearest neighbor atoms after relaxation; the dashed lines show the unrelaxed positions where it significantly differs from the relaxed configuration. The S-triangles and J-squares indicated the stacking fault and stair-rod jog, respectively.



either side. This displacement can be explained by noting that the 25 vacancy rhombus can be constructed from two 15 vacancy triangles (one five vacancy edge of the triangle is counted twice). If these triangles were separated but had the same orientations as in the rhombus, they would form two SFT with opposite orientations. The SFT are then merged into the rhombus, but at the intersecting edge an intermediate displacement field is formed. In Figure 7-9 three adjacent ( $\bar{1}\bar{1}2$ ) planes are shown. Notice this displacement field is qualitatively identical to the field around a similar cross-section in the 19 vacancy hexagonal loop in Figure 7-2. This is not unsurprising when it is noted that the 25 vacancy rhombus can be formed from a 19 vacancy hexagon if three vacancies are added to each of two opposite edges of the hexagon. The atoms in rhombus, however, experience a shear which is not present in the hexagon. In Figure 7-10 three adjacent (111) planes including the plane in which the vacancies were created are shown. The dashed triangles are drawn between the atoms which experience the large displacement on either side of the rhombus as shown in Figure 7-8. The atoms near the acute corners of the rhombus are displaced in a similar manner as the atoms on the face of the SFT shown in Figure 7-5, but there is evidence of shear in the rhombus. In the center of the rhombus where no triangles are drawn, the atoms are displaced to such a great extent

that they line up and the adjacent planes do not form a stacking fault, but are in intermediate positions and are almost unfaulted. Hence, although the rhombus can be considered as the combination of two SFT or as a modified hexagon, we see that the final structure is different than the structure of either a hexagonal loop or an SFT.

The binding energies of the clusters investigated in this work are given in Table 7-2 and plotted in Figure 7-11. Since these large clusters create extensive displacement fields, it was necessary to use large systems to achieve or at least indicate whether or not the calculated binding energies have converged with respect to the size of the system. The polygonal symbols indicate the binding energies in an 864 atom volume; results for larger systems are shown by an 'x' above the polygons. It is evident from Figure 7-11 that the SFT are the most stable over all the cluster sizes and configurations tested. The 19-vacancy "imperfect" SFT, formed from a 21-vacancy triangle with two corners missing, has a binding energy which is about 2 ev greater than the binding energy of the "perfect" 19-vacancy hexagonal loop. The rhomboids are also more stable than the hexagonal loops, but less stable than the SFT.

Figure 7-8: ( $\bar{1}10$ ) Cross-Section of Rhombus

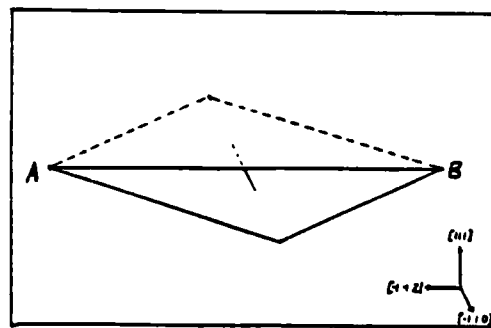
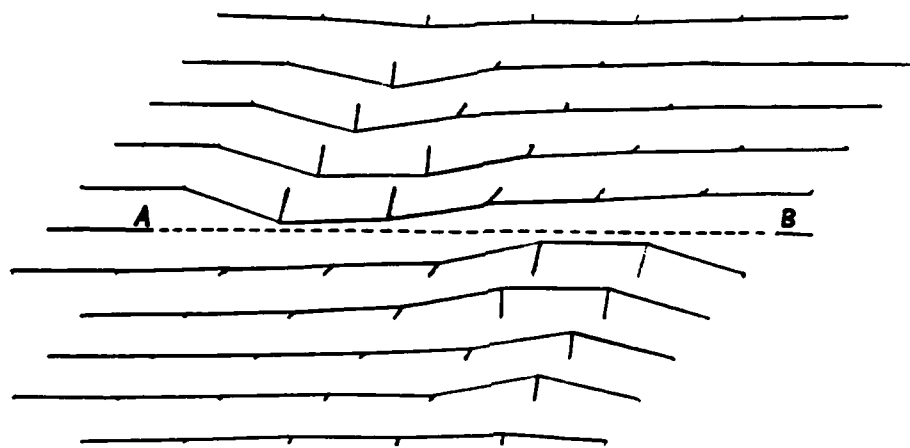


Figure 7-9:  $(\bar{1}\bar{1}2)$  Cross-Section of Rhombus

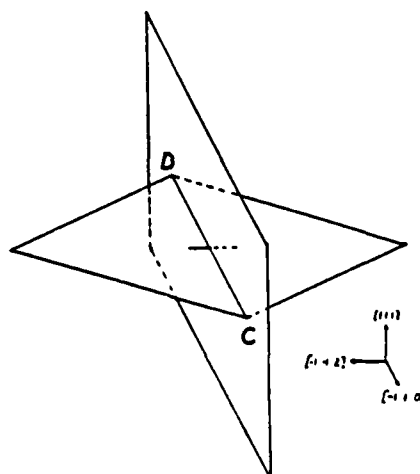
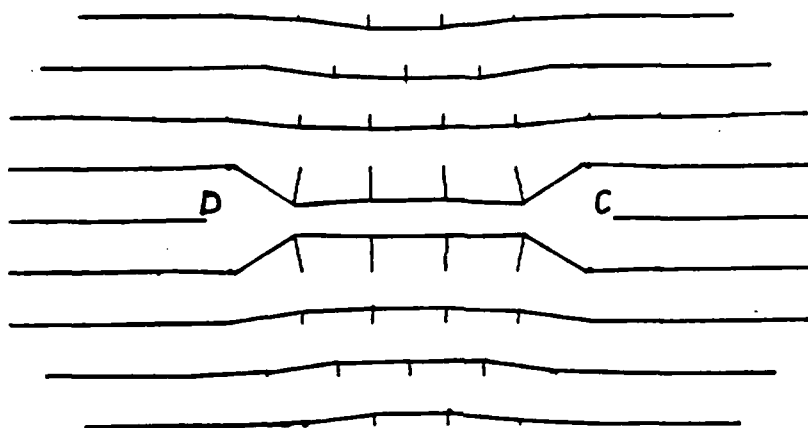
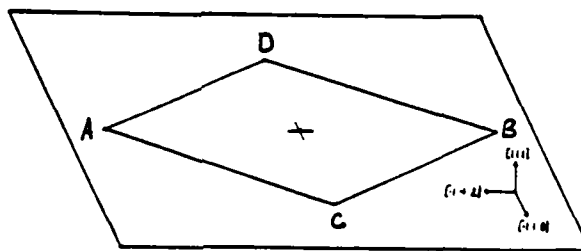
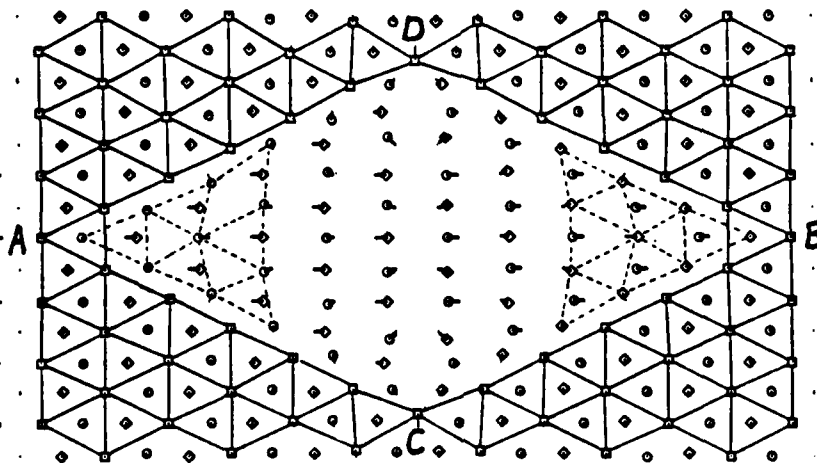


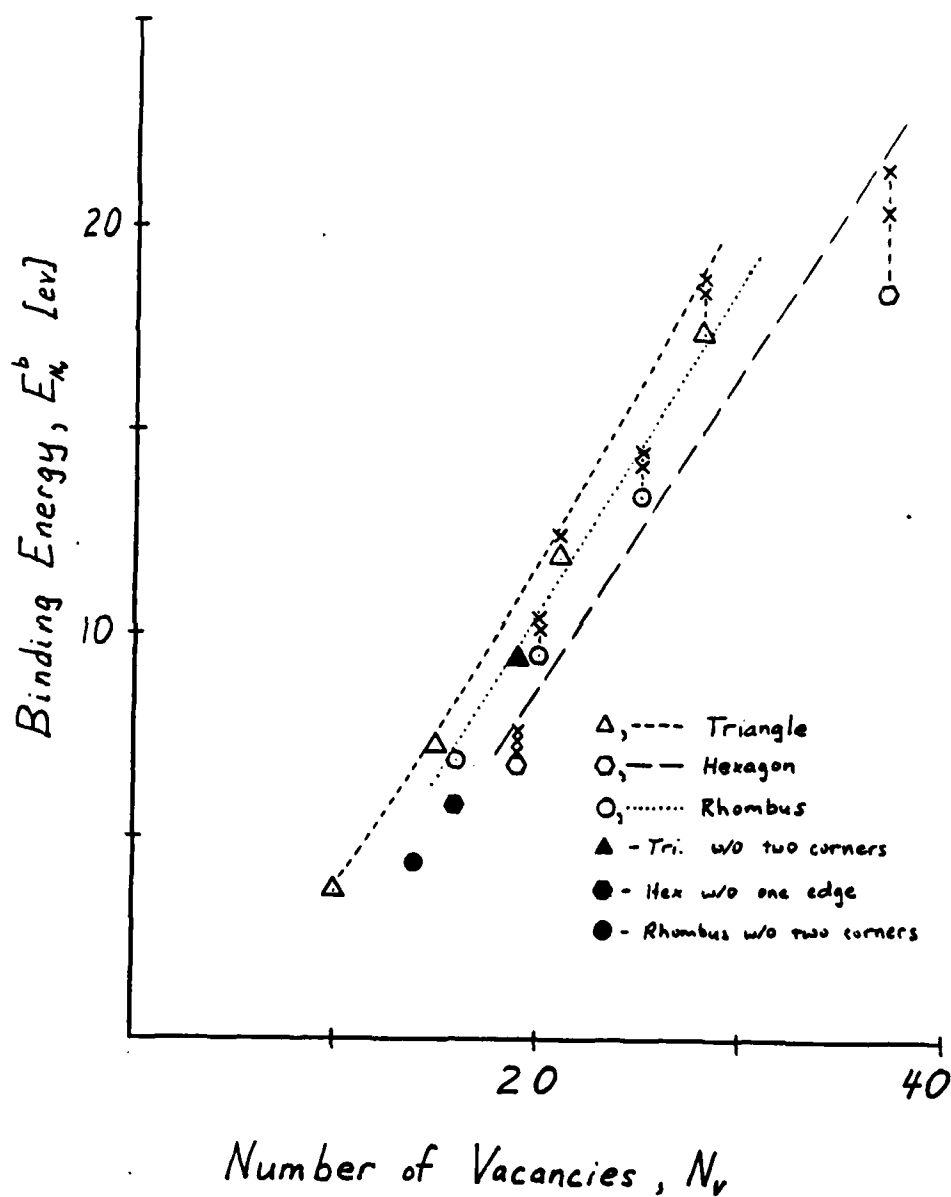
Figure 7-10: (111) Planes above and below Rhombus



| <u>Shape</u> | <u>Cluster Size</u> | <u>System Size</u> | <u>Binding Energy [eV]</u><br><u>Of Cluster</u> <u>Per Vacancy</u> |      |
|--------------|---------------------|--------------------|--|------|
| Hexagon      | 16                  | 864                | 5.79   | 0.36 |
|              | 19                  | 864                | 6.81   | 0.36 |
|              | 19                  | 1372               | 7.17   | 0.38 |
|              | 19                  | 2048               | 7.41   | 0.39 |
|              | 19                  | 4000               | 7.69   | 0.40 |
|              | 37                  | 864                | 18.51  | 0.50 |
|              | 37                  | 2048               | 20.53  | 0.56 |
|              | 37                  | 4000               | 21.44  | 0.58 |
| SFT          | 10                  | 864                | 3.68   | 0.37 |
|              | 15                  | 864                | 7.27   | 0.49 |
|              | 19                  | 864                | 9.34   | 0.49 |
|              | 21                  | 864                | 11.86  | 0.57 |
|              | 21                  | 2048               | 12.43  | 0.59 |
|              | 28                  | 864                | 17.48  | 0.62 |
|              | 28                  | 2048               | 18.39  | 0.66 |
|              | 28                  | 4000               | 18.83  | 0.67 |
| Rhomboid     | 14                  | 864                | 4.41   | 0.35 |
|              | 16                  | 864                | 6.90   | 0.43 |
|              | 20                  | 864                | 9.54   | 0.48 |
|              | 20                  | 2048               | 10.18  | 0.51 |
|              | 20                  | 4000               | 10.48  | 0.52 |
|              | 25                  | 864                | 13.46  | 0.54 |
|              | 25                  | 2048               | 14.23  | 0.57 |
|              | 25                  | 4000               | 14.63  | 0.59 |

Table 7-2: Binding Energies of Large Clusters

Figure 7-11: Binding Energies of Large Clusters





AD-A166 742

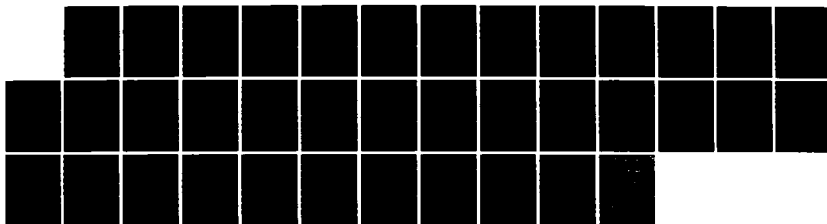
ATOMISTIC SIMULATION STUDY OF VACANCY CLUSTERS IN  
COPPER(U) AIR FORCE INST OF TECH WRIGHT-PATTERSON AFB  
OH M J SABOCHICK 1985 AFIT/CI/NR-86-35D

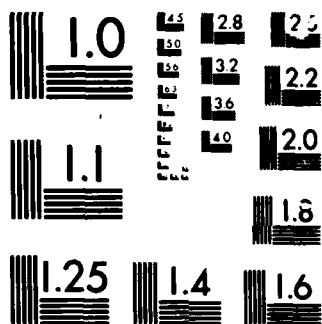
3/3

UNCLASSIFIED

F/G 11/6

ML





MICROCOPY

CHART

#### 7.4 Discussion

The general results of the large cluster calculations in this work follow the results of previous calculations on large clusters in copper<sup>76, 77</sup>. It is found that platelets collapse at relatively small sizes, starting with as few as 10 to 15 vacancies. The triangular vacancy platelets form stacking fault tetrahedra (note that the stable six vacancy cluster for copper found by Lam is a small stacking fault tetrahedron<sup>3</sup>).

It is well known that elasticity theory breaks down near a dislocation and a considerable amount of simulation work has gone into the study of the core region<sup>12</sup>. This is probably the reason for the discrepancy in the results in Figures 7-4 and 7-5. Note in Figure 7-4 that the difference between the simulation results and elasticity theory is fairly large when compared differences in the elasticity theory curves for different metals. Elasticity theory depends only on the elastic constants of a material, and the elastic constants calculated using Dagens' potential correspond very well to the experimental values for copper<sup>15</sup>. Because of this we would expect the correspondence between the the copper results calculated from the simulation and from elasticity theory to be fairly close in Figure 7-5, if the elasticity theory were accurate in this region. This is especially important

since anisotropic elasticity theory is used to interpret<sup>9, 11</sup>  
X-ray diffuse scattering data .

Although the displacement fields around large loops have been previously calculated for copper using atomistic simulation with empirical potentials<sup>76, 77</sup>, this is the first calculation of the binding energies of these clusters.<sup>79</sup> Bacon and Crocker used isotropic elasticity to calculate the energies of symmetrical polygonal loops and found a circular loop to be the most stable, but did not account for the dislocation core. The same results were found when the theory was applied to nonregular polygons<sup>80</sup>. Brown<sup>81</sup> used a two-dimensional analysis of straight dislocation line and applied it to calculating the shape of loops, and concluded that the variation of core energy with orientation would have to be accounted for to find that hexagonal loops were lower in energy than circular loops. The first application of anisotropic elasticity theory to fcc loops was made by Bacon et al<sup>82</sup>, although only rhombus-shaped loops were investigated. Gaboriaud and Grilhe<sup>83</sup> calculated the relative stability of triangular and hexagonal loops and SFT; it was found that SFT were more stable than hexagonal loops of about 4400 vacancies or less (this corresponds to an SFT with an 240 Å edge). These calculations accounted for the disassociation of the partial Frank dislocation around the defect. The results in this work agree with the overall

conclusions of Gaboriaud and Grilhe<sup>83</sup> because it was found that the SFT were the most energetically stable large clusters.

Comparison of this work with experimental evidence is less conclusive. As Kiritani points out<sup>8</sup>, the relative binding energy of clusters is not the only factor which determines whether or not a cluster will be formed. Unless only one type of large cluster was seen under all conditions, it would be difficult to determine the most energetically stable cluster from experimental evidence. In the case of copper, SFT and hexagonal loops have both been observed<sup>8, 84</sup>. The sizes of the collapsed loops also agree with X-ray diffraction studies in which vacancy clusters as small as about 10 Å in diameter are found<sup>9</sup>, although whether the cluster was a loop or SFT could not be determined.

The general conclusion of this work is that loops and SFT can form in copper from small vacancy clusters with as few as ten vacancies. It is interesting to note that the two previous simulations of these large clusters in copper yielded essentially the same conclusions, even though different copper potentials were used<sup>76, 77</sup>. This is one of the few cases where all the potentials for the same metal have given similar results in molecular statics simulations. It is found that there are some

discrepancies between the results of this work and elasticity theory, and it is concluded that the latter is in error for clusters of this size. This is particularly important since the results of Ohr<sup>30</sup> are used to interpret<sup>9, 11</sup> diffuse X-ray scattering observations .

## Chapter 8

### Silver Properties

#### 8.1 Introduction

In addition to the copper potential used in the earlier Chapters of this work, Dagens also developed potentials for the noble metals silver and gold<sup>13, 14, 15</sup>. Similar to the copper potential, excellent correspondence is found between calculated and experimental values of elastic constants<sup>15</sup> and the phonon spectra<sup>17</sup> for silver. Lam et al<sup>1, 3</sup> calculated the formation energies of single vacancies and interstitials, binding energies of some interstitial and vacancy clusters, and the migration energy of single and divacancies in silver. Lam et al<sup>1, 3</sup> calculated the migration energy the single vacancy to be 0.57 eV, which within twelve percent of the experimental result of 0.65 eV<sup>4</sup>. A large discrepancy was found in divacancy migration energies, however, because the calculated and experimental values of the divacancy migration energy are 0.19 eV and 0.57 eV, respectively.

A review of the annealing literature which supports the experimental value of the divacancy migration energy, however, indicates that it is possible to question the

assignment. The divacancy values were originally reported in two separate annealing studies of quenched silver in 1962<sup>85, 86</sup>. The primary finding of both investigations was that an annealing stage exists at ~250K which anneals out about sixty percent of the residual resistivity caused by the defects and which has an effective activation energy of 0.57 ev. At the time it was believed that monovacancies in silver had a migration energy of about 0.82 ev, so the 0.57 ev value was assigned to divacancies. (The single vacancy migration energy was later found to be about 0.65 ev<sup>87, 88</sup>). The second major finding was that the annealing followed second order kinetics throughout sixty to ninety percent of the annealing stage at 250 K. Second order kinetics imply that two of the same type of defect are involved in a reaction. It was suggested that divacancies were combining to form tetravacancies<sup>86</sup> through most of the annealing in the stage. Following the second order kinetics was a faster annealing process, i.e., one that approached first order, which could be explained by the divacancies going to clusters which had already been formed. The general picture which emerged was that the annealing was dominated by divacancies combining with each other during most of the annealing stage, followed by divacancies finally combining with clusters. Tetravacancies are still present to some degree<sup>86</sup> at the end of the annealing stage.



Because of the resistivity remaining at the end of the stage, it is possible that these conclusions may be contradictory. At the end of the annealing stage at 250K, approximately forty percent of the original residual resistivity remains. If most of original defects are now members of tetravacancies, the resistivity per vacancy of a tetravacancy would be about forty percent of that of a single vacancy. It is generally assumed, however, that the resistivity per vacancy is independent of the cluster size at least for small clusters which has been verified in experiments on some metals<sup>71, 89</sup>. Another possible explanation is that at the end of the stage the defects are members of larger clusters which are more likely to have a smaller resistivity per vacancy. At the onset of first order kinetics when divacancies start combining with clusters instead of other divacancies, however, the vacancies must be partitioned between divacancies and tetravacancies since larger clusters are just starting to form. At this point at least thirty percent of the original resistivity has already annealed out; depending on the original vacancy conditions, the tetravacancies once again must have significantly less resistivity contribution per vacancy than single and divacancies do.

Another interesting result reported by Antesburger et al also leads one to suspect that the accepted assignments<sup>87</sup> may not be complete. Antesburger et al performed

annealing studies of pure and doped electron-irradiated silver. The purpose of doping is to create large numbers of vacancy sinks so that the vacancies will interact mainly at the sinks instead of with one another. This process prevents mobile vacancy clusters from forming because the vacancies are annihilated at sinks and interstitial clusters or absorbed by large immobile vacancy clusters before they can encounter another vacancy. Since electron-irradiation experiments usually only produce single vacancies and interstitials, vacancy clusters should not influence the calculated activation energies. It was found that the activation energy for the annealing of the doped silver was constant throughout the annealing stage, as expected. In undoped silver, however, the results were difficult to explain. At high initial defect densities, behavior similar to the doped silver was found, i.e., the activation energy was constant. At low initial defect densities, the activation energy was found to vary from a maximum of 0.65 ev to a minimum of about 0.57 ev. Since divacancies are created by a second-order reaction (the combination of two single vacancies), this is surprising because one would expect divacancy effects to increase with defect density.

The general procedure in annealing studies is to attempt to explain annealing behavior using the simplest possible model. If a single defect (i.e., single vacancy)

cannot explain the results, divacancies and occasionally trivacancies are introduced. This was found to be necessary in gold and aluminum<sup>4</sup>. Often there is support from other types of experiments such as self-diffusion and positron annihilation investigations which provide additional information, but even in these cases interpretations can be incorrect. Gold, for example, is the most extensively investigated metal using annealing studies with investigations dating from the 1950's. The conclusions of an extensive fitting study performed on the available data in 1978<sup>90</sup> were generally accepted<sup>4</sup>, and yet later found to be incorrect<sup>91, 68</sup>.

Because of these questions, we felt it would be interesting to investigate the silver potential of Dagens<sup>15</sup> further. This involves the identification of the migration behavior of the tri- and tetravacancies and primarily the calculation of migration energies. Compared the copper work in Chapters 5, 6, and 7, fewer atoms were used in the silver study for both the small defect and thermodynamic property calculations, and no large defect calculations were performed. Nevertheless, these results provide important groundwork for future work and allow us to make tentative conclusions concerning the silver potential.

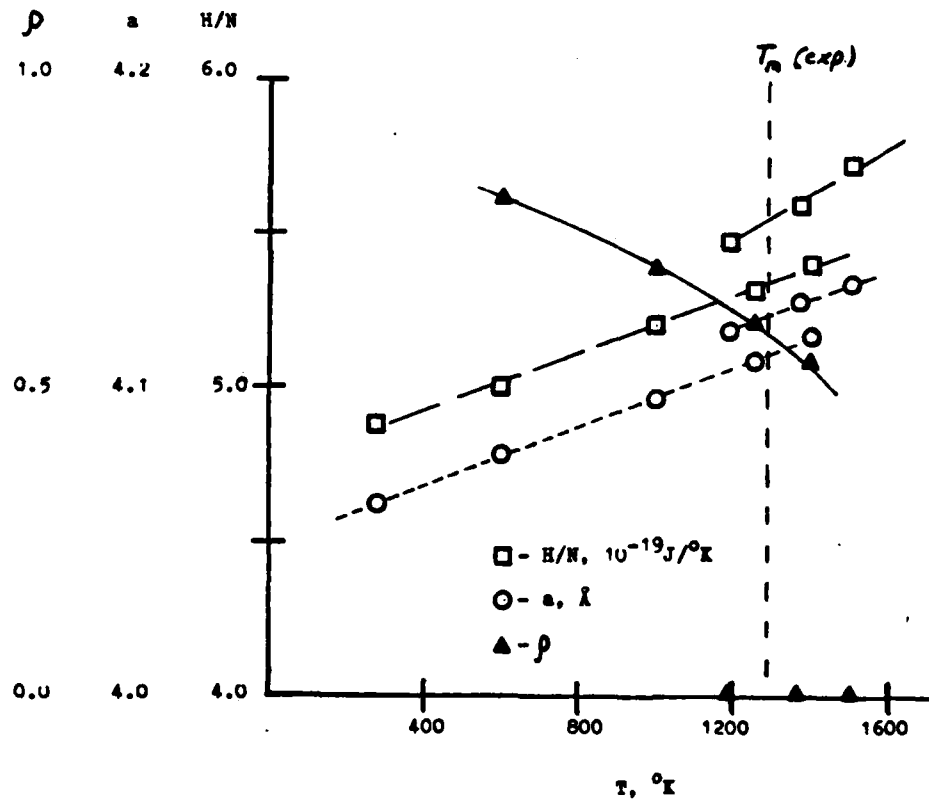
## 8.2 Thermodynamic Properties

As discussed in Section 5.2, it is not possible to calculate the pressure during the simulation since we do not know the structure-independent part of the potential. Instead of calculating silver properties at three different volumes as was done with copper, however, a reference pressure  $P_{ref}$  was calculated and used as a correction to the simulation pressure at all volumes. Since the silver interatomic potential was derived for the lattice constant  $a = 4.087\text{\AA}$ , the reference pressure was calculated at  $T = 298\text{K}$ , since real silver at this temperature and ambient pressure has the desired lattice constant, was found to be  $P_{ref} = 20.8\text{ GPa}$ .

The results of the thermodynamic calculations are plotted in Figure 8-1. These calculations were done with  $N = 108$  atoms and a cutoff radius of  $1.5a$  for the potential. In general the data is well-behaved except near the melting point, which is to be expected. Table 8-1 contains calculated thermodynamic properties and experimental values.

The results of bulk modulus calculations using molecular statics are shown in Figure 8-2, and the calculated bulk modulus is given in Table 8-1. The bulk modulus was calculated at  $T = 0\text{K}$  by setting up the system with a given volume and atoms at the perfect lattice sites

Figure 8-1: Silver Thermodynamic Properties



|  | This Work | <sup>92</sup><br>Exp |
|--|-----------|----------------------|
| $c_p$ [kJ/kg-K]                                | 251.      | 235@298K, 269@820K   |
| $T_m$ [K]                                      | ~1300     | 1235.                |
| $\Delta H_m$ [kJ/Kg]                           | 107.      | 104.2                |
| $\Delta V_f$                                   | 0.014     | 0.05                 |
| $B$ [10 <sup>10</sup> Pa]                      | 10.1      | 10.3                 |
| $\alpha_v$ [10 <sup>-6</sup> K <sup>-1</sup> ] | 10.7      | 19.5                 |

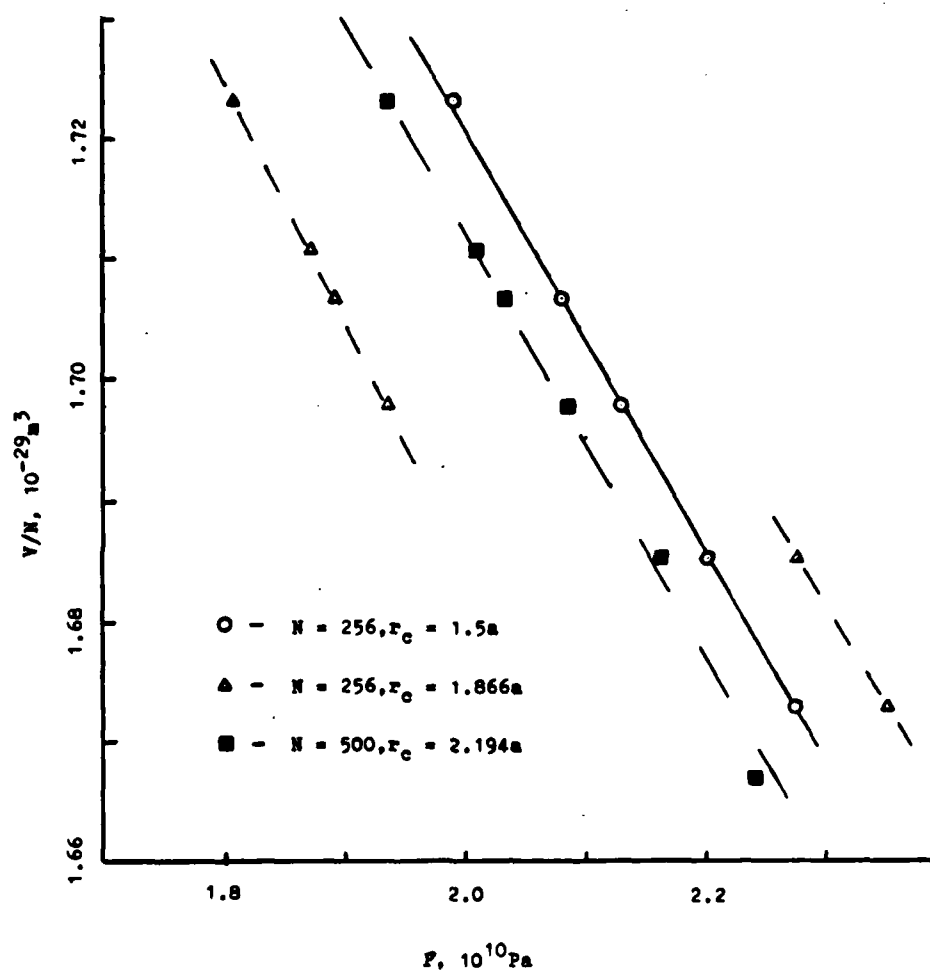
Table 8-1: Comparison of Silver Thermodynamic Properties

and then calculating the pressure. These calculations were done with three different systems which contained a specified number of atoms and potential cutoff radius. The discontinuity shown in the ( $N = 256$ ,  $r_c = 1.866a$ ) case is caused by the atoms crossing the cutoff radius at that particular volume.

### 8.3 Small Cluster Migration

In the small cluster calculations, and cutoff radius of 1.5a was used with a system of 108 atoms. Also, the Duesbury factor<sup>45</sup> was not employed in the silver calculations. Because of this we first wanted to compare<sup>1, 3</sup> the published values of defect results of Lam et al to

Figure 8-2: Silver Bulk Modulus Calculations



ours to insure that there was reasonable agreement. The migration and binding energies of the most stable configurations of some of the vacancy clusters are shown in Table 8-2 for systems of 108 and 256 atoms (before the atoms were removed to create vacancies). Table 8-2 indicates that there is fairly good correspondence between the values. This is not unexpected since the defect properties are mainly determined by the short range portion of the potential. We also confirmed that the configurations listed were the most stable.

| Energy | Lam et al <sup>a</sup> | This Work |        |
|--------|------------------------|-----------|--------|
|        |                        | N'=108    | N'=256 |
| m      |                        |           |        |
| E 1V   | 0.54                   | 0.55      |        |
| b      |                        |           |        |
| E 2V   | 0.04                   | 0.05      |        |
| m      |                        |           |        |
| E 2V   | 0.19                   | 0.22      |        |
| b      |                        |           |        |
| E 3V   | 0.47                   | 0.39      | 0.44   |
| b      |                        |           |        |
| E 4V   | 0.86                   |           | 0.82   |

Table 8-2: Comparison of Silver Results

a - Lam et al<sup>1, 3</sup>

To determine mechanisms of migration and breakup of clusters, it is necessary to know the binding energies of the possible cluster configurations. In Figure 8-3 five

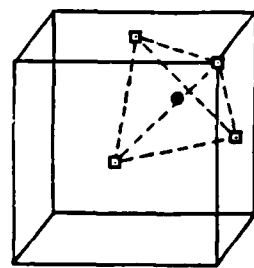


trivacancy configurations are shown. Configuration 3E is not a trivacancy in the sense that all the vacancies are not connected. The binding energies of the configurations are given in Table 8-3. Configuration 3A is definitely the most stable having a binding energy of about 0.25 ev larger than the others. Configuration 3C, which from a migration standpoint is between B and D, is less stable than 3B and 3D. Even though configuration 3E is not a trivacancy by our definition, it's binding energy is fairly close to that of 3C.

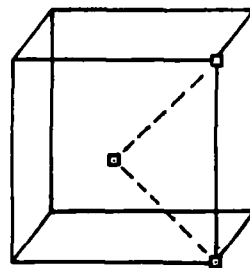
The migration energies between some of the configurations are given in Table 8-4. The trivacancy migrates by transforming from configuration 3A to 3B and then back to 3A at a different site. As shown in Figure 8-4, the transformation is accomplished by the movement of two atoms--the central atom of the 3A configuration and one adjacent atom. The migration energy for the motion is 0.47 ev. Defining a reaction coordinate  $\xi$  such that it is 1.0 near in configuration 3A and -1.0 when near 3B, we can plot the energy barrier as shown in the left half of Figure 8-5.

The breakup of the trivacancy can occur by a transformation from configuration 3B to 3E, as shown in Figure 8-4. The reaction coordinate is defined here to be 1.0 at 3B and -1.0 at 3E. As shown in Figure 8-5, the barrier height between 3B and 3E is about 0.28 ev above

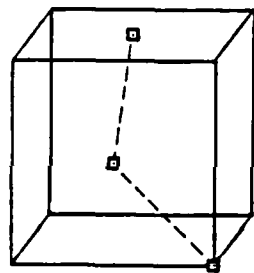
Figure 8-3: Silver Trivacancy Configurations



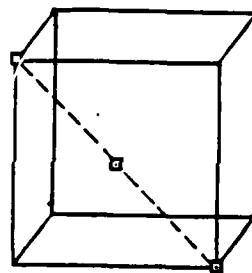
3A



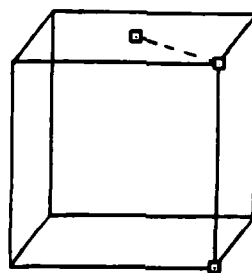
3B



3C



3D



3E

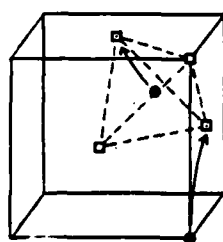
| <u>Cluster</u> | <u>Binding Energy (ev)</u> |
|----------------|----------------------------|
| 3A             | 0.437                      |
| 3B             | 0.201                      |
| 3C             | 0.087                      |
| 3D             | 0.146                      |
| 3E             | 0.047                      |
| 4A             | 0.815                      |
| 4B             | 0.579                      |
| 4C             | 0.514                      |
| 4D             | 0.426                      |

Table 8-3: Binding Energies of  
Silver Vacancy Clusters

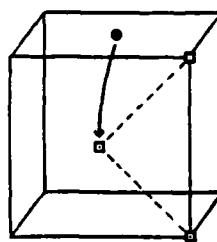
| <u>Transition</u> | <u>Migration Energy (ev)</u> |               |
|-------------------|------------------------------|---------------|
|                   | <u>N'=108</u>                | <u>N'=256</u> |
| 3A->3B            | 0.47                         | 0.47          |
| 3B->3E            | 0.28                         |               |
| 4A->4A'           |                              | 0.38          |
| 4A->4C            |                              | 0.48          |
| 4A->4D            |                              | 0.52          |

Table 8-4: Silver Migration Energies

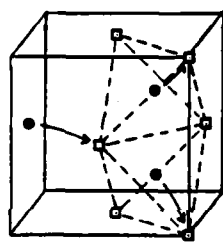
**Figure 8-4: Silver Migration Mechanisms**



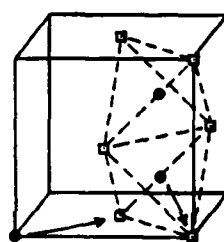
3A → 3B



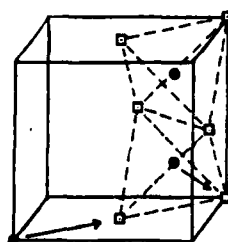
3B → 3E



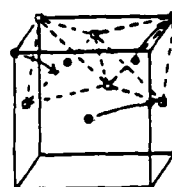
4A → 4B



4A → 4C



4A → 4D



4A → 4A'

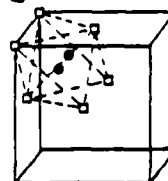
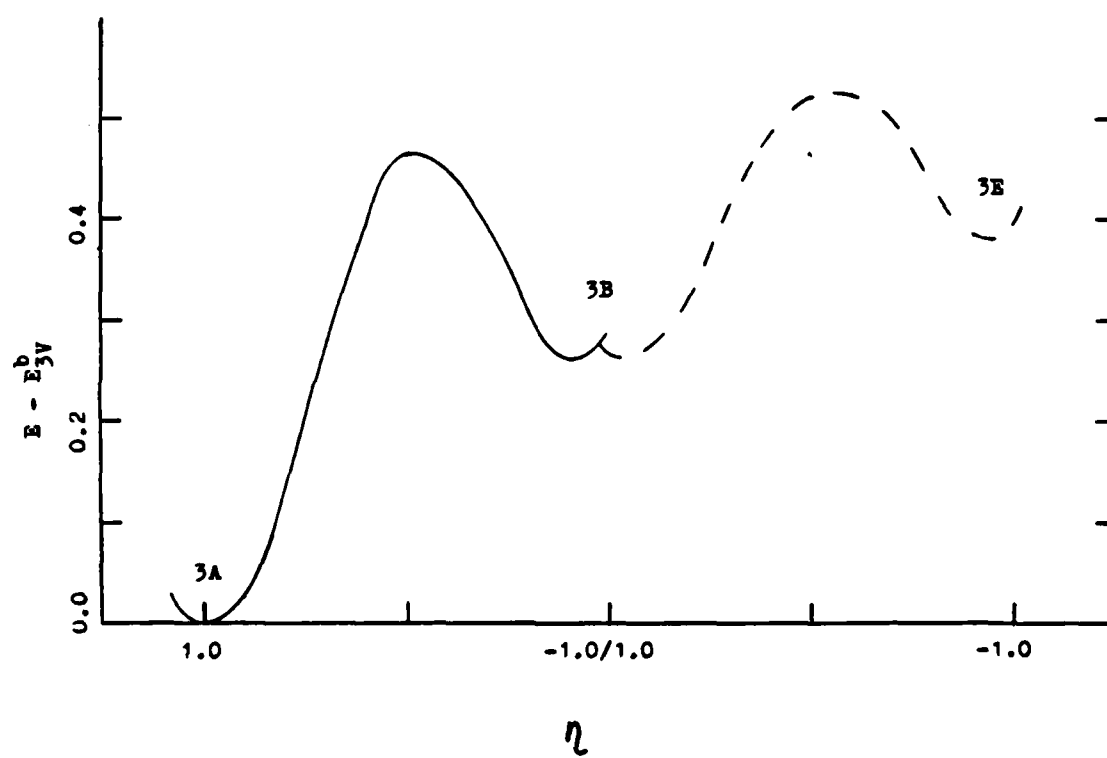


Figure 8-5: Silver Trivacancy Migration Energy Barrier



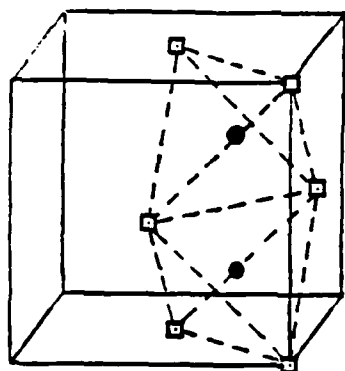
the energy in configuration 3B. We note that the energy at configuration 3E is still somewhat greater than that of an isolated divacancy, so the single and divacancy are still attracted to one another at this point.

The situation for the tetravacancy is more complicated than that for the trivacancy. We investigated the four configurations shown in Figure 8-6. As shown in Table 8-3, configuration 4A is the lowest energy configuration, as reported by Lam et al<sup>3</sup>. The other configurations have much lower binding energies. Note that 4D is not really a tetravacancy since all the vacancies are not connected. Some of the migration mechanisms for the tetravacancy are shown in Figure 8-4, and the migration energies are given in Table 8-4. It is interesting to note that the stable configuration 4A can migrate without passing through a higher energy metastable configuration.

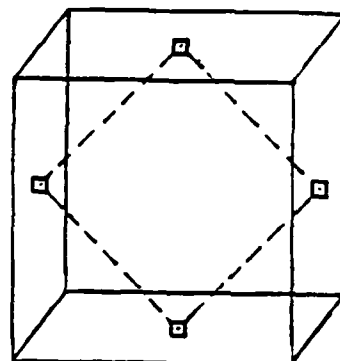
#### 8.4 Discussion

The thermodynamics properties that were calculated in the simulation agree are in good agreement with the experimental results. The two quantities that substantially differ are the thermal linear expansion coefficient  $\alpha$  and the volume change on freezing  $\Delta V_f$ . A possible explanation for the large errors in these quantities is that the reference pressure  $P_{ref}$ , which

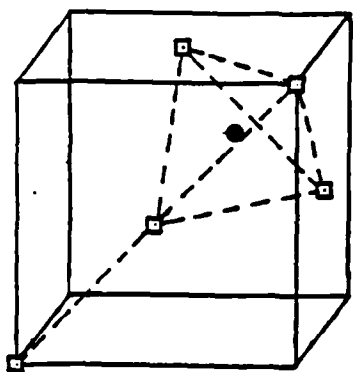
Figure 8-6: Tetravacancy Configurations



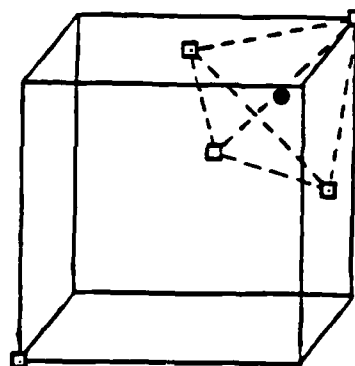
4A



4B



4C



4D

accounted for the cohesive energy of the electrons, is not realistically a constant over the wide temperature range (and phase change) we simulated. Errors in  $P_{ref}$  would significantly affect  $\alpha$  and  $\Delta V_f$  because they depend of volume changes.

The defect calculations in this work indicate interesting defect behavior. The most interesting result is that the tetravacancy is apparently more mobile than the trivacancy. This is caused by the fact that the tetravacancy can migrate without passing through a higher energy metastable configuration, while the trivacancy passes through 3B during migration.

By combining the results of this work with the previous studies by Lam et al<sup>1, 3</sup>, we can begin to understand the annealing behavior of the computer silver we are simulating. In Table 8-5, the basic defect properties affecting annealing are shown. In cases where Lam et al had previously calculated values, we use their  $E_{dis}$  numbers which are more accurate. The column  $E_{dis}$  is the disassociation or breakup energy of the cluster. This value is the difference in binding energies before and after the breakup, added to the migration energy of the most mobile constituent.

We can infer some conclusions from Table 8-5. First of all, the divacancies are so mobile compared to the other clusters that they will be annihilated at sinks or



| <u>Defect</u>  | <u>b</u><br><u>E</u> (ev) | <u>m</u><br><u>E</u> (ev) | <u>dis</u><br><u>E</u> (ev) |
|----------------|---------------------------|---------------------------|-----------------------------|
| V <sub>1</sub> | -                         | 0.55*                     | -                           |
| V <sub>2</sub> | 0.04*                     | 0.19*                     | 0.59                        |
| V <sub>3</sub> | 0.47*                     | 0.47                      | 0.62                        |
| V <sub>4</sub> | 0.86*                     | 0.38                      | 0.86                        |

Table 8-5: Defect Annealing Values in Silver

(\* from Lam et al<sup>1, 3</sup>)

combine with other vacancies almost instantaneously upon formation. This can shown by estimating the jump rate  $J_2$  of the divacancies. The jump rate is given by

$$J_2 = F \exp\left(-\frac{E_m}{2V} / kT\right)$$

where F is a frequency factor. For  $F = 10^{13} \text{ sec}^{-1}$  and  $T = 200\text{K}$ , we have  $J_2 \sim 10^8 \text{ sec}^{-1}$ . With a jump rate this large the divacancies will encounter sinks or other defects very quickly. Because of this, the divacancy concentration will be very low and their direct effect on the calculated activation energy will be small. Even though the divacancy binding energy is very small, they will never disassociate before being annihilated because

disassociation requires single vacancy migration. The indirect effect of the mobile divacancy is that the trivacancy will breakup or disassociate before interacting with other defects because its disassociation energy is low.

The consequence of low divacancy and trivacancy concentrations is that tetravacancy concentrations will also be small because the divacancies and trivacancies are required in reactions that create tetravacancies. Under these circumstances second-order reactions (divacancy-divacancy, trivacancy-trivacancy, etc.) between clusters will be minimal. At the beginning of annealing, some pentavacancies will eventually form and subsequently most of the annealing will be the absorption of single and divacancies by these clusters. We conclude that this annealing scheme does not explain the experimental results on the annealing of quenched silver any better than the previous model, since the reaction under these circumstances will be first order, i.e., single vacancies interacting with sinks and the newly formed vacancy clusters.

The major difficulty with the annealing model suggested by the computer simulation results is the very high mobility of the divacancies. The problem is not that the divacancy concentration is so low, but that the trivacancies disassociate so easily. If trivacancies were

relatively stable during annealing, they would be able to combine with each other in a second-order reaction resulting in the formation for hexavacancies. The problems we pointed out in the annealing model suggested by the quenching studies<sup>86, 85</sup> were based on tetravacancies having a much smaller resistivity per vacancy than single and divacancies. It is likely that hexavacancies have a smaller resistivity per vacancy than tetravacancies, and hence it would somewhat more acceptable if the second order reaction involved tri- instead of divacancies.

The results of these silver calculations support the general conclusions of the copper work. Notably, the silver potential reproduces the thermodynamic properties of real silver better than the copper potential did for copper, and even does well in estimating the melting point (although the density at the melting point is incorrect). The low temperature results are very good, as was found with the copper potential. As before, we find that the migration behavior of the silver tri- and tetravacancies is not easily predictable. In silver it is found that the divacancy is more mobile than single vacancies and tri- and tetravacancies, but the tetravacancies are more mobile than trivacancies.

Chapter 9  
Conclusions

The purpose of this thesis is to apply atomistic simulation techniques to the study of defect clusters in pure metals. Specifically, the method of molecular statics has been used to investigate vacancy clusters using an interatomic potential derived from first principles for copper. The migration energies of small clusters (four vacancies or less) have been determined by considering all possible paths and associated barriers for moving the lowest energy configuration from one location to another. The stable configurations of large clusters of 10-40 vacancies have been studied by forming a vacancy platelet of a given size in a (111) close packed plane, allowing the entire system to relax to the lowest energy configuration, examining the resulting displacement field, and checking for the collapse of adjacent atomic layers.

In order to examine the applicability of Dagens' potential for calculating other properties of copper, the method of molecular dynamics has been used to study bulk properties over a temperature range up to melting. A parallel calculation was also carried out using an empirical potential fitted to the bulk modulus, the

lattice constant at 0K, and point defect properties. These results provide additional evidence for the usefulness of these potentials.

The major findings of the vacancy migration energy study are the migration energies for tri- and tetravacancies, namely, 0.56 eV and 0.38 eV. These are appreciably lower than the single vacancy migration energy of ~0.74 eV, which is reasonably well established from annealing experiments<sup>4</sup>. The divacancy energy has not been experimentally measured, although the divacancy<sup>5</sup> is believed to be more mobile than the single vacancy. Essentially nothing definitive can be said about the tri- and tetravacancies in copper from experiment. Molecular statics calculations based on Dagens' potential give a value of 0.82 eV for the single vacancy migration energy and 0.55 eV for the divacancy. The present results predict that trivacancies should be just as mobile as divacancies, and the tetravacancies even more mobile. This prediction needs to be verified. An attempt has been made to model the existing annealing experiments for copper by using the binding and migration energies of small vacancy clusters calculated using Dagens' potential. It is found that the effective activation energy is still close to the single vacancy migration energy for a variety of sink and initial single vacancy concentrations.

In this thesis, a study was also made of tri- and

tetravacancy migration in silver, for which a first principles potential is also available. It is found that the tri- and tetravacancy are also more mobile than the single vacancy, but in this case they are both less mobile than the divacancy. Combining the copper and silver results, it appears that di-, tri-, and tetravacancy clusters are generally more mobile than the single vacancy, but that the precise relative order can vary from case to case.

The major findings of the study of stability of large vacancy clusters are observations of collapse of platelets with as few as ten vacancies, collapse hexagonal platelets into Frank loops, and the collapse of triangular platelets into stacking fault tetrahedra (SFT). Both Frank loops and SFT have been observed in copper by electron microscopy<sup>8, 84</sup>, and the from X-ray diffuse scattering the smallest Frank loop was found to be about 10 Å in diameter<sup>9</sup>, approximately the size of the 19-vacancy displacement loop. From the simulation results, the displacement field above and below the Frank loop has been calculated and compared with linear anisotropic elasticity calculations<sup>30</sup>; close to the loop, the two results differ which is not surprising in view of the fact that linear elasticity theory is not expected to be valid at short distances. This effect could be important since the elasticity results are used in interpreting X-ray diffuse

scattering data<sup>9, 11</sup>. The binding energies of the Frank loops and SFT have been calculated and the results indicate that SFT are the most stable large vacancy cluster configuration.

The bulk property study shows that both Dagens' and the empirical potentials given reasonable results at low temperatures. This is perhaps to be expected in the case of Dagens' potential since it is already known that the elastic constants and phonon spectra are calculated<sup>14</sup> correctly. As elevated temperatures both potentials are less satisfactory. Although Dagens' potential is better theoretically justified, it is incomplete without the structure-independent term for the purposes of thermodynamic calculations.

This work has shown that it is possible to simulate relatively large vacancy defect clusters using atomistic simulation methods. It would be interesting to repeat these calculations for a different interatomic potential which has a higher stacking fault energy to determine if the large defects are significantly different, perhaps forming unfaulted loops instead of faulted loops and SFT. Furthermore, the dynamical behavior of the large clusters can be investigated using molecular dynamics to observe the formation of stacking fault tetrahedra and unfaulting of Frank loops. The migration energy calculations can be

extended by performing more realistic annealing modeling  
using the correlated random walk method<sup>93</sup>, which may allow  
less ambiguous comparisons to be made with experiment.



REFERENCES

1. N.Q. Lam, L. Dagens and N.V. Doan, J. Phys. F: Metal Physics, 12, 88-110 (1983).
2. W.C. Gear, Numerical Initial Value Problems in Ordinary Differential Equations, Prentice-Hall, Inc., Englewood Cliffs, New Jersey (1971).
3. N.Q. Lam, N.V. Doan and L. Dagens, J. Phys. F: Metal Physics, 15, 799-808 (1985).
4. R.W. Balluffi, J. Nucl. Mat., 69-70, 240-263 (1978).
5. P. Wienhold, K. Sonnenberg and A. Antesberger, Rad. Eff., 36, 235-243 (1978).
6. Th. Wichert, M. Deicher, O. Echt and E. Recknagel, Phys. Rev. Lett., 41, 1659-1662 (1978).
7. M. Deicher, G. Grubel, R. Minde, E. Recknagel and Th. Weichert, in Point Defects in Defect Interactions in Metals, J.-I. Takamura, M. Doyama and M. Kiritani, ed., North Holland Publishing Company, New York (1982), 220-223.
8. M. Kiritani, in Point Defects in Defect Interactions in Metals, J.-I. Takamura, M. Doyama and M. Kiritani, ed., North Holland Publishing Company, New York (1982), 59-66.
9. B. C. Larson and F. W. Young, Jr., in Point Defects in Defect Interactions in Metals, J.-I. Takamura, M. Doyama and M. Kiritani, ed., North Holland Publishing Company, New York (1982), 679-686.
10. M. Ruhle, F. Haussermann and M. Rapp, Phys. Stat. Sol., 39, 609-620 (1970).
11. P. Ehrhart, B. Schonfeld, and K. Sonnenberg, in Point Defects in Defect Interactions in Metals, J.-I. Takamura, M. Doyama and M. Kiritani, ed., North Holland Publishing Company, New York (1982), 687-690.
12. R.M.J. Cotterill and M. Doyama, Phys. Rev., 145, 465-478 (1966).

13. L. Dagens, J. Phys. F: Met. Phys., 6, 1801-1817 (1976).
14. L. Dagens, J. Phys. F: Met. Phys., 7, 7, 1167-1191 (1977).
15. L. Dagens, Phys. Stat. Sol. B, 84, 311-324 (1977).
16. W. A. Harrison, Pseudopotentials in the Theory of Metals, W. A. Benjamin, Inc., New York, (1966).
17. Upadhyaya, J.C., L. Dagens, J. Phys. F: Met. Phys., 9, 2177-84 (1979).
18. L. A. Girifalco and J. R. Streetman, J. Phys. Chem. Sol., 4, 182-189 (1958).
19. L. A. Girifalco and V. G. Weizer, J. Phys. Chem. Sol., 12, 260-264 (1960).
20. L. Tewordt, Phys. Rev., 130, 61-68 (1958).
21. R. A. Johnson, J. Phys. Chem. Sol., 26, 75-80 (1965).
22. R. A. Johnson, Phys. Rev., 152, 629, (1966).
23. Bennett, C.J., in Diffusion in Solids, A. S. Nowick, ed., Academic Press, New York, 1975.
24. B. J. Alder and T. W. Wainwright, J. Chem. Phys., 31, 459 (1959).
25. A. Rahman, Phys. Rev., 136, 405 (1964).
26. J.M. Dickey and H. Paskin, Phys. Rev., 188, 1407 (1969).
27. H.C. Andersen, J. Chem. Phys., 72, 2384-2393 (1980).
28. M. Parrinello and A. Rahman, Phys. Rev. Lett., 45, 1196-1199 (1980).
29. H. R. Schober and R. Zeller, J. Nucl. Mat., 69-70, 341-349 (1978).
30. S. M. Ohr, Phys. Stat. Sol. B, 64, 317-323 (1974).

31. J. Th. M. de Hosson, in Interatomic Potentials in the Study of Materials, J. K. Lee, ed., The Metallurgical Society of AIME, Warrendale, Pennsylvania (1981), 3-30.
32. M. I. Baskes and C. F. Melius, Phys. Rev. B, 20, 3197-3204 (1979).
33. J. B. Gibson, A. N. Goland, M. Milgram and G. H. Vineyard, Phys. Rev., 120, 1229-1253 (1960).
34. S. W. De Leeuw, M. Dixon, and R. J. Elliott, Phil. Mag. A, 46, 677-690 (1982).
35. R. W. Shaw and W. A. Harrison, Phys. Rev., 163, 604-611 (1967).
36. R. W. Shaw, Phys. Rev., 174, 769-781 (1968).
37. R. W. Shaw, J. Phys. C, 2, 2335-2349 (1969).
38. W. A. Harrison, Pseudopotentials in the Theory of Metals, W. A. Benjamin, Inc., New York (1966).
39. W. A. Harrison, Pseudopotentials in the Theory of Metals, W. A. Benjamin, Inc., New York (1966), 319.
40. R. N. Barnett, C. N. Cleveland, and Uzi Landman, Phys. Rev. Lett., 54, 1679-1682 (1985).
41. W. A. Harrison, Phys. Rev., 181, 1036-1053 (1969).
42. J. A. Moriarty, Phys. Rev., 1, 1363-1370 (1975).
43. W. A. Harrison, Pseudopotentials in the Theory of Metals, W. A. Benjamin, Inc., New York (1966), 51.
44. L. Dagens, personal communication, 1985.
45. M. S. Duesbury, G. Jacucci, and Roger Taylor, J. Phys. F., 9, 3 (1979).
46. D. Beeman, J. Comp. Phys., 20, 130-139 (1976).
47. J. M. Haile, A Primer on the Computer Simulation of Atomic Fluids by Molecular Dynamics, unpublished (1981).
48. J. R. Dormand and P. J. Prince, Celestial Mechanics, 18, 223-232 (1978).

49. L. Verlet, Phys. Rev., 159 , 98-103 (1967).
50. G. Ciccotti, M. Guillope and V. Pontikis, Phys. Rev. B, 27, 5576 (1983).
51. M. Parrinello and A. Rahman, J. Appl. Phys., 52, 7182-7190 (1981).
52. M.W. Guinan, R.N. Stuart and R.J. Borg, Physical Review B, 15, 699-710 (1977).
53. J.R. Beeler, Jr., Radiation Effects Computer Experiments, North-Holland Publishing Co., New York, 1983.
54. C.V. Parks, Master's thesis, Department of Nuclear Engineering, North Carolina State University (1978).
55. J. E. Dennis, Jr., and R. B. Schnabel, Numerical Methods for Unconstrained Optimization and Nonlinear Equations, Prentice-Hall, Englewood Cliffs, New Jersey (1983).
56. D. Wolf, Act. Met., 32, 735-748 (1984).
57. Alan Jennings, Matrix Computation for Engineers and Scientists, John Wiley and Sons, New York (1977).
58. R. Fletcher and M. J. D. Powell, Computer J., 6, 163-168 (1963).
59. F. S. Acton, Numerical Methods That Work, Harper and Row, New York (1970).
60. D. McLalan and L.L. Chamberlain, Acta Met, 12, 571 (1964).
61. F. F. Abraham, Phys. Rev., 80, 339-374 (1981).
62. O. L. Deutsch, PhD Thesis, Massachusetts Institute of Technology, 1975.
63. R.M. Nicklow, G. Gilat, H.G. Smith, L.J. Raubenheimer, and M.K. Wilkonson, Phys Rev, 164, 922 (1967).
64. M. De Jong and J.S. Koehler, Phys. Rev., 129, 40-49 (1963).

65. R.W. Siegel, in Point Defects in Defect Interactions in Metals, J.-I. Takamura, M. Doyama and M. Kiritani, ed., North Holland Publishing Company, New York (1982), 533-540.
66. A.C. Damask and G. J. Dienes, Point Defects in Metals, Gordon and Breach Science Publishers, Inc., New York (1963).
67. A. Seeger and W. Frank, Rad. Eff., 31, 17-22 (1976).
68. G.S. Collins, C. Allard, R.B. Schuhmann and C. Hohenemser, Phys. Rev. B, 28, 2940-2946 (1983).
69. W. Schilling, P. Ehrhart, and K. Sonnenberg, CONF-751006-P1\*, (1975).
70. R.A. Johnson, Phys. Rev., 174, 684-690 (1968).
71. R.S. Averback, K.L. Merkle and L.J. Thompson, Rad. Eff., 51, 91-102 (1980).
72. A. G. Crocker, in Interatomic Potentials and Crystalline Defects, The Metallurgical Society of AIME, Warrendale, Pennsylvania (1981), 87-109.
73. Th. Weichert, in Point Defects in Defect Interactions in Metals, J.-I. Takamura, M. Doyama and M. Kiritani, ed., North Holland Publishing Company, New York (1982), 19-26.
74. R.A. Johnson, Phys. Rev. B, 1, 3956-3962 (1970).
75. R.R. Bourassa and B. Lengeler, J. Phys. F: Metal Phys., 6, 1405-1413 (1976).
76. E. J. Savino and R. C. Perrin, J. Phys. F: Met. Phys., 4, 1889 (1974).
77. N. V. Doan, in Point Defects in Defect Interactions in Metals, J.-I. Takamura, M. Doyama and M. Kiritani, ed., North Holland Publishing Company, New York (1982), 722-725.
78. R. A. Johnson, Phil. Mag., 16, 553-564 (1967).
79. D. J. Bacon and A. G. Crocker, Phil. Mag., 12, 195 (1965).

80. R. Dewit and A. W. Ruff, Phil. Mag., 15, 1065 (1967).
81. L. M. Brown, Can. J. Phys., 45, 893 (1967).
82. D. J. Bacon, R. Bullough, and J. R. Willis, Phil. Mag., 22, 31 (1970).
83. R. J. Gaboriaud and J. Grilhe, Phys. Stat. Sol. B, 51, 579 (1972).
84. Y. Shimomura, K. Yamakawa, K. Kitagawa, and H. Oda, in Point Defects in Defect Interactions in Metals, J.-I. Takamura, M. Doyama and M. Kiritani, ed., North Holland Publishing Company, New York (1982), 712-717.
85. L.J. Cuddy and E.S. Machlin, Phil. Mag., 7, 745-761 (1962).
86. M. Doyama and J.S. Koehler, Phys. Rev., 127, 21-31 (1962).
87. G. Antesberger, K. Sonnenberg and P. Wiehhold, J. Nucl. Mat., 69-70, 660-663 (1978).
88. J. Hillairet, C. Mairy, C. Minier, P. Hautojarvi, A. Vehanen and J. Yli-Kaupila, in Point Defects in Defect Interactions in Metals, J.-I. Takamura, M. Doyama and M. Kiritani, ed., North Holland Publishing Company, New York (1982), 284-287.
89. K. Sonnenberg, U. Dedek, P. Ehrhart and W. Schilling, Rad. Eff., 77, 269-272 (1983).
90. R.P. Sahu, K.C. Jain and R.W. Siegel, J. Nucl. Mat., 69-70, 264-276 (1978).
91. K. Sonnenberg and U. Dedek, Rad. Eff., 61, 175-178 (1982).
92. American Society for Metals, Metal Handbook, American Society for Metals, Metals Park, OH, 2 (1979).
93. J.R. Beeler, Jr., Nuclear Metallurgy, 18, 581-603 (1973).

END  
FILMED

5-86

DTIC